

**THE EFFECTS OF LARGE-EDDY MANIPULATOR DEVICES  
ON THE TURBULENT SPOT AND  
THE TURBULENT BOUNDARY LAYER**

**Thesis by  
Stephen Taylor**

**In Partial Fulfillment  
of the Requirements for the Degree of  
Doctor of Philosophy**

**California Institute of Technology  
Pasadena, California**

**1986**

**(Submitted 27 December 1985)**

© 1986

Stephen Taylor

All Rights Reserved

*To Chris and Carolyn*

### **ACKNOWLEDGEMENTS**

I wish to thank my mentors, Professor Hans W. Liepmann and Professor Donald E. Coles, for their guidance and support throughout the research program, and my colleagues in the laboratory, Harry F. Robey and Professor Dan M. Nosenchuck, for their help and suggestions. I also wish to thank Professor Anatol Roshko for his support when it was most needed. It has been both a pleasure and a privilege to work with such professionals.

I thank Jack Kingan, Herb Gaebler, George Lundgren, and Harry Hamaguchi for their willingness to offer assistance and answer my many questions. I also thank Jackie Beard and Kathy Ericksen for their skillful assistance during the rush hours.

Finally, I am grateful to all my friends and colleagues in the GALCIT community for their help, encouragement, and sense of humor.

This research was supported by the Office of Naval Research, contract no. N00014-81-K-0551.

## ABSTRACT

Recent experimental studies indicate that net drag reductions can be achieved in a turbulent boundary layer by placing a tandem configuration of large-eddy manipulator blades in the outer region of the boundary layer. However, the mechanisms responsible for the observed wall-shear reductions are not well understood. Furthermore, discrepancies exist among independent experimental studies regarding the magnitude of the attainable net drag reduction.

A fundamental argument is made regarding the source of the observed wall-shear reductions. It is shown that the tandem manipulator is **not** a low-drag device. The implication is that the momentum deficit in the wake of the manipulator is a prominent contributor to the observed wall-shear reductions, not necessarily that the ability of the large eddies to transport momentum is hampered. The behavior of the wall shear downstream of the device, obtained using hot-film wall-shear sensors, is consistent with the entrainment, mixing, and consequent deceleration of low-momentum fluid from the wake of the manipulator.

With the aid of direct measurements of wall shear, an upper bound is placed on the attainable net drag reduction by establishing a lower bound for the device drag. It is concluded that small net reductions ( $\sim 5$  percent) may be attained at large downstream distances ( $\geq 100$  boundary-layer thicknesses). This conclusion is consistent with most net drag assessments made independently by others in which the momentum-balance technique was employed. However, the result is not consistent with reports of large net reductions ( $\sim 20$  percent) over shorter distances ( $\sim 50$  boundary-layer thicknesses).

Efforts are also made to explain the observed effects in terms of turbulent structure. The turbulent spot is employed as a prototype structure for the large-scale, organized motions in the turbulent boundary layer. Dramatic wall-shear reductions occur in the region of the spot occupied by the large vortex structure. Such reductions are also evident when the spot is propagating in transitional and fully turbulent ambient boundary layers. Although the transport properties of the vortex structure may be affected by the manipulator, it is proposed that an important source of the wall-shear reductions is the transport by the large vortex of low-momentum fluid in the wake of the manipulator.

Some effects of a three-dimensional manipulator are also explored. The design of the device is based on a crude model of the three-dimensional structure of the turbulent spot. Although it appears that the device inhibits the spanwise growth of the spot, its overall effect on the wall shear of the spot and the turbulent boundary layer does not represent an improvement over the effectiveness of a comparable tandem configuration.

## TABLE OF CONTENTS

Chapter	Title	Page
	COPYRIGHT	ii
	DEDICATION	iii
	ACKNOWLEDGMENTS	iv
	ABSTRACT	v
	TABLE OF CONTENTS	vii
	LIST OF FIGURES	x
	LIST OF SYMBOLS	xiii
1	INTRODUCTION	1
	1.1 Historical Overview	1
	1.2 Present Objectives and Approach	5
2	EXPERIMENTAL FACILITY, INSTRUMENTATION, AND PROCEDURE	8
	2.1 General Experimental Procedure	8
	2.2 GALCIT High-Speed Water Tunnel (HSWT)	8
	2.3 Flat-Plate Model	9
	2.4 Turbulent Spot Trigger	10
	2.5 Tandem-Manipulator Configuration	15
	2.6 Hot-Film Wall-Shear Sensors	16
	2.7 Cylindrical Hot-Film Velocity Sensors	18
	2.8 Circuitry for Wall-Shear and Velocity Sensors	18
	2.9 Data-Acquisition and Processing Systems	19

3	MANIPULATOR EFFECTS ON WALL SHEAR IN A TURBULENT BOUNDARY LAYER	20
	3.1 Undisturbed Boundary Layer Behavior	20
	3.2 Manipulated Wall-Shear Behavior	22
	3.3 Importance of the Manipulator Wake	23
	3.4 Prospects for Net Drag Reduction	25
4	MANIPULATOR EFFECTS ON TURBULENT SPOTS	28
	4.1 Undisturbed Turbulent Spot Behavior	28
	4.1.1 Turbulent Spot Generation	28
	4.1.2 Ensemble-averaging Technique	29
	4.1.3 Interface Celerities and Virtual Origin	29
	4.1.4 Spanwise Extent	31
	4.1.5 Estimated Thickness	31
	4.1.6 Comparison with Other Near-wall Measurements	32
	4.2 Effects of a Tandem-Blade Manipulator	32
	4.2.1 Spot Behavior Downstream of Manipulator	33
	4.2.2 Near-Manipulator Spot Behavior	35
	4.3 Entrainment of the Manipulator Wake	37
	4.4 Turbulent Spot in an Ambient Turbulent Boundary Layer	38
5	EFFECTS OF THREE-DIMENSIONAL MANIPULATOR ELEMENTS	40
	5.1 Motivation for Use of a Three-Dimensional Device	40
	5.2 Effects of the Device on Turbulent Spots	43
	5.3 Effects on a Turbulent Boundary Layer	45



6	DISCUSSION AND CONCLUSIONS	48
	6.1 Manipulated Turbulent Boundary Layer	48
	6.2 Manipulated Turbulent Spots	52
	6.3 Effects of a Vertical-Fin Manipulator	56
	APPENDIX	59
	Manufacture of Wall-Shear Sensor Arrays	59
	FIGURES	67
	REFERENCES	102

## LIST OF FIGURES

Figure	Title	Page
1.1	Definition and evaluation of net drag reduction	67
2.1	GALCIT High-Speed Water Tunnel (HSWT)	68
2.2	Schematic of flat-plate model	69
2.3	Typical dimensions of tandem manipulator	70
2.4	Wall-shear sensor array, manufactured at GALCIT	71
2.5	Schematic of bridge circuit used to maintain sensors at constant temperature	72
2.6	Functional schematic of laboratory computer system	73
3.1	Turbulent velocity profile, $x = 40$ cm, $Re_\theta = 1200$	74
3.2	Variation of wall-shear reduction with height of manipulator. (a) $(x - x_m)/\delta_m = 8$ , (b) $(x - x_m)/\delta_m = 13$	75
3.3	Variation of wall-shear reduction with height of manipulator. (a) $(x - x_m)/\delta_m = 31$ , (b) $(x - x_m)/\delta_m = 42$	76
3.4	Mean wall-shear distribution downstream of tandem manipulator, $h/\delta_m \approx 0.75$	77
3.5	Mean wall-shear distribution downstream of tandem manipulator, $h/\delta_m \approx 0.50$	78
3.6	Mean wall-shear distribution downstream of tandem manipulator, $h/\delta_m \approx 0.25$	79
3.7	Minimum required wall-shear reductions (spatially-averaged) for net drag reduction, computed for (a) $L/\delta_m = 1.0$ , and (b) $L/\delta_m = 2.0$ . $Re_\theta = 2000$	80
4.1	Streamwise evolution of an individual spot generated from a <i>low</i> -amplitude heated-element pulse	81
4.2	Streamwise evolution of an individual spot generated from a <i>high</i> -amplitude heated-element pulse	82

4.3	Ensemble-averaged wall-shear time history of a turbulent spot	83
4.4	x-t diagram for a typical turbulent spot	84
4.5	Criteria used to determine interface arrival times	85
4.6	Tandem manipulator effects on the wall shear of an ensemble-averaged spot; laminar ambient boundary layer, $h/\delta_m \approx 0.65$ . (a) $(x-x_m)/\delta_m = 2$ , (b) $(x-x_m)/\delta_m = 12$	86
4.7	Effect of manipulator height on mean wall-shear reduction	87
4.8	Tandem manipulator effects on the wall shear of an ensemble-averaged spot; transitional ambient boundary layer. $h/\delta_m \approx 0.49$ . (a) $(x-x_m)/\delta_m = 2$ , (b) $(x-x_m)/\delta_m = 12$	88
4.9	Wall-shear behavior of turbulent spot in the neighborhood of a manipulator blade. $h/\delta_m \approx 0.70$	89
4.10	Structure and entrainment characteristics of an ensemble-averaged spot. [after Cantwell, Coles, and Dimotakis (1978)]	90
4.11	Manipulated spot propagating in a fully turbulent ambient boundary layer	91
5.1	Schematic of vertical-fin manipulator	92
5.2	Turbulent spot wall-shear behavior due to long-chord, vertical-fin device. $z/b = 0$	93
5.3	Turbulent spot wall-shear behavior due to long-chord, vertical-fin device. $z/b = 0.8$	94
5.4	Turbulent spot wall-shear behavior at its spanwise extremity. Long-chord, vertical-fin device. $z/b = 0.9$	95
5.5	Turbulent spot wall-shear behavior at its spanwise extremity. Short-chord, vertical-fin device. $z/b = 0.9$	96
5.6	Effect of manipulator wake on ambient flow directly downstream of a fin	97

5.7	Comparison between hybrid and tandem manipulators in a turbulent boundary layer. Variation of wall-shear reduction with height of manipulator. (a) $(x-x_m)/\delta_m = 10-13$ , (b) $(x-x_m)/\delta_m = 31-32$	98
5.8	Comparison between vertical-fin manipulator and tandem device in a turbulent boundary layer. Distribution of wall-shear downstream of devices. (a) $h/\delta_m \approx 0.75$ , (b) $h/\delta_m \approx 0.50$ , . The data for the vertical-fin device are the same in both plots.	99
A.1	Design of hot-film wall-shear sensors	100
A.2	Typical pattern of wall-shear sensors. (Pattern used for sensor array in Figure 2.4)	101

### LIST OF SYMBOLS

$\text{\AA}$	angstrom, $10^{-10}$ meters
$b$	half-span of spot, or characteristic spanwise dimension
$B$	law of the wall constant, 5.0
$c$	chord of 3-D manipulator fin
$C_f$	skin friction coefficient, $\frac{\tau_w}{\frac{1}{2}\rho U_\infty^2}$
$d$	$y$ -dimension of 3-D manipulator fin
$D$	drag force per unit span
$h$	manipulator height, measured from wall
$H$	shape factor, $\frac{\delta^*}{\theta}$
$k$	thermal conductivity
$L$	characteristic chord length
$N$	number of spots used in ensemble-average
$p$	pressure
$Pr$	Prandtl number, $\frac{\nu}{\kappa}$
$q$	heat flux (energy/time/area)
$Q$	heat transfer rate (energy/time)
$R$	impedance
$Re$	Reynolds number
$s$	element-to-element manipulator spacing
$t$	time
$T$	temperature
$u$	fluid velocity in $x$ -direction
$u_\tau$	friction velocity, $\sqrt{\tau_w/\rho}$

$U$	mean fluid velocity in $x$ -direction
$v$	fluid velocity in $y$ -direction
$v_w$	equivalent wall velocity due to surface heating
$V$	voltage
$w$	fluid velocity in $z$ -direction
$x$	streamwise distance, from leading edge of flat-plate model
$y$	distance normal to surface of flat-plate model
$z$	spanwise distance, measured from centerline
$\alpha$	half-angle for lateral growth of spot
$\alpha_s$	spot-induced angle of attack relative to chord of 3-D fin
$\beta$	Clauser equilibrium parameter, $\frac{\delta^*}{\tau_w} \frac{dp}{dx}$
$\gamma$	thermal coefficient of resistivity
$\Gamma$	circulation
$\delta$	boundary-layer thickness, $U(\delta) = 0.995 U_\infty$
$\delta^*$	displacement thickness, $\int_0^\infty (1 - \frac{u}{U_\infty}) dy$
$\delta_t$	thermal boundary-layer thickness
$\Delta T$	temperature difference, $T_w - T_\infty$
$\eta$	similarity coordinate in $y$ -direction, $\frac{y - y_0}{U_\infty(t - t_0)}$
$\theta$	momentum thickness, $\int_0^\infty \frac{u}{U_\infty} (1 - \frac{u}{U_\infty}) dy$
$\kappa$	thermal diffusivity, or Karman constant, 0.41
$\mu$	dynamic viscosity
$\nu$	kinematic viscosity
$\xi$	similarity coordinate for $x$ -direction, $\frac{x - x_0}{U_\infty(t - t_0)}$
$\rho$	density
$\tau_w$	wall shear (force/area)

$\varphi$	flap angle with respect to stream direction
$\omega$	radian frequency
$\Upsilon$	non-dimensional equivalent wall velocity
$\Phi$	non-dimensional penetration depth

#### Subscripts

$f$	fluid, or fin
$m$	manipulator
$o$	virtual origin, or undisturbed value
$s$	substrate, or spot
$t$	value at edge of thermal boundary layer
$T$	total
$w$	wall value
$\infty$	free-stream value

## Chapter 1

### INTRODUCTION

Flow control, defined here in a broad sense as the purposeful alteration of a given fluid flow, is a subject of great interest to engineers faced with such practical problems as transition fixing, the enhancement of chemical mixing in combustors, the reduction of frictional drag on moving bodies, and the cooling of heated surfaces. The ability to control a given flow depends in part on ingenuity but in larger part on understanding the mechanisms that operate in the undisturbed flow. As the level of understanding of such classical flows as mixing layers, wakes, jets, and boundary layers has increased, so has the number of techniques available for controlling such flows. A recent development of special importance is the introduction of the concept of coherent structure in turbulent flows [e.g., Kline et al. (1967), Brown and Roshko (1971)]. Although the concept itself has not solved turbulence problems, it has opened new avenues for investigations of turbulence and, in particular, turbulence-control techniques.

#### 1.1. Historical Overview

Attempts to purposefully alter the large-eddy behavior in the turbulent boundary layer were first reported by Yajnik and Acharya (1977) and Yajnik et al. (1980), who stretched a screen across the span of the boundary layer. Such experiments were initiated from a different viewpoint than that taken in earlier non-equilibrium turbulent boundary layer experiments [see Tani (1968) for a review of this work]. Yajnik's intent was not simply to increase the momentum thickness, but to modify the turbulent transport properties of the large eddies.



Such work was motivated, in part, by the possibility of achieving a net *viscous* drag reduction, as defined by the inequality

$$\left[ D + \int_{x_1}^{x_2} \tau_w(x) dx \right]_m < \left[ \int_{x_1}^{x_2} \tau_w(x) dx \right]_o$$

where  $D$  represents the device drag, and the subscripts  $m$  and  $o$  refer to the manipulated and undisturbed boundary layers, respectively. Although Yajnik reported wall-shear reductions as large as 55% downstream of the screen, there was no clear indication of either large-eddy breakup or net drag reduction.

In an attempt to develop devices with lower drag that also produced large wall-shear reductions, Hefner et al. (1980) at NASA Langley experimented with honeycombs and various configurations of vertically-stacked plates. In a parallel effort at IIT, Corke et al. (1980) used flow visualization and hot-wire techniques to judge the effectiveness of various multi-element, thin-plate configurations. Such plates were stretched across the span of the flat-plate model and were generally aligned with the flow direction. As with the screens, significant wall-shear reductions were observed downstream of the manipulator, but no net drag reductions were attained despite the reduced drag of the devices.

Net drag reductions were first reported by Corke (1981) and Corke et al. (1982) who employed a tandem configuration of thin plates. Wall-shear reductions as large as 30% coupled with net drag reductions of 20% were reported. Plesniak and Nagib (1985) subsequently reported net drag reductions as large as 30%. Although initial efforts at NASA Langley by Hefner et al. (1983) to reproduce the IIT results proved unsuccessful, subsequent attempts at NASA Langley by Anders et al. (1984) and Anders and Watson (1985), using a larger facility, yielded net drag reductions of approximately 7%. Bertelrud et al. (1982)

reported net drag reductions of approximately 5%. Investigations in which a net drag reduction was not attained include those by Takagi (1983), Mumford and Savill (1984), and Lemay et al. (1985). The drag of the tandem device used by Mumford and Savill was admittedly 50% greater than the laminar flat-plate value, due to the thickness of their blades.

The large discrepancy between the net drag reduction reported by the IIT group ( $\sim 30\%$ ) and that reported by others has remained an issue. Plesniak and Nagib (1985) suggest that the difference is due to the higher device drag encountered by others. They further argue that this conclusion may be inferred from the fact that other investigators report wall-shear reductions comparable to their own. Although the magnitudes of their *peak* wall-shear reductions are comparable to those obtained by others, their average wall-shear reductions at large distances (say,  $50-100 \delta_m$  downstream of the device) are significantly larger than those obtained by direct measurement [e.g., the skin-friction balance measurements of Mumford and Savill (1984), and Lemay et al. (1985)].

One possible cause of the net drag discrepancy may stem from the manner in which the quantity is measured. The magnitude of the net drag can be determined by measuring the device drag and the wall shearing force directly, or by measuring the net momentum flux through an appropriately chosen control volume, as illustrated in Figure 1.1. The net momentum flux is given by the change in momentum thickness between two streamwise stations. This change may be determined from profile measurements of the streamwise velocity component at each of the two stations. The latter approach is experimentally convenient and has been used exclusively in all experiments for which net drag reductions have been reported.

The momentum-balance technique yields a true measure of the net drag acting on the fluid (between the two stations) if: (1) no mean pressure gradient

exists in the flow; (2) the stations 1 and 2 are chosen far enough away from the manipulator to ensure that  $p_1 = p_2$ ; and (3) all momentum fluxes are accounted for, i.e., the flow is strictly two-dimensional. Plesniak and Nagib (1985) report that their flow is noticeably three-dimensional, but maintain that the effects are not important because of the demonstrated self-similarity of the boundary-layer characteristics in the streamwise direction.

Also at issue is the mechanism(s) responsible for the observed effects. Since the tandem manipulator blades are viewed as low-drag devices, investigators have primarily sought mechanisms that hamper the ability of the large eddies to transport high-momentum fluid from the free-stream into regions closer to the wall, where it is rapidly mixed with and decelerated by turbulent fluid. Within the boundary-layer approximation, and in the absence of mean pressure gradients, the deceleration of fluid must eventually be accommodated by with the shearing stresses at the wall. Therefore, if one could reduce the ability of the large eddies to incorporate, or entrain, high-momentum potential fluid into the boundary layer, one would expect to realize reduced wall-shear levels.

Many mechanisms have been proposed [see for example, Corke et al. (1979, 1982), Hefner et al. (1979, 1983), Anders et al. (1984), Mumford and Savill (1984), and Guezennec and Nagib (1985)] including: (1) a direct inhibition of the vertical velocity components of the large eddies due to the presence of the blades; (2) suppression of mixing due to an interaction between vorticity shed in the wake of the manipulator and vorticity that exists in the oncoming flow; (3) a redistribution of turbulent kinetic energy by the wake of the manipulator; and (4) "anti-production" of turbulence due to negative  $\partial \bar{u} / \partial y$  in the wake.

Although many effects have been observed, a basic understanding of the mechanism(s) involved is lacking.

## 1.2. Present Objectives and Approach

The present investigation was motivated by the need to better understand the mechanism responsible for the observed effects of tandem manipulators in a fully turbulent boundary layer.

Detailed descriptions of the facility, flat-plate model, and associated instrumentation are provided in Chapter 2. All of the experiments were performed on a flat-plate model mounted in the GALCIT<sup>†</sup> High-Speed Water Tunnel (HSWT). Turbulent spots were generated by pulsing a small, flush-mounted heating element located near the leading edge of the flat-plate model. This non-intrusive technique was first used by Liepmann et al. (1982) who sinusoidally heated a flush-mounted, full-span metal strip to excite Tollmien-Schlichting waves. The technique, which stemmed from Liepmann's experiments in superfluid helium [see, for example, Laguna (1975)], was originally introduced as a viable alternative to the vibrating ribbon.

Since wall shear is a quantity of particular importance, flush-mounted, hot-film wall-shear sensors were utilized. Arrays of sensors manufactured at GALCIT as well as individual sensors manufactured commercially were used. The general characteristics of both types of sensors are described in Chapter 2, and a detailed description of the manufacturing process for the sensor arrays, developed as part of the present investigation, is given in the Appendix.

Two issues are of particular concern: (1) the identification of the dominant mechanism responsible for the observed wall-shear reductions, and (2) the discrepancies which exist in the literature regarding the magnitude of possible net drag reduction. Both issues are addressed in Chapter 3. A fundamental argument is made regarding the source of the observed wall-shear reductions.

<sup>†</sup> *Guggenheim Aeronautical Laboratory, California Institute of Technology*

It is shown that the tandem manipulator is **not** a low-drag device, which implies that the momentum deficit in the wake of the manipulator is a prominent contributor to the observed wall-shear reductions. The argument is substantiated by the characteristics of mean wall-shear distributions obtained using direct-measurement techniques. Furthermore, an upper bound is placed on the magnitude of achievable net drag reduction, based on direct wall-shear measurements and on a lower-bound estimate for the device drag. It is concluded that small net reductions ( $\sim 5\%$ ) may be possible at large downstream distances ( $\sim 100$  boundary-layer thicknesses).

Efforts to understand the manipulator effects in terms of turbulent structure are described in Chapter 4. The turbulent spot is employed as a prototype structure for the organized large-scale motions in the fully turbulent boundary layer. The wall-shear distribution for manipulated spots in both laminar and fully turbulent ambient boundary layers is investigated, and the results are discussed in terms of the behavior of the ensemble-averaged spot. In particular, the structure of the unmanipulated ensemble-averaged spot deduced by Cantwell et al. (1978) serves as a basis for interpretation of the manipulated spot behavior. It is proposed that the large wall-shear reduction observed near the leading edge of the spot is due to the large-eddy transport of low-momentum fluid from the wake of the manipulator.

Since three-dimensionality is an inherent feature of turbulent flow, it can be conjectured that a three-dimensional device might be better suited to manipulate the large eddies than a two-dimensional device. For example, along off-centerline segments of the large vortex structure in the turbulent spot, one would expect a relatively large fraction of the vorticity in the structure to lie in the streamwise direction due to the highly-swept nature of the vortex tube. As described in Chapter 5, a preliminary investigation was undertaken in which

attempts were made to introduce a streamwise component of vorticity that opposes the natural sense of rotation of the large structure. The device was comprised of a spanwise row of vertical fins, each aligned with the mean flow direction. The function of the fins is to shed tip vortices when subjected to the spanwise component of velocity induced by the highly-swept vortex structure in the spot. Although the design of the device was based on known characteristics of the turbulent spot, the effects of the device were investigated for both the turbulent spot and fully turbulent flow. Wall-shear reductions were observed downstream of the device, but the magnitude of the reductions did not represent an improvement over the effectiveness of a comparable tandem configuration. It is conjectured that the dimension of the fins normal to the wall may have been too large, thus limiting the magnitude of the circulation developed by the fins.

Detailed discussions of the results presented in Chapters 3, 4, and 5, and conclusions drawn from the results, are given in Chapter 6.

## Chapter 2

### EXPERIMENTAL FACILITY, INSTRUMENTATION, AND PROCEDURE

#### 2.1. General Experimental Procedure

Wall-shear changes due to large-eddy manipulators are of primary interest, and it is therefore of importance to ensure that any undesirable changes in the experimental state be avoided. Such changes were alleviated by attaching the manipulator blades to a traversable, bow-shaped support that permitted the height of the blades to be changed quickly, while also holding them in tension.

Arrays of flush-mounted thin-films, maintained at constant temperature, were used to monitor the behavior of the wall shear. Calibration curves were constructed after first traversing the manipulator blades well into the free-stream, typically 3-7 turbulent boundary-layer thicknesses, or spot heights, from the wall. This position also served as the unmanipulated reference height for experiments involving manipulated turbulent boundary layers and manipulated turbulent spots.

Detailed descriptions of the hardware and the manner in which it was utilized are given in the following sections.

#### 2.2. GALCIT High-Speed Water Tunnel

A complete description of the High-Speed Water Tunnel (HSWT) is given in the paper by Ward (1976). As illustrated in Figure 2.1, the HSWT is a closed-circuit facility. A narrow two-dimensional test section (15.3 x 76.2 cm) and a circular test section (35.6 cm diameter) are available for use, but only the latter was employed in the present experiments.

Although the HSWT was designed to achieve free-stream speeds of nearly 30 m/sec, sufficiently high Reynolds numbers can be attained at much lower speeds. For example, at 3 m/sec a Reynolds number of  $3 \times 10^6$  is attained, based on the length of the test section (1.05 m). The range of speeds used in the present experiments was 1-2 m/sec. In addition, the static pressure is adjustable over the range 0.2 bar to 6 bar (absolute), a feature that is important for cavitation studies. Although this range of pressures is not necessary for typical boundary-layer experiments, the ability to adjust the static pressure above and below atmospheric pressure is quite useful for such tasks as air bleed-off, suppression of noise generated from small, trapped air bubbles, and the control of flow rates from dye injectors.

The circular test section is preceded on the upstream end by a 20:1 contraction section that is three meters long, and is followed on the downstream end by a 6:1 diffuser section that is six meters long. A stainless-steel honeycomb and a 40-mesh screen are positioned at the beginning of the contraction section. Conical hot-film velocity measurements by Nosenchuck (1982) indicated that the rms turbulence intensity was less than 0.04% on the centerline and 1.0% at a distance 1.9 cm from the wall of the test section. The mean velocity was found to be uniform at distances greater than 1.9 cm from the wall of the test section.

### **2.3. Flat-Plate Test Model**

A flat-plate model, illustrated in Figure 2.2, was designed and constructed for use in the present experiments, and is compatible with the circular test section of the High-Speed Water Tunnel. The model is comprised of a central plate of constant thickness, a 6:1 elliptical leading edge, and an adjustable trailing-edge flap. The leading edge and the central plate were machined from lucite stock. The trailing-edge flap, constructed from aluminum stock, was installed to permit



the appropriate positioning of the leading-edge stagnation point.

The flat-plate model incorporates a series of four circular cutouts into which instrument-bearing inserts can be mounted. Arrays of wall-shear sensors were mounted on such inserts (see Section 2.6), and could be easily moved from one location to another. The centers of the cutouts are located 19.76, 35.76, 51.77, and 67.77 cm from the leading edge. Typically, only the two downstream-most cut-outs were used.

The flat-plate model was secured to the test section at four points, two near the leading edge and two at the hinge point of the trailing-edge flap. The forward two points of the plate were rigidly attached to the test section, while the two aft-most points were pinned to permit rotation of the flap. After mounting the plate into the test section, the 3-mm gaps between the edges of the model and the test-section wall were filleted with General Electric silicon rubber (RTV) to avoid any communication between the upper and lower surfaces. All electrical leads were confined to the lower, non-active side of the flat-plate model, and exited through water-tight plugs located along the lower-most portion of the test section.

#### **2.4. Turbulent Spot Trigger**

The heated-element technique introduced by Liepmann et al. (1982) was used to generate turbulent spots. This technique relies on the dependence of viscosity on temperature, as is easily seen by evaluating the x-momentum equation at the wall,

$$\rho v_w \left[ \frac{\partial u}{\partial y} \right]_w = \mu \left[ \frac{\partial^2 u}{\partial y^2} \right]_w + \frac{d\mu}{dT} \left[ \frac{\partial T}{\partial y} \right]_w \left[ \frac{\partial u}{\partial y} \right]_w$$

where it has been assumed that  $dp/dx \approx 0$ . The term on the left-hand side of the relation is retained to illustrate the analogy between suction/blowing and heating/cooling at the wall, i.e.,

$$v_w \sim - \frac{1}{\rho} \frac{d\mu}{dT} \left[ \frac{\partial T}{\partial y} \right]_w$$

In water, heating is analogous to suction since  $d\mu/dT < 0$ .

The equivalent wall velocity,  $v_w$ , may be related to known quantities by employing the boundary-layer concept in which it is assumed that the thermal thickness,  $\delta_t$ , is small compared to the streamwise extent of the heater,  $L$ . Non-dimensionalizing the equivalent wall velocity by the friction velocity,  $u_\tau$ , we find

$$\frac{v_w}{u_\tau} \sim \frac{d(\log \mu)}{d(\log T)} \frac{\Delta T}{T_\infty} \left[ \frac{Pr}{\sqrt{C_f} Re_L} \right]^{\frac{1}{3}} \quad (2.1)$$

where the following relations have been used,

$$\left[ \frac{\partial T}{\partial y} \right]_w \sim - \frac{\Delta T}{\delta_t}, \quad \delta_t \sim \sqrt{\kappa L / u_\tau}, \quad u_\tau \approx \frac{\tau_w}{\mu} \delta_t$$

It can be expected that relation (2.1) will hold in a turbulent boundary layer as well as in a laminar boundary layer if the thermal thickness,  $\delta_t$ , lies within the viscous sublayer.

It is convenient to express the overheat,  $\Delta T$ , in terms of the total power supplied to the heater,  $Q_T = V^2/R$ , where  $V$  is the voltage across the heater and  $R$  is the impedance of the heater. The total power is the sum of that supplied to the fluid,  $Q_f$ , plus that lost to the substrate,  $Q_s$ .

$$Q_T = Q_f \left[ 1 + Q_s/Q_f \right] \quad (2.2)$$

Using the Fourier conduction law and the relations used to derive (2.1), the rate at which heat is supplied to the fluid,  $Q_f$ , can be expressed in terms of  $\Delta T$ , the dimensions of the heated- element, and the local characteristics of the fluid and of the flow condition. Alternatively, Lighthill's formula can be used [Lighthill (1950); see also Liepmann (1958)]. Assuming a top-hat distribution for the wall temperature in a laminar boundary layer, and  $L \ll x$ , Lighthill's formula yields

$$Q_f = 0.807 k \Delta T b (Pr Re_L^2 C_f)^{\frac{1}{3}} \quad (2.3)$$

where  $k$  is the thermal conductivity of the fluid, and  $b$  is the span of the heater.

Therefore, the equivalent wall velocity may be conveniently expressed in term of the total power dissipated in the heated- element. Combining relations (2.1), (2.2), and (2.3), one may define a non-dimensional equivalent wall velocity,

$$\Upsilon \equiv \frac{d(\log \mu)}{d(\log T)} \frac{V^2}{R k T_\infty b \left[ 1 + Q_s/Q_f \right] Re_L \sqrt{C_f}} \sim \frac{v_w}{u_\tau} \quad (2.4)$$

The importance of substrate heating depends on the forcing frequency,  $\omega$ ,

$$Q_s \sim k_s \frac{\Delta T}{\sqrt{\kappa_s/\omega}} b L$$

Thus,

$$\frac{Q_s}{Q_f} \sim \frac{k_s}{k} \left[ \frac{L^2 \omega}{\kappa_s} \right]^{\frac{1}{2}} \left[ Pr Re_L^2 C_f \right]^{-\frac{1}{3}}$$

The use in water of a lucite substrate at the nominal conditions of the current experiments (described below) yields  $Q_s/Q_f$  of order  $10^{-1}$ .

The magnitude of the flow perturbation introduced by the heated-element depends not only on the equivalent wall velocity, but on the depth of penetration of the thermal boundary layer into the velocity boundary layer as well,

$$\delta_t \sim \left[ \frac{\kappa \mu L}{\tau_w} \right]^{\frac{1}{3}}$$

The characteristic thickness of the velocity boundary layer is taken to be  $\sqrt{\nu x / U_\infty}$ . Therefore, a dimensionless parameter,  $\Phi$ , is defined which characterizes the penetration of the thermal boundary layer into the velocity boundary layer,

$$\Phi \equiv \left[ Pr^{-1} \frac{L}{x} \right]^{\frac{1}{3}} \sim \frac{\delta_t}{\delta} \quad (2.3)$$

Representative values are given below for the two parameters  $\Gamma$  and  $\Phi$  that proved successful in forcing disturbances ranging from Tollmien-Schlichting waves to turbulent spots.

A heated-element of streamwise length 0.75 cm and of span 1.0 cm was flush-mounted 5.0 cm from the leading edge. At a nominal operating speed of 150 cm/sec, the streamwise location of the heater approximately corresponds to the position of the critical Reynolds number (for the Blasius profile,  $Re_{\delta^*_{crit}} \approx 550$ ).

The application of a 1.25-volt, 30-msec pulse to the 0.06-ohm, stainless-steel heated-element produced a turbulent spot whose virtual origin was located approximately 25 cm downstream of the leading edge (see Section 4.1). The minimum required duration of the heater pulse was found to correspond approximately to the characteristic time  $L/u_t$ . Values of the parameters  $\Upsilon$  and  $\Phi$  used to generate such spots were  $\approx 0.04$  and  $\approx 0.3$ , respectively. Lowering  $\Upsilon$  to  $\approx 0.03$  while holding  $\Phi$  fixed resulted in growing disturbances that did not exhibit turbulent behavior as far downstream as 70 cm.

Liepmann et al. (1982) and Nosenchuck (1982) employed a full-span heater that was flush-mounted 5 cm from the leading edge (a 4:1 ellipse). The chord of the heated-element was 0.25 cm. At a nominal free-stream speed of 120 cm/sec, the heater was located near the position of the critical Reynolds number. One objective of those experiments was to demonstrate the ability of the heating strip to excite Tollmien-Schlichting (T-S) waves, and the element was therefore heated sinusoidally at an appropriate frequency ( $\sim 40$  Hz). Using values of the forcing parameters,  $\Upsilon$  and  $\Phi$ , of 0.01–0.02 and 0.2, respectively, T-S waves whose rms wall-shear fluctuations were of the order  $10^{-2} \bar{\tau}_w$  were observed at a station located 20 cm downstream of the leading edge. Note that this streamwise position approximately corresponds to the virtual origin of the spots generated in the present experiments when the non-dimensional forcing level,  $\Upsilon$ , was approximately equal to 0.04.

It is noted that the pressure gradient is slightly adverse in the shoulder region of the elliptical leading edge [see for example, Hess and Smith (1966)]. The magnitude of the gradient, which depends on the eccentricity of the ellipse and on the stagnation-point location, affects the growth rates of small disturbances. Since the heaters in both sets of experiments were located near the shoulders of the leading edges, the overall amplification between the heaters

and the measuring stations would be expected to be greater than that for a strictly Blasius profile. Therefore, it would be required to use higher values of  $\Upsilon$  in a truly Blasius boundary layer than those cited above.

## 2.5. Tandem-Manipulator Configuration

Shown in Figure 2.3 is a schematic of a typical tandem-manipulator configuration. Also included is a table of the characteristic dimensions used in other investigations. The chord,  $L$ , of each manipulator blade is on the order of the local boundary-layer thickness,  $\delta_m$ , and the blades are usually placed parallel to the wall at heights,  $h$ , ranging from  $0.4 - 0.8 \delta_m$ . It is conventional to measure the boundary-layer thickness,  $\delta_m$ , at the trailing edge of the last manipulator blade. The effectiveness of the device appears to be relatively insensitive to the streamwise spacing of the two blades,  $s$ . Typically, the blades are spaced  $5 - 10 \delta_m$  apart.

In the present experiments, the chord length and thickness of the blades were fixed,  $L = 1.27$  cm and  $t = 0.20$  mm. The streamwise separation,  $s$ , of the blades was 3.8 cm in the turbulent boundary-layer experiments and 7.6 cm in the turbulent spot experiments. Each blade was cut to its desired length, approximately 28 cm, from a long strip of steel shim-stock. The edges and both sides of the blades were subsequently sanded with 500-grit sandpaper.

The blades were then fastened to a bow-shaped, stainless-steel support by first squeezing its tips toward each other using a wide furniture clamp (much like stringing a bow). The ends of each blade were then secured to clamps that were connected to the two ends of the bow-shaped support. The position of each clamp was adjustable, thus allowing the blades to be aligned into one plane. That portion of the clamps located below the manipulator blades prevented the blades from being traversed closer than 1.0 mm from the surface of the flat-

plate model.

A brass rod, 0.64 cm in diameter, was mounted to the bow-shaped support so that its axis was perpendicular to the plane of the manipulator blades. This rod exited through an O-ring in the top of the test section, and was secured to a traversing mechanism located outside the test section. The traverse was mounted such that its traversing axis was normal to the surface of the flat-plate model. Provision was made to permit small adjustments in the angle of the brass rod (and, consequently, the bow-shaped support and manipulator blades) with respect to the normal of the flat-plate model. The angle was adjusted using gauge blocks to ensure that the plane of the manipulator blades was parallel to the working surface, and that the leading edges of the blades were perpendicular to the flow direction.

The leading edge of the first manipulator blade was observed to be more susceptible to vibration than were other portions of the device. The problem was eliminated when the clamps were adjusted to produce a greater tension along the leading edge than along the trailing edge. Furthermore, a compromise was required between the desire to achieve high Reynolds number and the tendency for the blades to vibrate at high speeds. Free-stream velocities were maintained below 190 cm/sec in all experiments.

## **2.6. Hot-Film Wall-Shear Sensors**

Arrays of wall-shear sensors manufactured at GALCIT as well as individual wall-shear sensors manufactured by TSI were used in the present experiments. All sensors were flush-mounted on the wall of the flat-plate model, and were oriented to detect the streamwise component of wall shear. They were maintained at a constant temperature by the bridge circuitry described below. The operating resistance,  $R_{hot}$ , was typically adjusted to a value 7.0% higher than the

resistance at room temperature,  $R_{cold}$ .

Shown in Figure 2.4 is a photograph of a completed array of sensors. The sensors were manufactured at GALCIT using a process that was developed during the present study (see the Appendix for details). The streamwise and spanwise dimensions of both types of sensors were the same, 0.13 mm by 1.02 mm, respectively. The cold resistance,  $R_{cold}$ , and the thermal coefficient of resistivity,  $\gamma$ , of both types of sensors were also comparable ( $R_{cold} \approx 5$  ohms,  $\gamma \approx 0.004$  ohms/degree-Kelvin). The GALCIT sensors were made of tin and were deposited on a glass-reinforced epoxy-resin substrate, while each TSI sensor was made of platinum and was deposited on a slender quartz rod. The GALCIT sensors were used in many of the experiments. However, the substrate later separated from the stainless steel ring onto which it was epoxied, and the experiments were completed using several TSI sensors that had been employed in a previous investigation.

The sensors are calibrated based on a simplified form of Lighthill's formula. It is assumed that the wall temperature is constant over an effective length,  $L$ , and that  $L \ll x$ , where  $x$  is the streamwise location of the sensor. With these assumptions, the functional relationship between the wall shear and the total power supplied to the (constant resistance) element is

$$V^2 = C_1 \tau_w^{\frac{1}{3}} + C_2$$

where  $V$  is the voltage across the sensor, and  $C_2$  represents the heat supplied to the substrate. The constant  $C_1$ , which depends on the thermal and geometrical characteristics of the sensor and on the properties of the fluid, represents the sensitivity of the sensor to wall-shear changes.



## 2.7. Cylindrical Hot-Film Velocity Sensors

A cylindrical hot-film sensor, manufactured by TSI, was used to obtain velocity profiles in the turbulent boundary layer (see Section 3.1). Its operating principle, like the hot-wire, is based on King's law. That is, it is assumed the heat supplied to the constant-temperature cylindrical sensor is related to the local Reynolds number,  $Re_d$ , by

$$V^2 = C_3 Re_d^{\frac{1}{2}} + C_4$$

where  $C_3$  and  $C_4$  are constants, and  $d$  is the diameter of the sensor.

## 2.8. Circuitry for Wall-Shear and Velocity Sensors

A schematic of the bridge circuit used to maintain all hot-film sensors at constant temperature is shown in Figure 2.5. Sixteen circuits were constructed using standard printed-circuit (PC) manufacturing techniques.

The main feature of the circuit is the use of an operational amplifier to provide voltage feedback. Current is supplied to the bridge by a 2N2270 transistor. For the resistance values used in the two upper legs of the bridge, 40 and 400 ohms, the feedback ensures that the operating resistance of the sensor, including the resistance of the leads, is one-tenth (40/400) the resistance of the 100-ohm potentiometer setting.

Two automotive batteries served as low-noise,  $\pm 12$ -volt power supplies for the circuits. A typical noise level for the circuits was 5 mV peak-to-peak, which is comparable to the 2.5 mV quantization error introduced by A/D conversion (see Section 2.9). Other features of the circuit include a sensor-saving, current-limiting resistor (typically 25-ohms) located between the 12-volt supply and the

collector of the 2N2270 transistor, an additional operational amplifier on the output of the bridge to isolate the circuit from other instruments, and low-pass filters on the output of each circuit to prevent aliasing during data acquisition.

## **2.9. Data-Acquisition and Processing Systems**

A microprocessor-based data acquisition and control system was constructed during the course of the present investigation. Provided below is a brief summary of its salient features. A more detailed description is given by Robey (1986).

Shown in Figure 2.6 is a functional schematic of the system. The microprocessor itself is comprised of an 8085-based central processing unit (CPU), 16K of random access (RAM) memory, 16K of erasable programable memory (EPROM), a direct-memory access (DMA) controller, a floppy-disk drive controller, four general-purpose A/D channels, four D/A channels, and various timers and counters.

Other components that are used with the system include an Advanced Electronics Design 6200LD dual floppy-disk drive and a 16-channel, 12-bit, differential-input data-acquisition system (DAS) built around an Analog Devices 50-kHz A/D module. Each channel of the DAS is capable of sampling signals whose amplitude lies in the range 0-10 volts, thus yielding a 2.5 mV resolution for each 12-bit data word. Data sampled by the DAS were transferred to one of the floppy-disk drives via RAM memory using a double-buffering technique. The data were stored on 8-inch floppy disks in the RT-11 file format. All data processing was subsequently performed on a Digital PDP 11/44 computer system.

## Chapter 3

### **MANIPULATOR EFFECTS ON WALL SHEAR IN A TURBULENT BOUNDARY LAYER**

One objective of the present experiments is to obtain a better understanding of the mechanisms responsible for the wall-shear reductions observed downstream of tandem manipulators. It is also of importance to clarify the discrepancies that exist regarding the magnitude of the attainable net drag reduction.

Arrays of flush-mounted films, maintained at constant temperature, are presently used to obtain wall-shear data. Comparisons of mean wall-shear distributions are made with distributions obtained in two independent investigations in which skin-friction balances were employed. Such comparisons not only provide a basis for assessing the prospects of attaining net drag reductions, but also provide a foundation for subsequent turbulent spot experiments in which attempts are made to understand the effects of the manipulator blades in terms of large-scale turbulent structure.

#### **3.1. Undisturbed Boundary Layer Behavior**

A turbulent boundary layer was produced by appropriately adjusting the trailing-edge flap, whose angle,  $\varphi$ , determines the position of the leading-edge stagnation point. For positive values of  $\varphi$ , in which the flap is rotated toward the active side of the flat-plate model, the stagnation point lies on the active surface of the model. For such flap angles, the flow is laminar over the stream-wise extent of the model for  $U_\infty \lesssim 200$  cm/sec. (The contamination regions that grow from the two edges of the model meet approximately at the hinge point of the trailing-edge flap.) Early transition occurs when the flap is set to non-

positive angles. For the turbulent boundary-layer experiments, the flap angle was set to values in the range  $-3 < \varphi < -5$  degrees.

Profile measurements were made of the streamwise component of velocity using a cylindrical hot-film sensor (see Section 2.7). Quantities of interest include: (1) the boundary-layer thickness at the trailing edge of the downstream manipulator blade,  $\delta_m$ , used as a non-dimensionalizing parameter; and (2) the magnitude of the unmanipulated wall shear, used as a basis for calibrating the wall-shear sensors. Shown in Figure 3.1 is an unmanipulated velocity profile measured at station  $x$  40 cm, just upstream of the leading edge of the tandem manipulator blades. Unless otherwise stated, the nominal free-stream velocity for the turbulent boundary-layer experiments was 162 cm/sec. The corresponding range of Reynolds numbers between the manipulator and the downstream-most measuring station was  $6.5 \times 10^5 < Re_x < 1.2 \times 10^6$ .

The boundary-layer thickness at the trailing edge of the second manipulator,  $\delta_m$ , was approximately 0.69 cm. This value is used to non-dimensionalize the height of the manipulator and various streamwise distances. Streamwise distances are typically measured from the trailing edge of the last manipulator blade, i.e., from  $x = x_m$ , where  $x$  is measured from the leading edge of the flat-plate model.

An estimate of the mean wall shear can be made using one of a number of proposed correlations that relate the mean wall shear to such local integral quantities as the momentum-thickness Reynolds,  $Re_\theta$ , and the shape factor,  $H$ . The following correlation [which closely approximates the wall-shear data compiled by Coles and Hirst (1968)] was used to establish the magnitude of the unmanipulated wall shear,

$$C_f \approx \frac{0.3 e^{-1.33H}}{(\log_{10} Re_\theta)^{1.74 + 0.31H}} \quad (3.1)$$

For the profile in Figure 3.1, the correlation predicts a value for  $C_f$  of approximately 0.0040.

### 3.2. Manipulated Wall-Shear Behavior

The effects of tandem manipulators on turbulent wall shear are investigated using an array of flush-mounted sensors located downstream of the manipulator. The variation of mean wall shear with manipulator height,  $h$ , at streamwise stations in the range  $8 < (x - x_m)/\delta_m < 42$  are shown in Figures 3.2 and 3.3. The location  $(x - x_m)/\delta_m = 42$  is the most downstream position at which measurements could be made. The repeatability of the measurements for any given manipulator height is indicated by the error bars. The height of the manipulator was varied in a random fashion with frequent returns to the reference height,  $h = 2.7\delta_m$ . Averages were computed from 16-second records that were sampled at a 1-kHz rate (per channel).

No significant wall-shear reductions are apparent for  $h \gtrsim 2\delta_m$  (over the streamwise region considered). As the manipulator blades are traversed closer to the wall, reductions are observed to occur first at the downstream-most stations. However, the most significant wall-shear reductions occur immediately downstream of the manipulator when the blades are close to the wall. At each station there exists a manipulator height at which the wall-shear reduction is a maximum. The magnitude of this maximum wall-shear reduction is observed to decrease monotonically with increasing distance from the manipulator, and the corresponding manipulator height at which the maximum reduction occurs increases monotonically with downstream distance.

Streamwise distributions of wall shear for fixed manipulator heights are given in Figures 3.4 through 3.6. Comparisons are also made with data obtained using skin-friction balances, under comparable conditions, as reported by Mumford and Savill (1984) and Lemay et al. (1985). Considering the experiment-to-experiment variations in manipulator configuration (e.g.,  $h/\delta_m = 0.61, 0.50,$  and  $0.48$  in Figure 3.5) and flow condition, the agreement is good.

For a fixed manipulator height the wall shear is observed to initially decrease with downstream distance. A minimum is attained whose streamwise position and magnitude depend on the manipulator height. As the manipulator blades are moved closer to the wall, the minimum deepens and moves upstream toward the manipulator. Just downstream of the minimum, the wall shear recovers rather rapidly (over the region, say,  $20-40\delta_m$  at  $h/\delta_m \approx 0.5$ ), and then slowly approaches its undisturbed level.

The mean wall-shear levels in the recovery region are not in agreement with those inferred by Plesniak and Nagib (1985) who report wall-shear reductions as large as 25% at downstream distances as great as  $140\delta_m$ . Of further concern is the qualitative behavior of their distributions at large distances. For  $(x-x_m) \gtrsim 100\delta_m$ , some of their distributions tend toward the undisturbed wall-shear levels, while others remain at low levels or even decrease with increasing distance.

### **3.3. Importance of the Manipulator Wake**

Various mechanisms have been proposed for the observed wall-shear reductions. Since the manipulator blades are considered to be low-drag devices, the importance of the momentum deficit in the wake has generally been ignored. Most proposals attempt to explain the effects in terms of large-eddy behavior. It has been suggested that the manipulator blades and/or their wakes hamper the

ability of the large-scale eddies to transport high-momentum fluid from the free-stream into the boundary layer, where this fluid is mixed and subsequently decelerated. For example, Guezennec and Nagib (1985) report a steepening of the intermittency profiles, which suggests that the manipulator may alter the behavior of the large eddies. It has been proposed that such changes are due to an interaction between the vorticity in the large eddies and the vorticity that is shed from the blades.

The importance of the momentum deficit in the wake, which represents the drag of the device, can be established by comparing the momentum thickness of the wake,  $\theta_m$ , with a characteristic change in the momentum thickness of the undisturbed boundary layer,  $\Delta\theta$ . The latter quantity is representative of the force that the wall exerts on the fluid over that region of the flow in which the wake of the manipulator is incorporated into the boundary layer. A lower bound can be established for the drag of the device by computing the laminar flat-plate value [see, for example, Anders et al. (1984) and Mumford and Savill (1984)],

$$\theta_m \approx \frac{4(0.664)L}{\sqrt{Re_L}} \quad (3.2)$$

where the factor 4 arises from the four sides of the two manipulator blades.

The characteristic change in the momentum thickness of the undisturbed boundary layer may be written,

$$\Delta\theta \approx \frac{\Delta\theta}{\Delta x} \Delta x \approx \frac{C_f}{2} \frac{\Delta x}{\delta_m} \delta_m \quad (3.3)$$

Comparing (3.2) with (3.3), a non-dimensional device-drag parameter can be defined in terms of known quantities,

$$\frac{\theta_m}{\Delta\theta} \approx \frac{5.3}{C_f \frac{\Delta x}{\delta_m}} \left[ \frac{\frac{L}{\delta_m}}{\text{Re}_\theta \frac{\delta_m}{\theta_m}} \right]^{1/2} \quad (3.4)$$

The non-dimensional streamwise distance  $\Delta x/\delta_m$  represents the streamwise region over which a distinct wake profile is embedded in the mean velocity profile. Based on the velocity profiles reported by Corke (1981) and by Lemay et al. (1985), this region is observed to persist for 20–40 $\delta_m$ . A nominal value of 30 $\delta_m$  is assumed, although the conclusion is not sensitive to the exact value used. Given  $\text{Re}_\theta$ , accepted correlations can be employed to relate  $C_f$  and  $\delta/\theta$  to the local momentum-thickness Reynolds number and (say) shape factor, H [e.g., eqn. (3.1) for  $C_f$ ]. Assuming a lower bound for the chord of the manipulator,  $L/\delta_m = 1$ , the drag parameter assumes the following values,

$$\frac{\theta_m}{\Delta\theta} \approx \begin{cases} 0.50, & \text{for } \text{Re}_\theta = 1000 \\ 0.25, & \text{for } \text{Re}_\theta = 6000 \end{cases}$$

Therefore, the tandem manipulator is **not** a low-drag device. The momentum deficit in the wake of the device can be expected to strongly influence the behavior of the wall shear. A discussion of the consequences of this result is given in Chapter 6.

### 3.4. Prospects for Net Drag Reduction

Given the wall-shear reductions determined by direct measurements, it is of interest to establish an upper bound for the attainable net drag reduction. That is, if it is assumed that the drag of the device is given by its laminar value, what net drag reductions can be expected? Although the direct wall-shear



measurements were made at relatively low momentum-thickness Reynolds numbers ( $1000 < Re_\theta < 2400$ ), net drag reductions as large as 20% have been reported at  $Re_\theta = 2000$ .

The spatially-averaged wall-shear reduction required to overcome the laminar drag of the device is given in Figure 3.7 as a function of the distance from the manipulator. That is, large wall-shear reductions are necessary to overcome the drag of the device when the averaging distance is small. The calculations were made for two chord lengths,  $L/\delta_m = 1.0$  and  $2.0$ .

The effects of "shielding" were also included in the computation. It has been proposed that the drag of the second blade,  $D_2$ , is lower than the drag of the first,  $D_1$ , because the second blade is embedded in the wake of the first blade. Drag measurements by Mumford and Savill (1984) suggest that  $D_2 \approx 0.85 D_1$ . The shaded regions in Figure 3.7 represent values of  $D_2$  in the range  $0.50 < D_2/D_1 < 1.0$ .

Based on the lowest values of wall shear given in Figure 3.5 ( $h/\delta_m \approx 0.5$ ), and taking into account possible reductions between the first and second blades (assumed to be 20% below the undisturbed value -- a generous provision), it is found that the wall-shear reduction overcomes the drag of the device at  $\Delta x/\delta_m \approx 40$  (assuming 50% shielding). If it is assumed that the wall-shear reduction remains unchanged downstream of the last measuring station,  $\Delta x/\delta_m \approx 63$ , the net drag reduction is only 5% at  $\Delta x/\delta_m = 100$ . Since the present estimate of the net drag reduction is admittedly optimistic, it is more likely that small net drag reductions ( $\sim 5\%$ ) may be attainable at very large downstream distances ( $> 100\delta_m$ ). It is noted that for  $\Delta x/\delta_m \geq 50$ , the spatially-averaged wall-shear reduction is not particularly sensitive to the height of the manipulator.

Also given in Figure 3.7 are the average wall-shear reductions required to achieve a 20% net drag reduction. For  $L/\delta_m = 1.0$  and 50% shielding, it is necessary to achieve a 27% average wall-shear reduction over  $100\delta_m$ . The present hot-film measurements and the skin-friction balance measurements [i.e., Mumford and Savill (1984) and Lemay et al. (1985)] indicate that this requirement grossly exceeds the possible average wall-shear reduction.

## Chapter 4

### MANIPULATOR EFFECTS ON TURBULENT SPOTS

The present experiments focus on the effects of tandem manipulator blades on the turbulent spot, employed as a prototype structure for the organized, large-scale motions in the turbulent boundary layer. Attention is focused on the ensemble-averaged wall-shear behavior along the plane of symmetry of the turbulent spot. Results are presented for isolated spots propagating in ambient laminar, transitional, and turbulent boundary layers.

#### 4.1. Undisturbed Turbulent Spot Behavior

Prior to an examination of manipulator effects on turbulent spots, the general characteristics of unmanipulated spots that were generated in the present experiments are discussed.

**4.1.1. *Turbulent Spot Generation.*** The flush-mounted heated-element described in Section 2.4 was used to trigger all spots. One advantage of using this triggering technique is the degree of control one has over the amplitude of the disturbance. The effect of an increase in the amplitude of the heater pulse is illustrated in Figures 4.1 and 4.2. For low levels of forcing one would expect the phase velocity and growth rate of small-amplitude disturbances to follow approximately that predicted by linear stability theory. Once a critical amplitude is attained (e.g., in the region  $48 < x < 68$  cm in Figure 4.1) a local breakdown of the laminar flow occurs, and a turbulent spot rapidly develops from the breakdown. Further increases in the forcing amplitude cause the breakdown region to occur farther upstream.

For the nominal operating condition of the experiments,  $U_\infty = 150$  cm/sec and  $(Re_x)_m = 7 \times 10^5$ , it was necessary to apply a 1.25-volt pulse to the 0.06-ohm heated-element to ensure that the virtual origin of the spot (see Section 4.1.3) was located well upstream of the manipulator device. The virtual origin of the spot was observed to be essentially independent of the pulse duration for pulse widths greater than several milliseconds. (The use of pulse widths greater than 150 msec was avoided because of the disastrous effect of dc heating at comparable levels on the epoxy-held heated-element, an effect confirmed accidentally.)

**4.1.2. Ensemble-averaging Technique.** Of interest is the ensemble-averaged behavior of turbulent spots. A typical ensemble-averaged wall-shear time history of a turbulent spot is shown in Figure 4.3. Ensemble-averaged spots were obtained by recording the time history of  $N$  spots, with a delay of four seconds between heater pulses to allow the flow to relax, and averaging the  $N$  wall-shear points at each recorded instant of time. The rising edge of the heater pulse was used as a time reference for the ensemble averaging, and no attempt was made to align the individual traces based on, say, the arrival of each leading edge [e.g., Wygnanski et al. (1976)].

The amount of variation in the arrival times of individual spots was determined by noting the time at which the skin-friction coefficient,  $C_f$ , first exceeded the arbitrary value 0.002 for each of the  $N$  events. As an example, at a free-stream speed of 150 cm/sec the mean of 64 arrival times was 0.601 seconds at station  $x = 52$  cm with a standard deviation of 0.015 seconds.

**4.1.3. Interface Celerities and Virtual Origin.** Interface celerities in the near-wall region of turbulent spots are determined from wall-shear histories recorded simultaneously from sensors positioned along a line in the streamwise direction. Such information is conveniently represented in the form of an  $x$ - $t$  diagram in which the arrival times of the leading and trailing interfaces are

plotted against the corresponding streamwise stations of the sensors. All present measurements of near-wall interface celerity were made along the plane of symmetry of the turbulent spot.

The x-t diagram for a typical turbulent spot is shown in Figure 4.4. One least-squares straight line is constructed for the set of leading-edge points, and another for the set of trailing-edge points. The slope of each line represents the celerity of the interface. From Figure 4.4, the interface celerities for the leading and trailing interfaces are  $0.90U_{\infty}$  and  $0.56U_{\infty}$ , respectively.

The virtual origin is defined as the intersection of the two lines in the x-t diagram. For the spot represented in Figure 4.4, the virtual origin lies 19 cm downstream of the heating element (which is located 5 cm downstream of the leading edge of the flat-plate model). Celerities are noticeably affected only when the forcing level is decreased to the point where the virtual origin lies near, or downstream of, the measuring stations ( $x > 48$  cm). At such low forcing levels, the disturbances detected by the sensors can not be considered to be fully developed spots. Furthermore, large forcing levels are not desirable because of the possible effect of edge contamination on the growth of the spot, particularly at the downstream-most station. The virtual origins for all spots were positioned 15-20 cm downstream of the heated-element.

A pictorial representation of the criteria used to determine the arrival times of the leading and trailing interfaces is shown in Figure 4.5. Five points along the rise of the leading edge and five points along the decay of the trailing edge are fit with a least-squares straight line and a least-squares exponential curve, respectively. The arrival time of the leading edge is defined as the time at which the wall shear along the linear fit attains the value of the first local maximum in the trace. The arrival time of the trailing edge is defined as the time at which the wall shear along the exponential fit attains the last local maximum value in

the trace. Because of the steepness of the fits near the turbulent region of individual spots, the results are relatively insensitive to the particular wall-shear levels that are specified (e.g., the first and last relative maxima).

**4.1.4. *Spanwise Extent.*** As reported by Wygnanski et al. (1980) the spanwise growth of the spot is weakly dependent on the Reynolds number. Over the Reynolds number range  $605 < Re_{\delta^*} < 1520$ , the half-angle,  $\alpha$ , increases from 9.3 degrees at the lowest Reynolds number to 10.0 degrees at the highest. Since only a representative value of the spreading angle is presently required, it is assumed that  $\alpha = 10$  degrees.

The virtual origin for the spanwise extent of the spot, which does not necessarily coincide with the virtual origin for the streamwise extent, was determined by adjusting the forcing level until the spanwise extremity of the spot was evident on the output of the sensor at  $(x, z) = (52.8 \text{ cm}, 3.66 \text{ cm})$ . At this forcing level the virtual origin in  $z$  was found to lie only 3 cm downstream of the virtual origin in  $x$ . Considering that only an estimate of the spanwise origin is presently required, and that the experiments were performed over a relatively narrow range of Reynolds number, it is assumed that the the virtual origin in  $z$  coincides with the virtual origin in  $x$  for all spots.

**4.1.5. *Estimated Thickness.*** The apex height, or maximum thickness,  $\delta$ , of the spot is used as a characteristic length for non-dimensionalizing such quantities as manipulator height. Possible means of estimating the thickness include: 1) assuming that the spot grows like a comparable turbulent boundary layer, say,  $\delta \sim (x - x_0)^{4/5}$  as suggested by Schubauer and Klebanoff (1955) and later supported by Wygnanski et al. (1982); or 2) assuming that the spot grows in the conical sense,  $\delta \sim (x - x_0)$ , which is consistent with the work of Cantwell et al. (1978).

For a nominal spot in the present experiments, the two methods yield apex estimates of 0.62 cm and 0.39 cm, respectively, at station  $x = 50$  cm. Based on the height attained by injected dye in a preliminary investigation, the former method is employed for estimating the apex height of the spots.

**4.1.6. Comparison with Other Near-Wall Measurements.** The characteristics of the ensemble-averaged wall-shear time histories are consistent with the near-wall velocity traces reported by Wygnanski et al. (1976) and Cantwell et al. (1978). As Wygnanski observed, there exists an abrupt acceleration of the fluid in the near-wall region as the leading interface of the spot passes a given measuring station, followed by a nearly monotonic acceleration until a maximum velocity is achieved near the trailing edge of the spot. The tendency for the mean velocity at a point near the wall to increase as the spot passes by is consistent with the rise in the mean wall-shear presently observed.

One interesting feature of the present wall-shear traces, and of the velocity traces of the two investigations cited above, is the relative minimum (or plateau region) that occurs just upstream of the leading interface. Since this minimum occurs near the streamwise position of the large vortical structure deduced by Cantwell et al. (1978), it is conjectured that the minimum is related to the passage of the structure. More detailed discussions related to the large vortex structure appear in Sections 4.3 and 6.2.

## **4.2. Effects of a Tandem-Blade Manipulator**

The effects of a typical tandem manipulator on the wall shear of a turbulent spot propagating in a laminar boundary layer were investigated. Although an isolated spot may not be an ideal model for the large-scale eddy in a turbulent boundary layer, similarities between the two flows in the presence of manipulators are sought in hopes of better understanding the behavior of the organized

motions in turbulent boundary layers. Possible connections between the large scales and the wall-shear behavior are of particular interest.

Employed in the experiment was a combination of the heated-element for generating spots, traversable manipulator blades, and multiple wall-shear sensors. The manipulator blades were first positioned at a reference height, and a series of  $N$  spots were subsequently forced. Unmanipulated, reference turbulent spots are defined as those spots forced when the manipulator height was approximately 4 cm above the flat-plate model. This reference height corresponds to approximately 7 nominal spot heights. No significant changes in the wall-shear behavior of ensemble-averaged spots were observed when the manipulators were lowered from the reference position to a height 1.0 cm above the plate. The blades were then lowered to various positions closer to the wall, and  $N$  spots were forced at each height. Ensemble-averages presented in the remainder of this chapter were constructed for  $N = 99$ . To ensure that the effects of possible drift did not affect the results, measurements were taken periodically with the manipulator blades positioned at the reference height.

It is noted that in all experiments the trailing edge of the manipulator was located 42.5 – 50.0 cm from the leading edge of the flat-plate model. The chord,  $L$ , of each blade was 1.27 cm and the blade-to-blade spacing,  $s$ , was 7.6 cm.

*4.2.1. Spot Behavior Downstream of Manipulator.* The general effect of the manipulator blades on the wall shear of isolated turbulent spots is apparent from the comparisons made in Figure 4.6. Plotted are ensemble-averaged wall-shear traces obtained from the output of two sensors located at  $(x - x_m) = 2\delta_m$  and  $(x - x_m) = 12\delta_m$ , where  $x_m$  is the streamwise position of the trailing edge of the manipulator, and  $\delta_m$  is the estimated apex height of the spot at  $x = x_m$ . Each of the two plots in Figure 4.6 contains two wall-shear traces: one for which the manipulator blades were positioned at the reference height and one for



which the blades were positioned at  $h = 0.65\delta_m$ . The latter height was the lowest that the blades could be traversed without the wake of the blades tripping the otherwise laminar boundary layer at the downstream-most measuring station.

The most apparent effect of the manipulator blades is the dramatic reduction in wall shear near the leading edge of the turbulent spot. The effect appears to diminish toward the trailing interface. Since the manipulator blades are large-scale devices, it is not surprising that the effect is most noticeable in the region occupied by the horseshoe vortex. Plotted as a function of blade height,  $h$ , in Figure 4.7 is the mean wall shear, non-dimensionalized by the mean wall shear of the undisturbed spot. Mean wall shear was computed for the region of the traces located between the arrival of the leading interface and the arrival of the trailing interface for the reference spot. It is observed that the effect on the wall shear is measurable only for  $h < 2\delta_m$ . As in the fully turbulent boundary layer the wall-shear reduction is enhanced as the manipulator moves closer to the wall. However, at a fixed streamwise station it was not possible to identify a height at which a maximum wall-shear reduction occurs, as in the turbulent boundary layer, because of the occurrence of transition for the lower manipulator heights.

Despite the adverse effect of the manipulator wake on the laminar boundary layer, the blades were lowered to  $h = 0.49\delta_m$ . At this height the flow just downstream of the second manipulator blade was turbulent, indicating that transition occurred between the first and second manipulator blades. Turbulent spots were subsequently forced as before and ensemble-averages were again taken. As shown in Figure 4.8, the wall shear is reduced significantly, particularly near the leading-edge region of the spot. The existence of large, fluctuating shear levels in the ambient flow does not appear to noticeably alter the effect of the blades on the spot. However, since the origin of the spot is located well upstream of the

transition front, one might expect the spot to dominate any developing structures in the transition region. The effects of a spot merging with a turbulent boundary layer formed well upstream of the manipulator blades are described in Section 4.3.

It is noted that a laminar calibration was used to obtain the results for the turbulent spot in Figures 4.6 through 4.8. Because of the extrapolation of the calibration curve to high turbulent wall-shear values, the wall-shear levels of the turbulent spots in Figures 4.6 and 4.8 are lower than those observed in all other wall-shear traces of the spot (e.g., Figure 4.3). No extrapolation errors were introduced in the latter wall-shear traces since the calibration curves were constructed from both laminar and turbulent calibration points. From Figure 4.8, it is observed that the spatially-averaged wall shear of the spot is approximately equal to the mean wall shear of a fully turbulent boundary layer at a comparable Reynolds number. The skin-friction coefficient,  $C_f$ , for the ambient turbulent flow in Figure 4.8 should be closer to 0.004. However, the effect of the extrapolation error on the percentage change in the manipulated wall shear,  $C_f/C_{f_0}$ , as given in Figure 4.7, was found to be small (< 5% extrapolation error in the values of  $C_f/C_{f_0}$  presented for the turbulent spot).

**4.2.2. Near-Manipulator Spot Behavior.** In an effort to identify the mechanism(s) responsible for the observed wall-shear reduction near the leading edge of the spot, it was conjectured that an immediate interaction between the manipulator blades and the large vortex in the spot may occur. For example, does the interaction change the circulation of the vortex, or shift the location of the vortex within the spot? It is therefore of interest to investigate the behavior of the wall shear when the spot is travelling in the neighborhood of the manipulator blades. Three wall-shear sensors were located at stations  $(x - x_m) = -1.38L$ ,  $-0.58L$ , and  $0.22L$ , where  $L$  is the chord of each of the two blades. The

geometry of the tandem manipulator was the same as that used in the previous experiment. The first sensor was thus located  $0.38L$  upstream of the leading of the second blade, the second sensor was located directly under the blade, and the third sensor was located  $0.22L$  ( $0.38\delta_m$ ) downstream of the trailing edge.

From the traces in Figure 4.9 it is observed that the most dramatic wall-shear reduction occurs just upstream of the leading edge of the manipulator blade, where both the turbulent spot and the ambient laminar boundary layer are affected. Downstream of the leading edge of the blade, the wall-shear recovers rather quickly toward its undisturbed level. It is also observed that the arrival times of the leading and trailing edges of the spot are retarded.

Although it does appear that small changes do occur near the leading edge of the spot (e.g., the slow rise of the wall shear at  $(x-x_m)/L = -0.58$ ), the large wall-shear reductions observed near the leading edge of the spot at stations farther downstream, as in Figure 4.6, are not apparent when the spot is in the neighborhood of the manipulator blade. The wall-shear behavior of the spot and of the ambient laminar boundary layer is suggestive of a developing channel flow, where the manipulator blade acts much like the upper wall of the channel. The streamlines diverge in the region upstream of the blade as the fluid attempts to circumvent the channel, thus decreasing the wall shear in this region. The wall shear subsequently attempts to recover as the flow accelerates through the channel. The turbulent boundary layer exhibits a similar behavior near the manipulator blades (see Section 4.4), consistent with Mumford and Savill's (1984) observation in a fully turbulent boundary layer that "as the flow reaches the devices it moves outwards thickening by approximately one-third." Their observation was based on laser/incandescent illumination of injected smoke.

The presence of adverse pressure gradients can introduce errors in the magnitude of the wall shear due to the fact that the thermal boundary layer of the sensor is embedded in a velocity profile with curvature at the wall. Since the present calibrations are performed in the absence of mean pressure gradients, the subsequent use of the sensors in flows with non-zero pressure gradients may require corrections to the wall shear [see, for example, Brown (1967)]. However, for the present flow conditions and sensor geometry the correction term is small for favorable and moderately adverse pressure gradients. For example, the calibration curves constructed in the present experiments for zero pressure gradient overpredict the wall shear by roughly ten percent for a flow in which the equilibrium parameter,  $\beta$ , defined by Clauser (1954,1956) as  $(\delta^*/\tau_w)(dp/dx)$ , is of order 10. Corrections are negligible for  $\beta \ll 10$ . Therefore, the uncorrected wall-shear levels at station  $(x-x_m) = -1.38L$  in Figure 4.9 are slightly higher than the actual levels.

### 4.3. Entrainment of the Manipulator Wake

As discussed in Section 3.3, the momentum deficit introduced by the tandem manipulator is not small compared to an appropriate characteristic change in the momentum thickness of the undisturbed turbulent boundary layer. The wake is expected to be a prominent contributor to the observed wall-shear reductions.

It is conjectured that the dramatic wall-shear reductions that occur near the leading interface of the spot are due, in large part, to the entrainment of the wake of the manipulator. Shown in Figure 4.10 is a representation of the mean particle-path trajectories in an ensemble-averaged spot, as deduced by Cantwell et al. (1978). For clarity, the vertical scale is expanded by a factor of approximately four. Also provided in Figure 4.10 is a table of the relative entrainment

rates along various segments of the boundary of the spot.

It is observed that the streamwise position within the spot where the wall-shear reductions are most apparent coincides with the approximate location of the large vortex structure. As the wake is entrained along the upstream-facing boundary, it is incorporated into the region occupied by the vortex. Since the momentum of the entrained fluid from the wake is initially lower than the momentum of the fluid that is normally entrained, the overall deceleration of the entrained fluid due to turbulent mixing is consequently reduced. Since the deceleration of fluid within the boundary layer must be manifested in the shearing stresses at the wall (in the absence of mean pressure gradients), the wall shear is also reduced in the vicinity of the large vortex.

It is also noted that the region near the trailing interface is not affected by the wake of the manipulator, since the manipulator is always located well above the upper boundaries of this region. It is conjectured that if the spot were followed to greater downstream distances, or if the manipulator were positioned closer to the surface, wall-shear reductions would also be evident near the trailing interface of the spot.

A more complete discussion of the relevance of the structural model deduced by Cantwell et al. on the behavior of manipulated spots is given in Section 6.2.

#### **4.4. Turbulent Spot in an Ambient Turbulent Boundary Layer**

In an attempt to draw similarities between the manipulated turbulent spot and the manipulated turbulent boundary layer, individual spots were followed in a fully turbulent boundary layer. Shown in Figure 4.11 are ensemble-averaged wall-shear time histories of turbulent spots propagating in an ambient turbulent boundary layer. The lower two plots illustrate the behavior of the spot

near the manipulator, while the upper trace reflects its behavior well downstream of the manipulator.

It is first established that the spot can be followed in the turbulent flow for large downstream distances. The last measuring station (upper trace in Figure 4.11) is located approximately  $75\delta_m$  downstream of the heated-element. A similar conclusion was reached by Haritonidis et al. (1977).

Secondly, it is observed that at the downstream-most station the wall-shear reductions are enhanced near the leading interface of the spot compared to the reduction in the ambient turbulent boundary layer. Wall-shear reductions are also evident at the trailing interface of the spot, but the effect is not as prominent as in all other regions of the flow. In terms of the spatially-averaged wall-shear reduction within the leading and trailing interfaces of the spot, the magnitude is comparable to the average wall-shear reduction in the turbulent boundary layer.

Just upstream of the manipulator blade, i.e., at  $(x-x_m)/L = -1.38$ , the manipulated wall-shear levels of the turbulent boundary layer and the turbulent spot are approximately 20% lower than the undisturbed levels. Near the trailing edge of the manipulator blade, the wall-shear levels nearly recover to the unmanipulated levels. Such behavior is similar to the near-manipulator behavior of the turbulent spot propagating in an ambient laminar boundary layer.

## Chapter 5

### **EFFECTS OF THREE-DIMENSIONAL MANIPULATOR ELEMENTS**

#### **5.1. Motivation for Use of a Three-Dimensional Device**

The possibility was explored of using a device whose drag is comparable to the drag of the tandem manipulator, but which might produce a more dramatic effect on the wall shear. Since three-dimensionality is an inherent feature of turbulent flow, it was conjectured that a three-dimensional device may be better suited to manipulate the large eddies. Although the investigation addresses the effects of the device on the fully turbulent boundary layer as well as on the turbulent spot, the design of the device is based on known characteristics of turbulent spots.

Recent studies suggest that results obtained from ensemble-averaged measurements inadequately describe the structure of a typical individual spot [e.g., Perry et al. (1981), Gad-el-hak et al. (1981), Wygnanski (1981), Itsweire and van Atta (1984)]. Individual spots may be comprised of numerous eddies that appear on a smaller scale than that of the rather large vortical motions identified in earlier studies by Wygnanski et al. (1976) and Cantwell et al. (1978). However, as concerns the design of the present three-dimensional manipulator, the turbulent spot is modelled by its ensemble-averaged structure.

The study by Coles and Barker (1975) and the detailed investigation by Wygnanski et al. (1976) suggest that one salient feature of the ensemble-averaged turbulent spot is the existence of a large, horseshoe-shaped vortex tube. In planview, the large structure is swept back at a half-angle of approximately 15–20 degrees measured from the centerline. Due to the highly swept nature of

the horseshoe vortex tube, one would expect a significant component of streamwise vorticity to exist along the off-centerline segments of the tube. The sign of the vorticity is such that induced spanwise velocities in the near-wall region are directed toward the centerline. The purpose of the present three-dimensional device is to introduce a strong streamwise component of vorticity into the flow, in contrast to the spanwise component of vorticity introduced by two-dimensional manipulator blades.

The three-dimensional device consists of a set of wall-anchored, vertical fins aligned with the free-stream. The function of the fins is to shed tip vortices during the passage of a turbulent spot, as shown pictorially in Figure 5.1. The horseshoe vortex is a crude model for the large-scale structure of the turbulent spot and, therefore, a crude model based on high aspect-ratio wing theory is employed for the predicted behavior of the fins in the presence of spot-induced spanwise velocities. Although the flow is nonsteady, each fin is treated as a flat plate of finite span subjected to a steady angle of attack during the passage of the horseshoe vortex. If the height of the fins lies below the center of the vortex tube, induced spanwise velocities are directed toward the plane of symmetry of the spot, and the sense of rotation of the tip vortices from the fins opposes the sense of rotation of the horseshoe vortex. That is, spanwise velocities induced by the tip vortices oppose the spot-induced spanwise velocities. (Tip vortices that reinforce the spot-induced spanwise velocities could be introduced by placing the whole of the fins *above* the center of the horseshoe vortex.)

Based on this simplified model of the fin behavior, estimates can be made of the required chord length and spanwise spacing of the fins to ensure that the fin-induced spanwise velocities,  $w_f$ , are comparable to the velocities,  $w_s$ , induced by the horseshoe vortex. The characteristic mean streamwise velocity,  $U$ , is of order  $U_\infty$  and the characteristic length is assumed to be of order  $h$ , the distance



between the wall and the horseshoe vortex. At the streamwise position of the bound vortex of a fin, the Biot-Savart law predicts that a semi-infinite tip vortex will induce a 'downwash' velocity,

$$|w| = \frac{\Gamma}{4\pi h}$$

at a distance  $h$  from the core of the tip vortex. Including the effect of the tip vortex shed from the mirrored-imaged fin, the characteristic spanwise velocity induced by a single fin becomes,

$$|w_f| \sim \frac{\Gamma_f}{2\pi h}$$

The circulation around the fin,  $\Gamma_f$ , is related to relevant parameters through the lift force developed by a flat plate,

$$L_f = \rho U \Gamma_f = (2\pi\alpha)\left(\frac{1}{2}\rho U^2\right)c$$

where  $\alpha \doteq \frac{w_s}{U}$  is the spot-induced angle of attack, and  $c$  is the chord of the fin.

If  $h$  is assumed to be approximately equal to the maximum half-height of the turbulent spot,  $\delta_m/2$ , then

$$\left| \frac{w_f}{w_s} \right| \sim \frac{c}{\delta_m}$$

Therefore, if one chooses  $c = O(\delta_m)$ , the tip vortices of the fins will induce velocities  $w_f = O(w_s)$  at the characteristic distance  $h = O\left(\frac{\delta_m}{2}\right)$  from the tip

vortex. To provide such induced velocities across the entire span, the fin-to-fin spacing,  $s$ , should be  $O(\delta_m)$ .

## 5.2. Effects of the Device on Turbulent Spots

Two configurations of vertical fins were investigated: (1) a long-chord manipulator,  $c = 2.5$  cm,  $h = 0.45$  cm,  $s = 0.9$  cm, and (2) a short-chord manipulator,  $c = 1.0$  cm,  $h = 0.50$  cm,  $s = 1.0$  cm. The estimated height of the spots at the manipulator station was 0.8 cm, corresponding to the thickness attained by a spot growing at the rate of a fully turbulent boundary layer with origin located near the leading edge of the flat-plate model. Although different forcing levels were used in the course of the experiments, the virtual origins were always located between the leading edge of the flat-plate model and the trailing edge of the manipulators,  $x_m = 42.5$  cm.

Each fin was attached to a 0.13-mm thick, 1.0-cm wide brass base. The base was held in tension by the traversable, bow-shaped manipulator support, thus allowing manipulated turbulent spots to be compared with unmanipulated turbulent spots without having to change the operating condition of the HSWT facility during the experiments. Unmanipulated spots are defined as those spots forced when the base of the fins lies 4.2 cm above the flat-plate model, the highest position to which the base could be traversed. No changes in spot behavior were observed until the distance between the base of the fins and the flat-plate model was less than one centimeter. In the design configuration, however, the base of the fins rested on the surface of the flat-plate model. To ensure intimate contact between the base and the surface of the flat-plate model, a very thin film of silicon grease was applied to both surfaces prior to each run. Bench experiments indicated that the overall film thickness was less than 0.02 mm.

One difficulty in performing such an experiment is the adverse effect of the nonsteady wakes produced by the fins on the laminar boundary layer. Although a detailed study of the wake behavior was not undertaken, it was determined that laminar flow regions exist between the wakes for at least 10 fin-spacings downstream of the device. Furthermore, the flow exhibits fully turbulent behavior across the entire span at a station located 25 fin-spacings downstream of the device. Some measurements were made directly in line with the wakes, but the wall-shear sensors were generally positioned between neighboring wakes.

Attempts to alter the wall shear of turbulent spots yielded only slight changes. Shown in Figures 5.2 and 5.3 are ensemble-averaged wall-shear time histories recorded at two spanwise positions,  $z/b \approx 0.0$  and  $0.8$ , respectively, located approximately  $10\delta_m$  downstream of the long-chord manipulator. The dotted curves depict the wall-shear behavior of the undisturbed turbulent spot, i.e.,  $h = 4.2$  cm, and the solid curves represent the behavior of the manipulated spot, i.e.,  $h = 0.0$  cm. Both sensors were positioned between the wakes of the vertical fins.

A slight decrease in the extent of the turbulent region is observed at both spanwise positions. Overall, the wall shear along the centerline experiences a small reduction while that at the off-centerline position increases slightly. A delay in the arrival of the leading and trailing interfaces also occurs at both spanwise positions.

If the manipulators are to behave as predicted, the effects should be more pronounced along off-centerline segments of the spot than along its centerline. The experiment was repeated using slightly smaller spots, thus increasing  $z/b$  to  $\approx 0.9$  while keeping the sensor positions fixed. As shown in Figures 5.4, a more dramatic effect is realized near the extremity of the spot where the wall-shear level and the streamwise extent are reduced.

This behavior was also observed in an earlier experiment in which the short-chord manipulator was employed. As  $z/b \rightarrow 1$ , the wall shear and the stream-wise extent of the spot are dramatically reduced, as shown in Figure 5.5. (The off-centerline sensor was again positioned between the wakes of two vertical fins.)

The wall-shear behavior *directly* downstream of a short-chord fin is shown in Figure 5.6. In this experiment, the center-most fin was aligned with the center-line of the flat-plate model, which also corresponds to the plane of symmetry of the turbulent spot. The wake of the fin is observed to cause an increase in the mean wall shear of both the ambient boundary layer and certain regions of the turbulent spot.

Therefore, the most significant effect of the vertical-fin manipulator on the spot appears to be the inhibition of its spanwise growth. Large reductions in the wall shear and in the streamwise extent of the spot are observed only near the spanwise extremity,  $z/b \approx 0.9$ . At this spanwise position the magnitude of the mean wall-shear reduction,  $\approx 30-40\%$ , is realized for both long- and short-chord manipulators. However, these effects do not appear to be significant in the context of the present investigation since only modest wall-shear reductions are evident for values of  $z/b$  less than 0.9.

### 5.3. Effects on a Turbulent Boundary Layer

To ascertain the average effect of the vertical-fin manipulator on randomly occurring large-scale structures, and to substantiate its relatively small effect on turbulent spots, the vertical-fin device was placed in a fully turbulent boundary layer. Although the primary focus of the experiment was to investigate the effectiveness of the vertical fins in reducing the wall shear, the fins and base to which they are attached could be traversed to any height in the range  $0 < h <$

4.2 cm. When the base is positioned above the wall, the device can be considered to be a hybrid manipulator comprised of a conventional two-dimensional blade (the base) and vertical fins. Results are therefore presented using the height of the base above the wall,  $h$ , as a parameter. The vertical-fin results therefore represent a special case of the hybrid manipulator in which  $h \rightarrow 0$ .

Shown in Figure 5.7 are the wall-shear reductions at two downstream stations for various manipulator heights. Comparisons are made with the effects of the tandem configuration, whose total wetted area is equal to that of the hybrid device (fins plus base). Although direct measurements of the drag of the device were not made, it appears that for  $h > 0$  the hybrid device is as effective in reducing the wall shear as is the tandem configuration.

Shown in Figure 5.8 is the wall-shear distribution downstream of the device for the case  $h = 0$ . The dimension of the fins in the direction normal to the wall is  $0.61\delta_m$ . Comparisons are therefore made with the effects of a tandem manipulator positioned  $\approx 0.50\delta_m$  and  $0.75\delta_m$  from the wall. It is noted that the total wetted area of the vertical-fin device is effectively one-half that of the tandem device, since the base of the fins is on the wall. Thus, if the wall-shear reductions due to the fins were comparable to the reductions due to the tandem device, the effectiveness of the vertical-fin device would be rated higher than that of the tandem configuration. However, the reductions due to the vertical-fin device are much smaller than the reductions due to the tandem device (and of the hybrid device as well). Furthermore, the effects do not persist as far downstream. The quick recovery of the wall shear is reminiscent of the behavior exhibited by other near-wall devices (e.g., sudden change in wall roughness or moderate blowing/suction) as opposed to outer-scale devices whose effects are observed to persist for greater downstream distances.

Therefore, as in the case of the turbulent spot, the effects of the vertical-fin device on the turbulent boundary layer are modest. The device, as designed in the present investigation, does not appear to be a suitable alternative to the tandem configuration.

## Chapter 6

### DISCUSSION AND CONCLUSIONS

Experiments were performed to study the effects of various large-eddy manipulators on turbulent wall shear, and to better understand the mechanisms involved. The effects of a tandem-blade manipulator on the wall shear in a turbulent boundary layer were investigated in an initial set of experiments. In an effort to explain the observed effects in terms of organized turbulent structure, the turbulent spot was employed as a prototype large-scale eddy. The possible effectiveness of a three-dimensional manipulator configuration was also explored. Wall-shear reductions due to the device were investigated for both the fully turbulent boundary layer and the turbulent spot.

#### 6.1. Manipulated Turbulent Boundary Layer

The present measurements of mean wall-shear distributions downstream of tandem manipulators show good agreement with skin-friction balance measurements made independently by Mumford and Savill (1984) and by Lemay et al. (1985), as shown in Figures 3.4 through 3.6. To obtain an upper bound for the possible net drag reduction, it is assumed that the drag of the device is given by its laminar value. In computing the laminar drag, it is assumed: (1) that the drag of the second blade is one-half that of the first blade due to shielding effects; (2) that the appropriate velocity for the dynamic pressure computation is the local mean velocity at the manipulator height,  $h \approx \delta_m/2$ ; and (3) that the chord of each manipulator blade is equal to the local boundary-layer thickness,  $\delta_m$ . Generous provision is also made for the possibility of wall-shear reductions in the region between the first and second manipulator blades, in that the

average manipulated wall shear is assumed to be 20% below its undisturbed value, a reduction comparable to the maximum value attained downstream of the second manipulator blade.

Based on such estimates of device drag and on the direct wall-shear measurements made downstream of the second manipulator blade, it is concluded that small net drag reductions ( $\sim 5\%$ ) may be possible over large downstream distances ( $\gtrsim 100 \delta_m$ ). This assessment is in general agreement with the results obtained in the NASA Langley investigations, e.g., Anders and Watson (1985), in which the two-dimensional momentum-balance technique was employed. Unfortunately, such small net drag reductions are comparable to the magnitude of experimental error.

Such results are not consistent with the results of Plesniak and Nagib (1985) who report net drag reductions as large as 20% under comparable conditions. Plesniak and Nagib argue that discrepancies in the magnitude of reported net drag reductions may be attributed to differences in the drag of the device. However, differences in the magnitude of the wall-shear reduction, particularly at large downstream distances ( $\sim 100\delta_m$ ), seem to be the dominant contributing factor to the net drag discrepancies. Direct wall-shear measurements indicate that peak reductions of 20-40% are attainable, depending on the manipulator height. Such peak values were inferred by Plesniak and Nagib, but the direct measurements of the present study indicate that the reductions do not persist for significant streamwise distances. Therefore, for streamwise distances greater than (say)  $50\delta_m$ , experiments involving direct wall-shear measurements in manipulated boundary layers show much smaller values of the average shearing *force* reduction than those attained by Plesniak and Nagib.

A more important conclusion can be reached regarding the mechanism responsible for the observed wall-shear reductions. By comparing the



momentum deficit introduced by the manipulator,  $\theta_m$ , to a characteristic change in the momentum thickness of the undisturbed boundary layer,  $\Delta\theta$ , it is established that the tandem manipulator is **not** a low-drag device. A low-drag device is presently defined as one for which  $\theta_m \ll \Delta\theta$ , where the momentum deficit in the wake of the manipulator is representative of the drag imposed by the device on the fluid. The laminar value is assumed to represent a lower bound for the drag of the device. The characteristic change in the momentum thickness of the undisturbed boundary layer is that which occurs over the streamwise distance,  $\Delta x$ , in which the wake of the manipulator is incorporated into the boundary layer. This characteristic change in the momentum thickness is representative of the natural ability of the friction at the wall to decelerate fluid over the streamwise distance in which the wake is mixed with the boundary layer fluid.

It was shown in Section 3.3 that a lower bound for the drag parameter,  $\theta_m/\Delta\theta$ , is

$$\frac{\theta_m}{\Delta\theta} \approx \frac{5.3}{C_f \frac{\Delta x}{\delta_m}} \left[ \frac{\frac{L}{\delta_m}}{\text{Re}_\theta \frac{\delta_m}{\theta_m}} \right]^{\frac{1}{2}}$$

For turbulent flow over a flat plate, unmanipulated values of the skin-friction coefficient,  $C_f$ , and the ratio of boundary-layer thicknesses,  $\delta_m/\theta_m$ , may be computed from accepted correlations, given the momentum-thickness Reynolds number,  $\text{Re}_\theta$ . For the Reynolds number range  $1000 < \text{Re}_\theta < 6000$ , the corresponding ranges for  $C_f$  and  $\delta_m/\theta_m$  are approximately 0.0029–0.0042 and 8.7–9.6, respectively.

From the mean-velocity profiles of Corke (1981) and Lemay et al. (1985), a distinct wake profile is observed to be embedded in the mean velocity profile immediately downstream of the manipulator, and to persist for  $\sim 20-40\delta_m$  downstream. Assuming that a representative value for  $\Delta x$  is  $30\delta_m$ , a lower bound for the drag parameter  $\theta_m/\Delta\theta$  varies from  $\sim 0.50$  at  $Re_\theta = 1000$  to  $\sim 0.25$  at  $Re_\theta = 6000$ . Therefore, the drag of the tandem manipulator is **not** small compared to a characteristic (unmanipulated) drag force on the wall.

It is conjectured that the distinct minimum that occurs in the manipulated wall-shear distributions is intimately connected to the characteristic streamwise distance over which the wake is incorporated into the boundary layer. Furthermore, the distance over which the low-momentum fluid in the wake is fully incorporated into the boundary layer is expected to depend on the height of the manipulator. One would expect the mixing of the low-momentum fluid to take place over shorter downstream distances as the device is moved closer to the wall, due to the smaller time scales and velocity scales at the lower heights. For low manipulator heights, the mixing of the low-momentum fluid occurs over a relatively small streamwise extent and, consequently, the wall-shear reductions are more dramatic than the reductions that occur for greater manipulator heights. This conjecture is consistent with the observation that the minimum deepens and moves closer to the manipulator as the blades are traversed closer to the wall. It is also noted that over a wide range of manipulator heights,  $0.30-0.75\delta_m$ , the average wall-shear reduction at large downstream distances does not appear to be particularly sensitive to the height of the blades.

The conclusion reached is that the momentum deficit introduced by the wake is an important contributor to the observed wall-shear reductions, rather than that the ability of turbulent mixing in the boundary layer to decelerate fluid is dramatically impaired. It is not suggested that the ability of the boundary layer

to decelerate fluid is unaffected, or that net drag reductions are not possible. In fact, one would expect reductions in the Reynolds stresses and in the turbulence production near the wall due to the reduction in the shear stress at the wall. However, it is suggested that a significant contribution to such reductions arises from the transport and mixing of low-momentum fluid from the wake of the manipulator. Furthermore, it is suggested that the possible effects of the device on turbulent structure are clouded by the presence (and importance) of the wake.

## **6.2. Manipulated Turbulent Spots**

In an attempt to better understand the mechanisms responsible for the observed wall-shear reductions, the turbulent spot was employed as a prototype large-scale eddy. The investigation focused on the ensemble-averaged behavior of turbulent spots, with and without manipulation. As shown in Figure 4.6, the most dramatic wall-shear reduction occurs near the leading edge of the spot. The trailing edge of the spot is not noticeably influenced by the manipulator.

The structural model of the turbulent spot presented by Cantwell et al. (1978) is used as a basis for interpreting the presently observed effects on the turbulent spot. The ensemble-averaged structure was deduced from the assumption of conical similarity for their ensemble-averaged velocity measurements. Shown in Figure 4.10 is a sketch of the particle trajectories in the ensemble-averaged turbulent spot. Also included is a table of the relative rates of entrainment across various boundaries of the spot, as deduced by Cantwell et al.

The position of the large vortex structure and the entrainment of ambient fluid into the spot are of particular interest. As this high-momentum ambient fluid is entrained into the spot, it is mixed with and decelerated by the turbulent

fluid inside the spot. Within the boundary-layer approximation, the deceleration of the entrained fluid must eventually be manifested in the shearing force at the wall. From the table in Figure 4.10, it is observed that approximately 80% of the total entrainment in the spot occurs along the upstream-facing boundary (segment b-c-d). Of this fluid, approximately two-thirds is entrained along the upper portion of this boundary (segment c-d) and is subsequently incorporated into the outer region of the spot, i.e., the region occupied by the large vortex structure.

The manipulator and its associated wake were located in the outer region of the spot, i.e., above the separatrix defined by the solid line between points c and e in Figure 4.10. In the presence of the manipulator, the momentum of the 'free-stream' wake fluid that is eventually entrained along the upper, rear boundary of the spot (segment c-d) is initially lower than that of the fluid entrained in the absence of the manipulator. Therefore, one would expect the deceleration of the entrained fluid, and thus the average wall shear, to be lower in the presence of the manipulators. Furthermore, the tendency of the large vortical structure to transport entrained fluid closer to the wall, where turbulent fluctuations are particularly violent, suggests that wall-shear reductions should be most prominent in the immediate vicinity of the vortex. The large decrease in wall shear presently observed near the leading edge of manipulated spots supports this conjecture.

A similar argument can be made for the absence of any wall shear reductions near the trailing interface of the spot. Since the manipulator was always positioned in the outer region of the spot, entrainment along the lower, rear boundary (segment b-c) was little affected by the wake of the manipulators. It is noted that more than 20% of the total entrainment occurs along the short segment b-c, and that the deceleration occurs within a relatively small region located near

the trailing interface. It appears that the maximum in the wall shear observed near the trailing interface, with or without manipulation, is associated with the rapid deceleration of fluid entrained along the segment b-c.

Attempts to observe the effects of the manipulator on the spot at greater downstream distances ( $> 12\delta_m$ ), or for lower manipulator heights ( $< 0.6\delta_m$ ), were hampered by premature transition of the otherwise laminar ambient boundary layer due to the wake of the manipulator. Under either condition, it is conjectured that wall-shear reductions would be evident in regions closer to the trailing interface of the spot due to the entrainment of the wake along segments of the upstream-facing boundary that lie closer, in the conical similarity coordinates, to the trailing interface of the spot.

Despite the adverse effect of the manipulator wake on the ambient laminar flow, the manipulator blades were placed closer to the wall ( $\sim 0.5\delta_m$ ), as in Figure 4.8. It is observed that the wall-shear reduction in the leading-interface region of the spot is slightly enhanced compared to the effect at greater manipulator heights. Furthermore, wall-shear reductions are also apparent toward the trailing interface, as expected. Since the entrainment of the oncoming ambient boundary layer accounts for only about 14 percent of the total fluid entrained by the spot, the large mean and fluctuating shear levels caused by transition in the ambient flow do not appreciably affect the mean shear levels within the spot.

Exploratory measurements were also made in the neighborhood of the manipulator blades. It was conjectured that any circulation developed by the blade as the vortex structure approaches may alter the position of the vortex within the spot. However, the large wall-shear reductions observed near the leading edge of the spot after it travels downstream of the manipulator are not apparent in the neighborhood of the blades. Instead, the blades act much like the upper

wall of a channel. The wall shear first decreases almost uniformly across the entire extent of the spot as it approaches the leading edge of the blade. This behavior is consistent with the observation in a turbulent boundary layer by Mumford and Savill (1984) that as the flow approaches the blades it moves outward and the boundary layer thickens by approximately one-third. Their observation was based on flow visualization. The deceleration is apparently followed by an acceleration directly under the blades, as suggested by the rise in wall shear as the spot approaches the trailing edge of the blade. This general behavior occurs for the laminar boundary layer, the turbulent spot, and the turbulent boundary layer.

It is not clear from the present measurements that transport properties of the spot or of the turbulent boundary layer are inhibited. The numerical study by Kinney et al. (1985) and the recent analytical work by Dowling (1985) suggest that an interaction does indeed occur between the large eddies and the vorticity shed by the manipulator due to a nonsteady circulation around the blades. Both investigations indicate that, for a two-dimensional flow, the sign of the vorticity shed from the blades during the passage of large eddies (concentrations of vorticity) opposes the sense of rotation of the eddies.

Attempts were also made to follow and manipulate individual turbulent spots propagating in a fully turbulent boundary layer. It was first established that the unmanipulated spot can be followed for large downstream distances, i.e., approximately  $75\delta_m$  from the heated-element. [A similar conclusion was reached by Haritonidis et al. (1977)]. The wall-shear traces shown in Figure 4.11 were obtained near the last manipulator blade and  $16\delta_m$  downstream of the blade. At the most downstream station, the wall-shear reduction near the leading interface of the spot is enhanced compared to the mean reduction in the ambient turbulent boundary layer. A reduction also occurs near the trailing

interface of the spot, although the effect is smaller than that in the ambient turbulent flow. The average wall-shear reduction in the manipulated spot was found to be comparable to the reduction in the surrounding turbulent boundary layer.

The wall-shear reduction presently observed near the trailing interface of the spot when it propagates in a turbulent boundary layer is not apparent when the spot propagates in a laminar boundary layer (at a comparable distance, say,  $10-15\delta_m$  from the manipulator). It is conjectured that the reduction is primarily due to the presence of eddies near the trailing interface of the spot that are not present when the ambient flow is laminar. Such eddies would enhance the transport of the low-momentum fluid in the wake to positions closer to the wall.

### **6.3. Effects of a Vertical-Fin Manipulator**

The possibility of affecting the behavior of the turbulent spot using a three-dimensional manipulator configuration was also explored. The spot is modelled as a highly swept, horseshoe-shaped vortex tube that induces a relatively strong spanwise component of velocity. Near the wall this spanwise component of velocity is directed toward the centerline of the spot. In an attempt to attenuate the streamwise component of vorticity along the vortex tube, a set of wall-anchored, streamwise-oriented, vertical fins was placed across the span of the flat-plate model. As illustrated in Figure 5.1, the purpose of the fins is to generate streamwise-oriented tip vortices when the horseshoe-shaped vortex is in the vicinity of the device. If the upper edges of the fins lie below the mean position of the vortex tube, they are subjected to an angle-of-attack such that the 'lift' force is directed toward the centerline of the spot. The corresponding sense of rotation of the tip vortices shed from the uppermost edge of the fins is such as

to oppose the streamwise component of vorticity in the vortex tube.

A crude model based on high aspect-ratio wing theory is used to estimate the required chord length,  $c$ , and the fin-to-fin spacing,  $s$ , of the device. The appropriate height of the fins,  $h$ , is assumed to be approximately  $\delta_m/2$ , where  $\delta_m$  is the local maximum thickness of the spot. The model predicts that if  $c = O(\delta_m)$ , the tip vortices will induce spanwise velocities  $w_f = O(w_s)$  at characteristic distances  $h$  from the tip vortices, where  $w_s$  is the spanwise component of velocity induced by the horseshoe vortex. To provide such induced velocities across the entire span of the spot, the fin-to-fin spacing,  $s$ , should be of the order of  $\delta_m$ .

As illustrated in Figures 5.4 and 5.5, the most dramatic effect of the device on the spot occurs near the spanwise extremities where both the magnitude of the wall shear and the streamwise extent of the spot are reduced. Such dramatic reductions are not observed at positions closer to the centerline. Therefore, it appears that the dominant effect of the vertical-fin configuration is a retardation of the spanwise growth of the spot. However, it is emphasized that the effects do not appear to be significant in the context of the present investigation, since only modest wall-shear reductions are evident for values of  $z/b$  less than 0.9.

Effects of the vertical-fin device on fully turbulent mean wall shear were also investigated and compared with the effects due to a tandem manipulator. The total wetted area of the vertical-fin device, per unit span, was one-half that of the tandem device. Thus, one would consider the vertical-fin device to be more effective than the tandem device if the wall-shear reductions due to the two devices were comparable. However, as shown in Figure 5.8 the peak reductions in the wall shear are less than those due to the tandem configuration, and the wall shear exhibits a quicker recovery to its undisturbed level. Therefore, the



effectiveness of the vertical-fin device does not represent a significant improvement on the effectiveness of the tandem manipulator.

It is conjectured that the lack of any significant effect may be related to the fin height used. According to the vortex-tube model of the spot presently used, if the fin height is appreciably greater than the height of the vortex tube, spanwise velocity components of both signs would exist along the leading edge of each fin. Consequently, the circulation developed around each fin would be reduced. Furthermore, the model used for the spot is admittedly crude. A better understanding of the three-dimensional structure of the spot [obtained, for example, by extending the centerline description provided by Cantwell et al. (1978)] would be useful.

## Appendix A

### MANUFACTURE OF WALL-SHEAR SENSOR ARRAYS

A new technique for manufacturing arrays of flush-mounted, thin-film wall-shear sensors was developed for use in the present experiments. The motivation for the development stemmed from the inherent immobility of flush-mounted wall-shear sensors, as opposed to such transducers as velocity hot-wires that can be easily traversed from one location to another. The use of sensor arrays provides the experimenter with the flexibility to select desirable measuring locations. Furthermore, the present technique permits the experimenter to design convenient sensor-array patterns and sensor-to-sensor spacings.

Shown in Figure A.1 is a schematic of a single wall-shear sensor and its associated substrate, protective coating, and electrical leads. The two circular pads shown in the top view provide low-resistance electrical connections between the conductive epoxy-filled holes and the 0.10 x 0.81 mm sensor.

The process developed to manufacture arrays of wall-shear sensors is outlined below:

- [1] Design of the sensor pattern and spacings.
- [2] Substrate preparation, which includes the provision of front-to-back electrical connections through conductive epoxy-filled holes.
- [3] Vacuum deposition of a uniform metal (tin) film over the entire active surface of the substrate.
- [4] Positive photoresist application, exposure, and development.

[5] Chemical etching of undesired metal.

[6] Photoresist removal.

[7] Deposition of Parylene C, a thin protective film.

Details of each of the above steps are given below.

### **Step 1: Sensor Design**

A large master drawing of the sensor pattern was made on a 1:4 scale. A true-size 'positive' of the sensor array, used as a mask when exposing the photoresist in Step 4, was produced from a photographic reduction of the master drawing.

The procedure used to produce the master was similar to that used in the design of simple printed-circuit (PC) boards. Using standard drafting equipment, the centers of all circular 'conductions' pads were first marked on vellum. Narrow strips of black artists tape, representing the sensors themselves, were then placed between each pair of center marks. Finally, commercially available, adhesive-backed, black 'doughnuts', representing the circular conduction pads, were located at each of the center marks. If necessary, India ink was used to touch-up any unblackened areas within the dumbbell-shaped contours.

Shown in Figure A.2 is a typical, true-size pattern of wall-shear sensors produced from a photographic reduction of the master. Each sensor in the particular pattern shown has a 'twin'. This redundancy was included in the design in the event that any sensors were damaged during the manufacturing process or in subsequent handling and use.

## **Step 2: Substrate Preparation**

Standard 1/8-inch thick, glass-reinforced epoxy-resin PC boards were selected for the substrate material. The primary factors considered in the selection were the machinability and durability of PC boards, compared to (say) quartz which is used as the substrate for sensors manufactured commercially.

Substrate preparation began by first cutting a stock PC board to a diameter slightly larger than the diameter of the circular cutouts in the flat-plate model. A thin layer of fiberglass resin was then applied to the active side of the board. This step was taken to avoid exposing the relatively rough glass strands while sanding and polishing the active surface. The board was then mounted on a milling machine, and the pairs of 0.80-mm diameter holes were drilled.

The holes were filled with Emerson & Cuming ECOBOND 83C silver-filled conductive epoxy. Extrusion of the pasty epoxy through the holes using a small block of lucite was found to work well. Prior to the epoxy cure, solid copper pins were inserted into the holes from the back side of the board. After the cure, electrical leads were soldered to the copper pins.

The substrate was then epoxied to a circular, thin-walled, stainless-steel insert that could be mounted into the circular cutouts of the flat-plate model. Excess material around the circumference of the PC board was trimmed on a lathe until its diameter matched the outside diameter of the stainless steel insert.

The active surface of the substrate was then prepared for vacuum deposition. Using a machinist's surface plate and sandpaper, the surface was leveled and smoothed. Fiberglass polishing compound was subsequently used to provide a mirror-like surface finish. The substrate was thoroughly cleaned with methanol immediately prior to the metal-film vacuum deposition.

### **Step 3: Metal-Film Vacuum Deposition**

A vacuum system manufactured by Veeco Instruments, Inc., model VE-775, was used to vacuum deposit a thin film of tin over the entire surface of the sensor array. The substrate was placed 36 cm from the source, a cup-shaped metal 'boat' that held the granular tin. Air within the bell jar was pumped out using a combination of mechanical and diffusion pumps. After the pressure was reduced to a value below  $10^{-5}$   $\mu\text{m Hg}$ , the tin was deposited by ohmically heating the tin boat. The film thickness was monitored by placing a crystal oscillator near the surface of the substrate. A film thickness of approximately 3000 Å, as measured by the oscillator, yielded final sensor resistances of  $\approx 5.0$  ohms. The predicted thickness necessary to achieve 5-ohm sensors is 1800 Å, assuming that the volume resistivity of tin is 11  $\mu\Omega$ -cm and that the aspect ratio of the sensors is 8:1 (0.81 x 0.10 is the design value).

### **Step 4: Photolithography**

This step *immediately* followed the tin deposition to avoid the possibility of contaminating the tin film through oxidation, exposure to Pasadena smog, etc. The purpose of this step was to provide a thin protective film over those portions of the tin that would comprise the sensors and their corresponding conduction pads. Areas not protected by the film were later chemically dissolved (see Step 5).

The following photolithographic procedure was followed:

- 1) Positive photoresist (ROK Industries PPH3135-30.5, equivalent to AZ1350J-SF) was applied with an airbrush. Three parts of photoresist were diluted with one part of photoresist thinner.

2) The unexposed photoresist film was soft-baked at  $65^{\circ}\text{C}$  for 10 minutes. A dust-cover was used over the sensor array during the bake.

3) The photographic positive produced in Step 1 was positioned on the substrate surface, and the assembly was placed in a frame that sandwiched the photographic positive between a thick lucite plate and the active surface of the substrate, thus ensuring intimate contact between the photographic film and the photoresist film.

4) The masked photoresist film was exposed to ultra-violet light ( $\approx 385$  nanometer wavelength). For incident radiation in the wavelength range 325-450 nm, the recommended exposure energy is  $\approx 80 \text{ mJ}/\text{cm}^2$  per micron of film thickness. Using a commercial UV lamp rated at  $7 \text{ mW}/\text{cm}^2$  at a distance of 30 cm, an exposure time of approximately 60 seconds was required. Using sunlight, whose irradiance within the sensitive wavelength range of the photoresist is roughly  $13 \text{ mW}/\text{cm}^2$ , an exposure time of approximately 40 seconds was required.

5) The photographic mask was removed and the photoresist was developed for 60 seconds (ROK Industries PPD-20 developer). The sensor array was then rinsed with de-ionized water and blown dry.

6) Finally, the photoresist was hard-baked at  $110^{\circ}\text{C}$  for 15-20 minutes.

#### **Step 5: Chemical Etching of Tin**

The following acid-based mixture was used to chemically remove undesired areas of the tin film (all parts are by volume):

40 parts ethylene glycol

7 parts hydrogen peroxide

3 parts hydrochloric acid

1 part nitric acid

The substrate was immersed in the etchant for a total of 2-3 minutes. Constant agitation was provided by simply moving the substrate up and down in the bath. The state of the etchable tin was examined every 15 seconds or so, and the etch was complete when only the dumbbell-shaped sensors/pads remained. Upon completion of the etch, the substrate was rinsed with de-ionized water.

#### **Step 6: Photoresist Strip**

The remaining hardened photoresist, which protected the sensors during the metal etch, was removed using a commercial stripping solution (ROK Industries PRR-001). Since the mixture contains alkaline chemicals, the stripper also served to neutralize any residual acid.

After the photoresist strip, the array was rinsed thoroughly with de-ionized water and blown dry. Residual water was removed by rinsing the substrate with a chemical drying agent (ROK Industries HMDS), and subsequently baking the assembly at 100°C for 10 minutes.

#### **Step 7: Parylene C Protective Film**

Since the sensors were designed to be used in water, it was necessary to insulate the metal films to protect them against electro-chemical degradation. Parylene C, one member of a class of polymers developed by the Union Carbide Corporation, was deposited over the entire surface of the substrate.

One unique feature of the deposition is the conformal nature of the coating. This is due to the relatively high pressure at which Parylene deposition takes place ( $\approx 0.1$  torr compared to  $10^{-5}$  torr or below for metal deposition), thus yielding a mean free path in the deposition chamber on the order of 1 mm. Other desirable characteristics include its low permeability to moisture and its high dielectric strength.

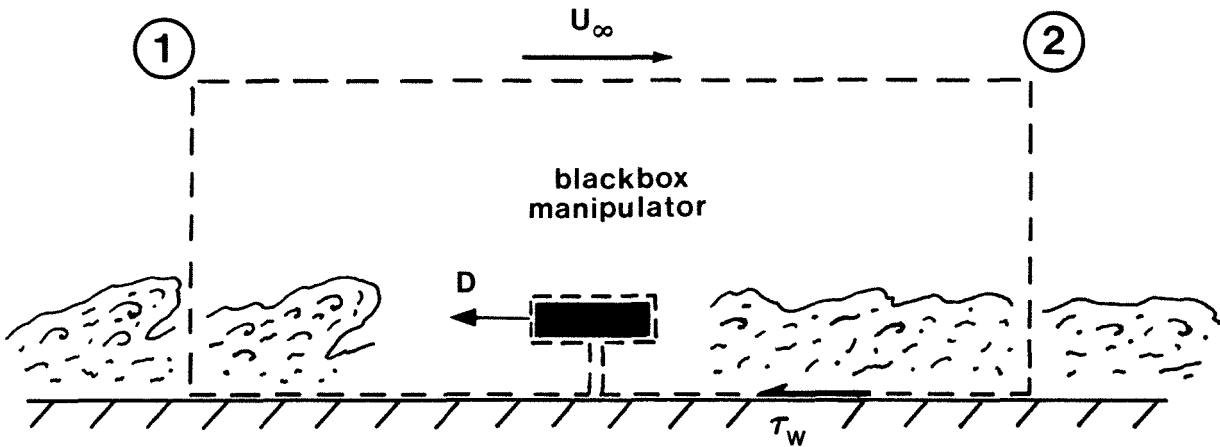
The Parylene deposition was performed by the Nova Tran Corporation, licensed by the Union Carbide Corporation. Film thicknesses of 3-5 microns were deposited on the present sensor array, and the coating was guaranteed by the manufacture to be pinhole-free.

To ensure that the Parylene coating was providing the proper insulation, a bench experiment was performed in which the sensor array and an external electrode were submersed in water. The electrode was connected to a power supply whose voltage could be set to any value in the range 0-30 volts. The pair of leads from a randomly selected sensor was connected to a 1.0 mA ohmmeter that shared a ground with the power supply of the external electrode, and the electrode voltage was slowly increased from zero volts. The existence of a flow of ions between the electrode and the sensor, which would indicate that the Parylene coating was not protecting the tin film, would be evident from a change in the resistance of the sensor. The experiment was repeated for several other randomly selected sensors.

Sensors coated with the Parylene exhibited no changes in resistance for electrode voltages as high as 30 volts, a level that was an order of magnitude higher than the voltage levels used to force spots (see Section 2.6). Sensors *not* protected with Parylene were severely damaged when the electrode voltage exceeded a value on the order of several volts. Sensor damage was indicated by a sharp increase in the resistance of the sensor and by the pitted nature of the



metal film when viewed under a microscope. The electrode voltage at which the electro-chemical action was initiated was not strongly dependent on the electrode material used (copper, stainless steel, and tin were used, independently, for the electrode material).



Control volume chosen to ensure that  $p_1 = p_2$ .

$D$  = drag of device acting on fluid.

$\tau_w$  = wall shear acting on fluid.

Net Drag Reduction if:

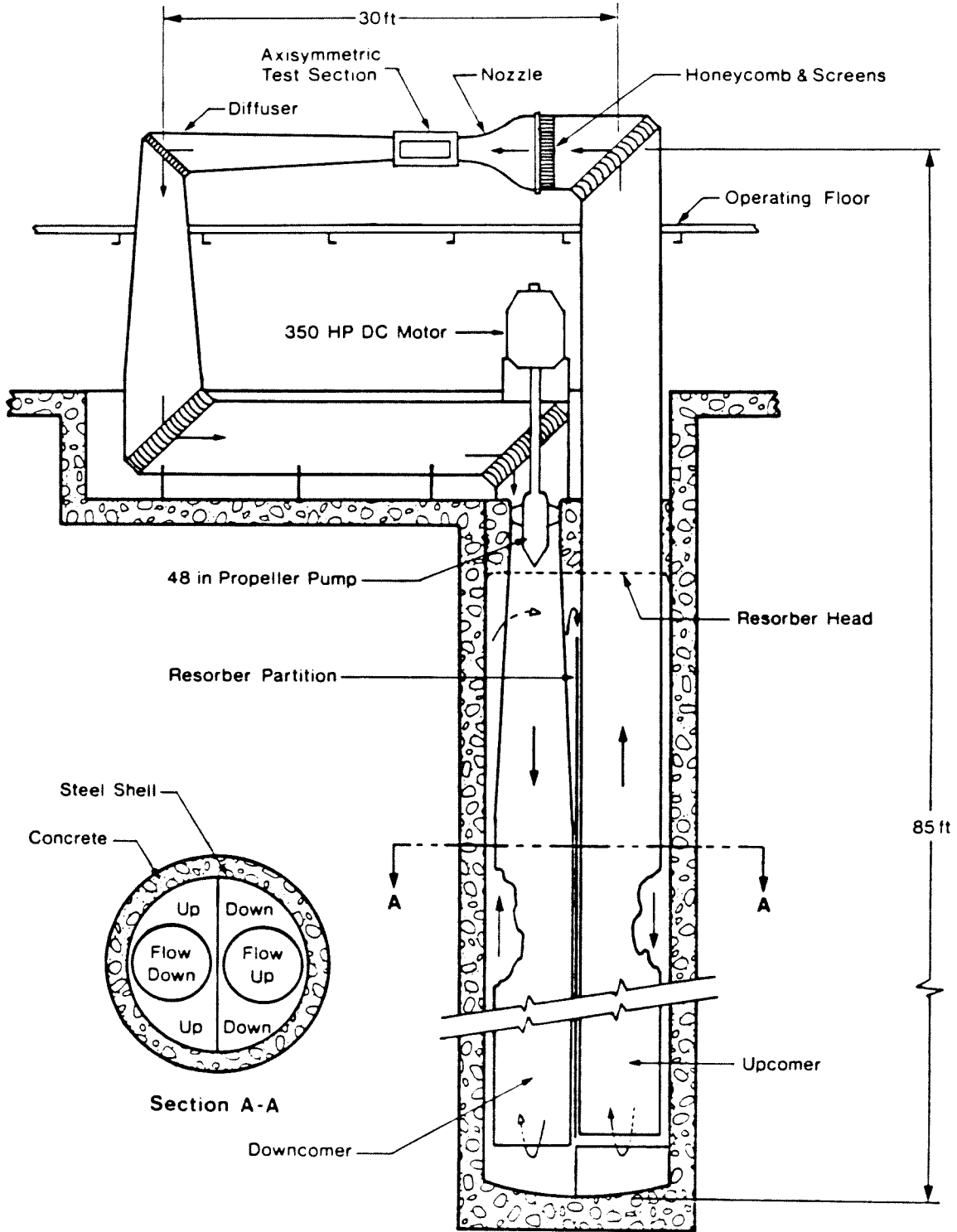
$$\left[ \int_{x_1}^{x_2} \tau_w dx + D \right]_m < \left[ \int_{x_1}^{x_2} \tau_w dx \right]_o$$

Or,

$$\left[ \theta_2 - \theta_1 \right]_m < \left[ \theta_2 - \theta_1 \right]_o$$

where  $\theta$  = local momentum thickness

**Figure 1.1** Definition and evaluation of net drag reduction



**Figure 2.1** GALCIT High-Speed Water Tunnel (HSWT)

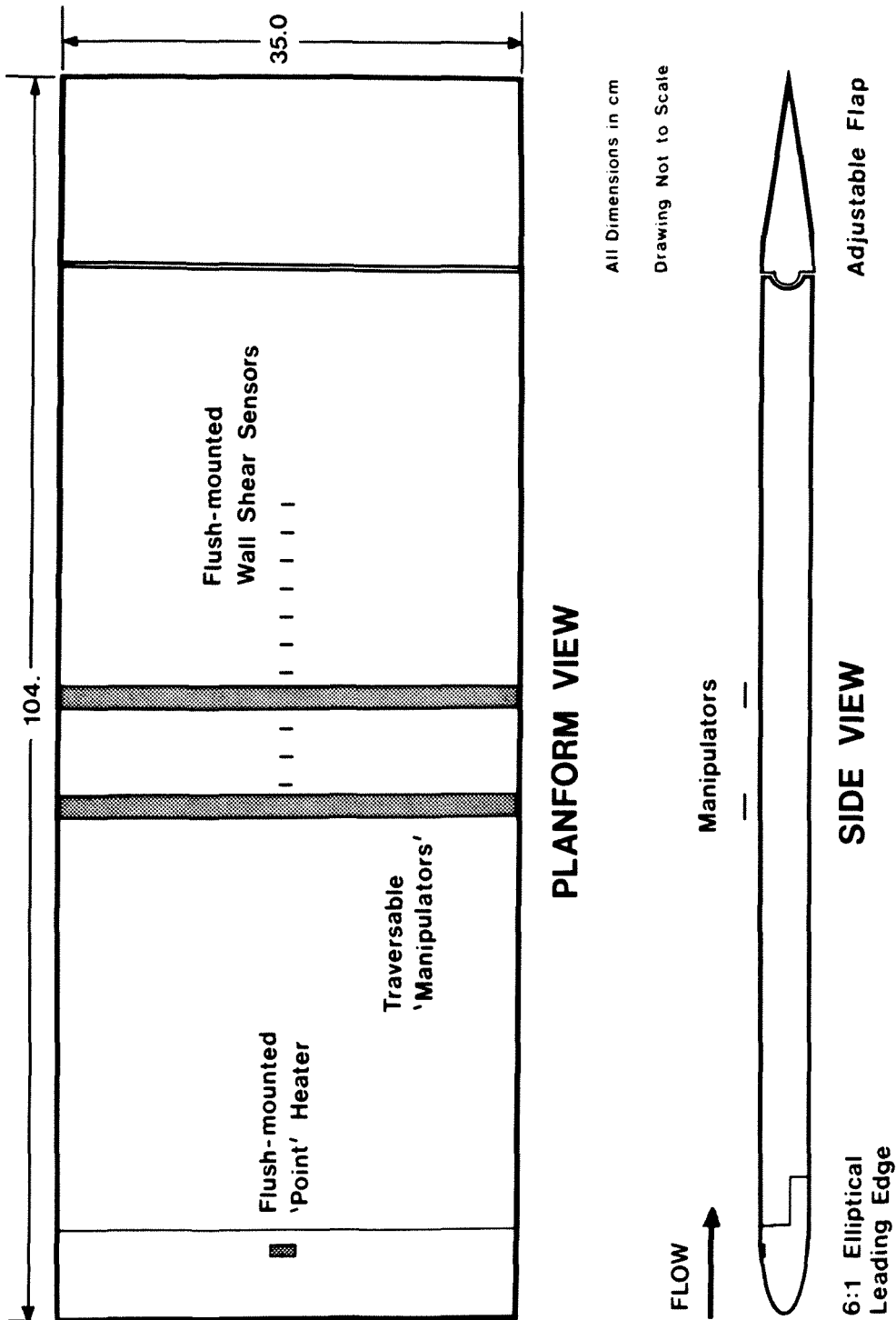
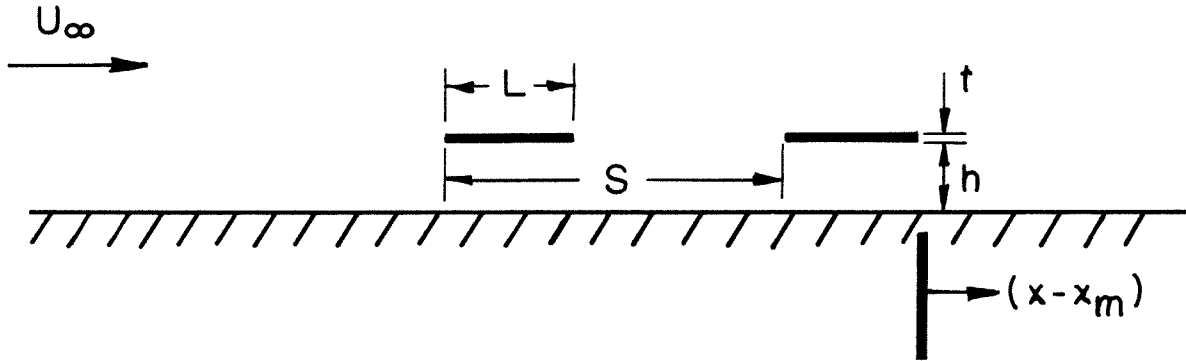


Figure 2.2 Schematic of flat-plate model



$\delta_m$  = Boundary layer thickness at  $x = x_m$   
(or maximum thickness of spot at  $x = x_m$ )

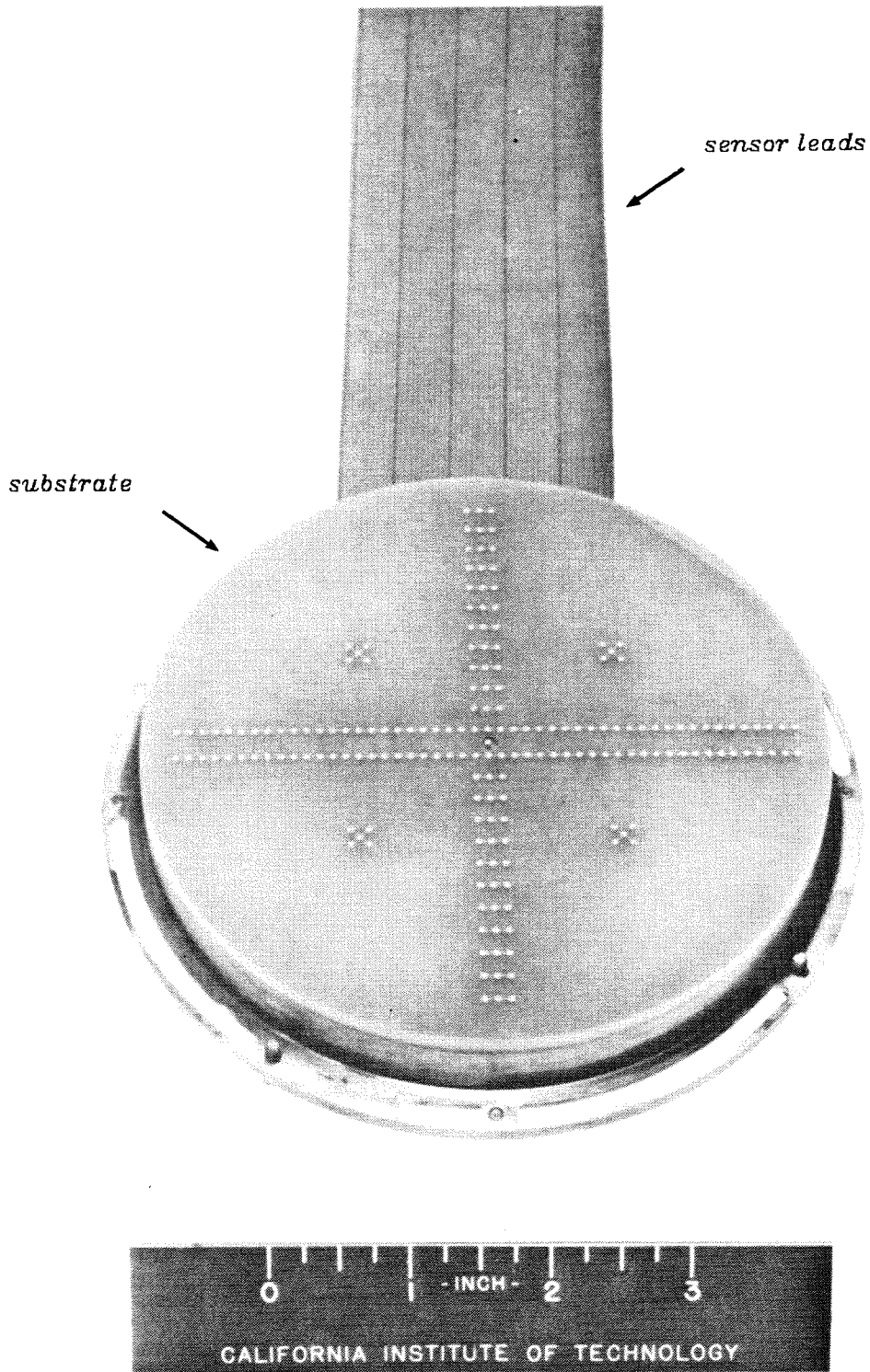
Typical Dimensions:

$$L / \delta_m = 1 - 2$$

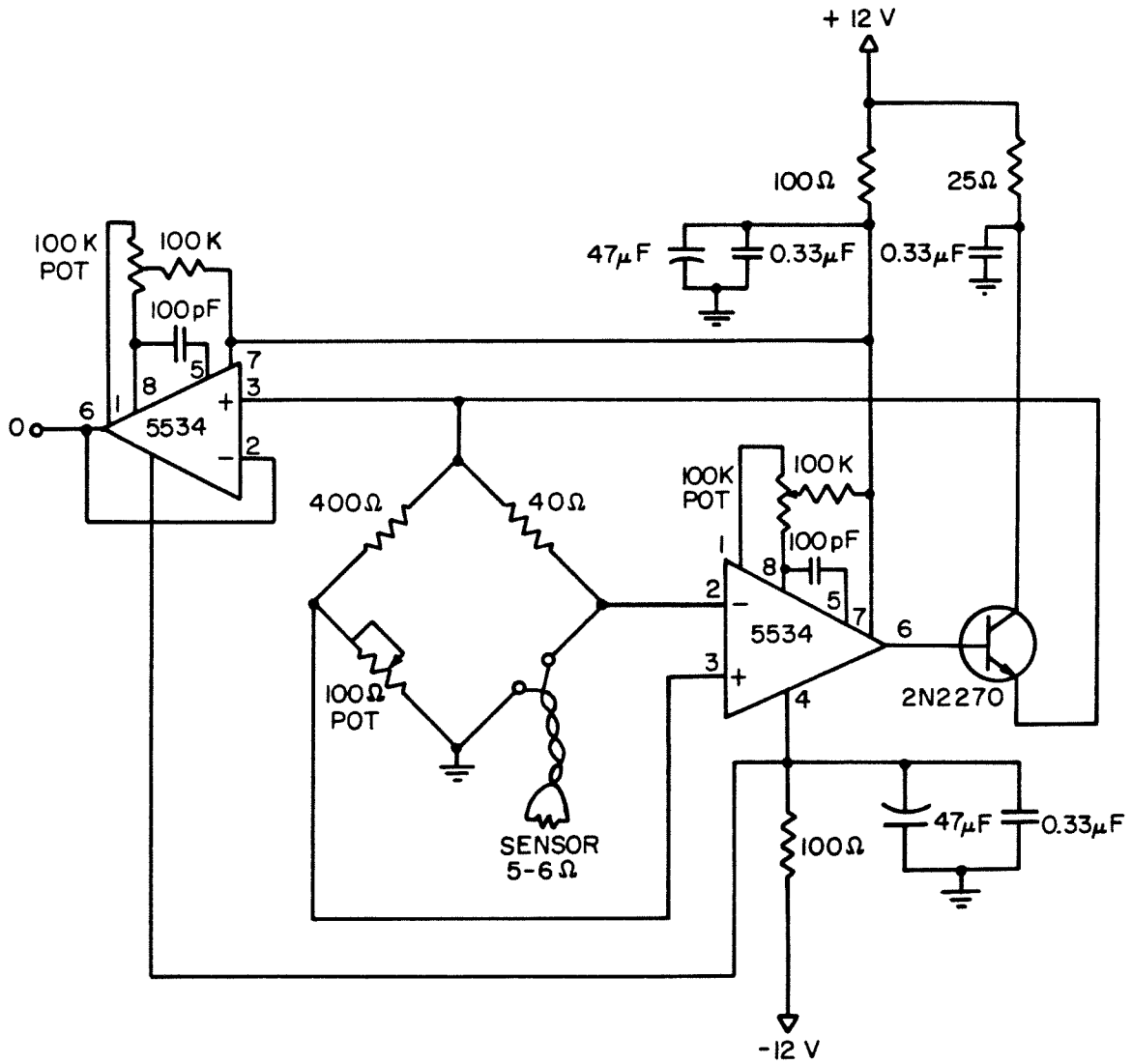
$$S / \delta_m = 5 - 10$$

$$h / \delta_m = 0.4 - 0.8$$

**Figure 2.3** Typical dimensions of tandem manipulator



**Figure 2.4** Wall-shear sensor array, manufactured at GALCIT



**Figure 2.5** Schematic of bridge circuit used to maintain sensors at constant temperature

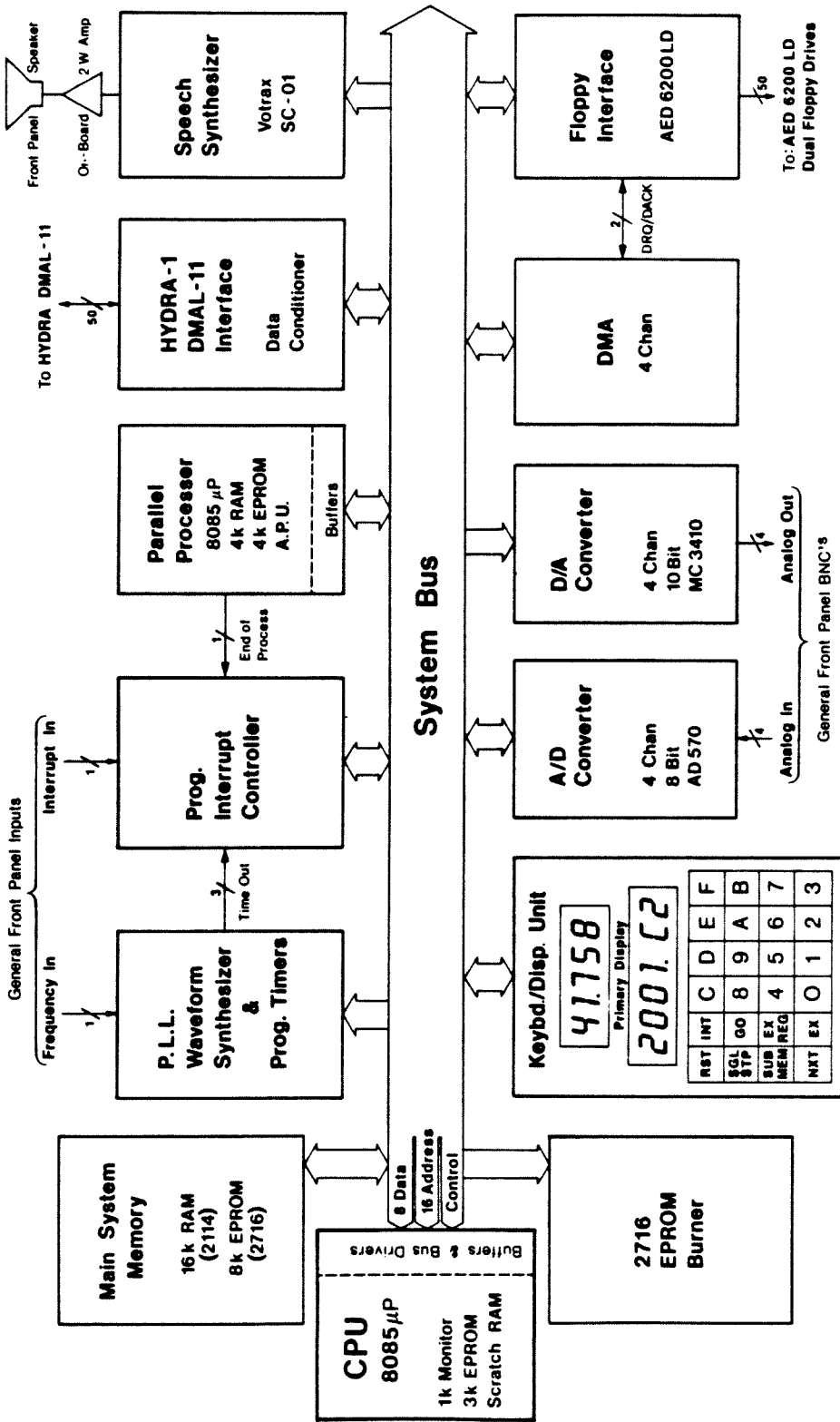


Figure 2.6 Functional schematic of laboratory computer system



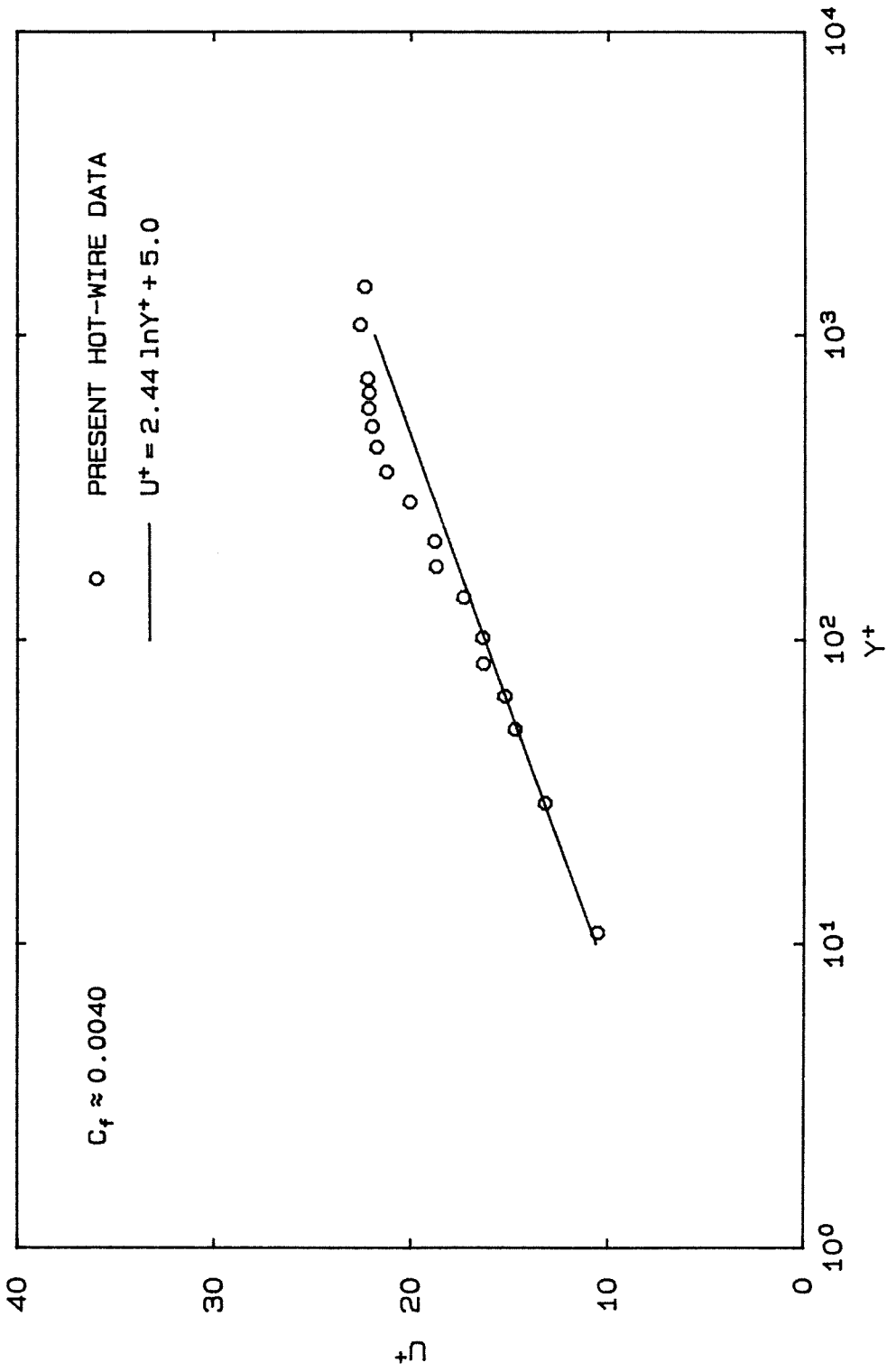


Figure 3.1 Turbulent velocity profile,  $x = 40$  cm,  $Re_\theta = 1200$

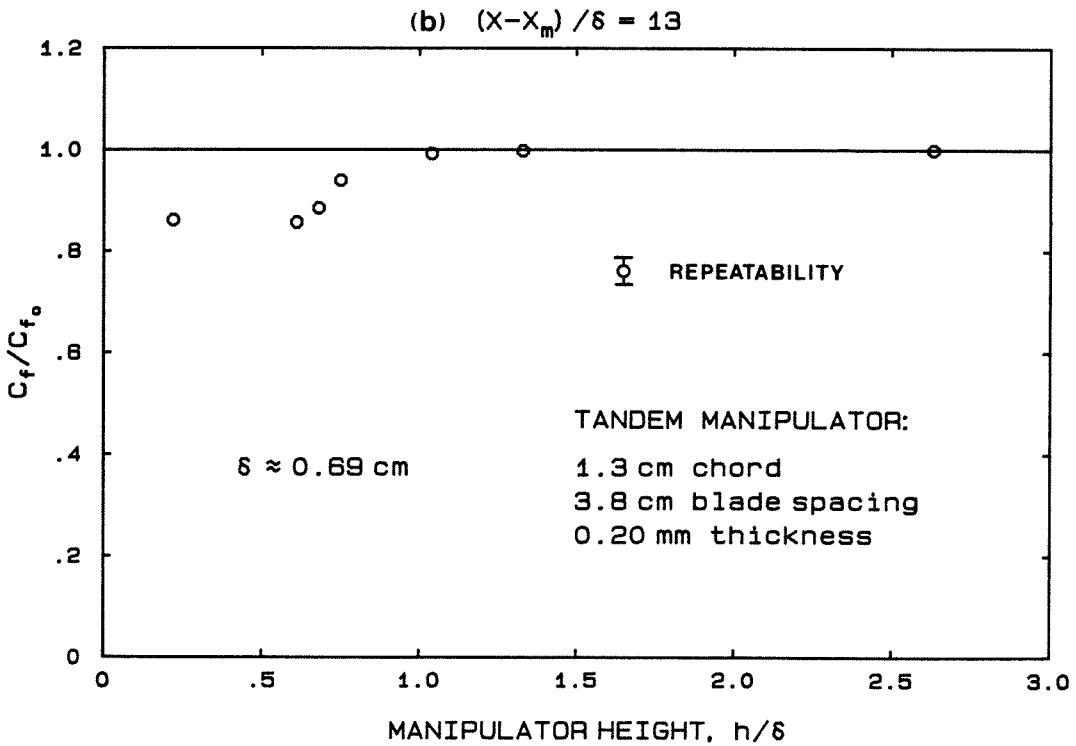
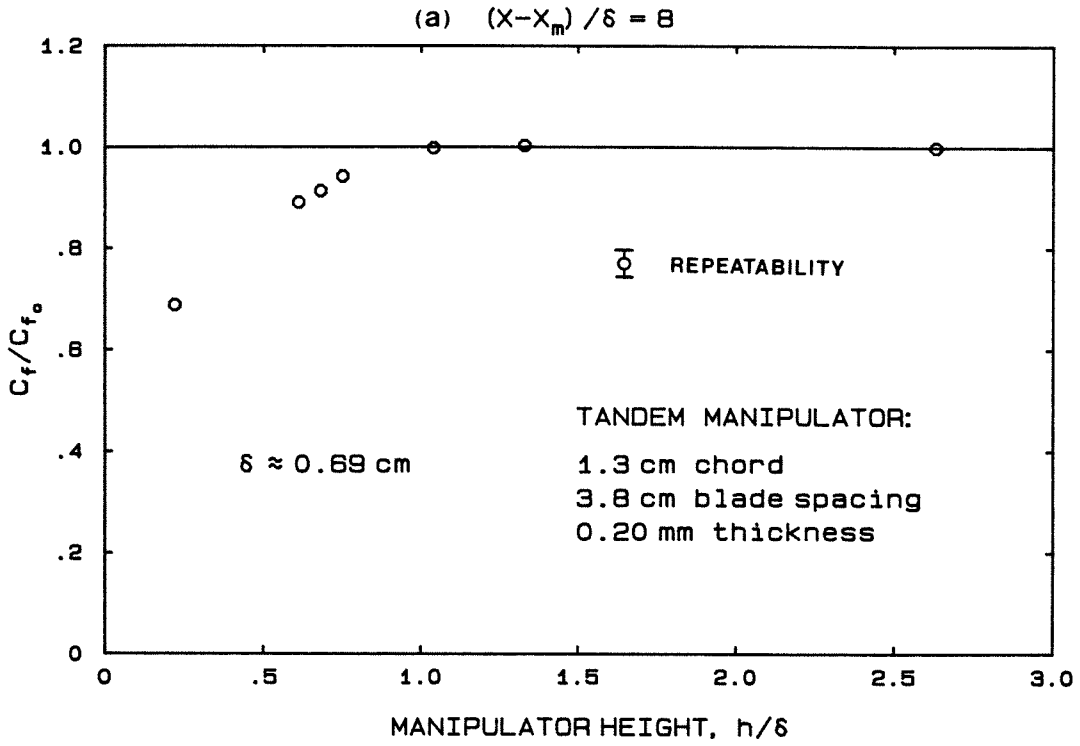
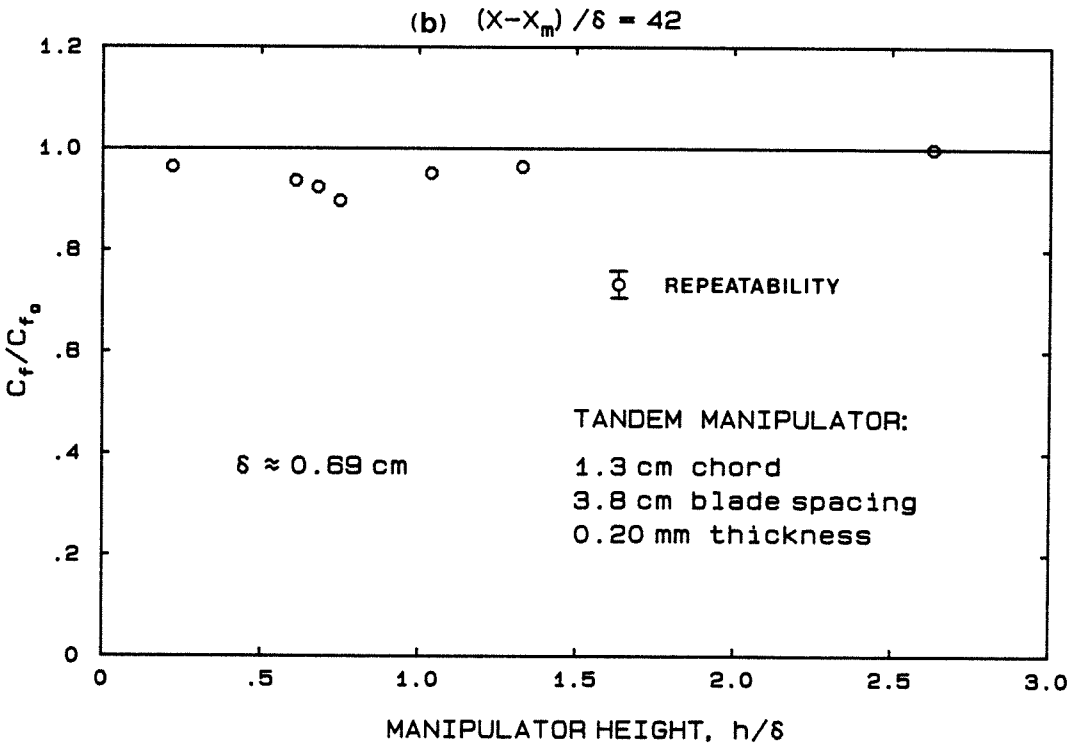
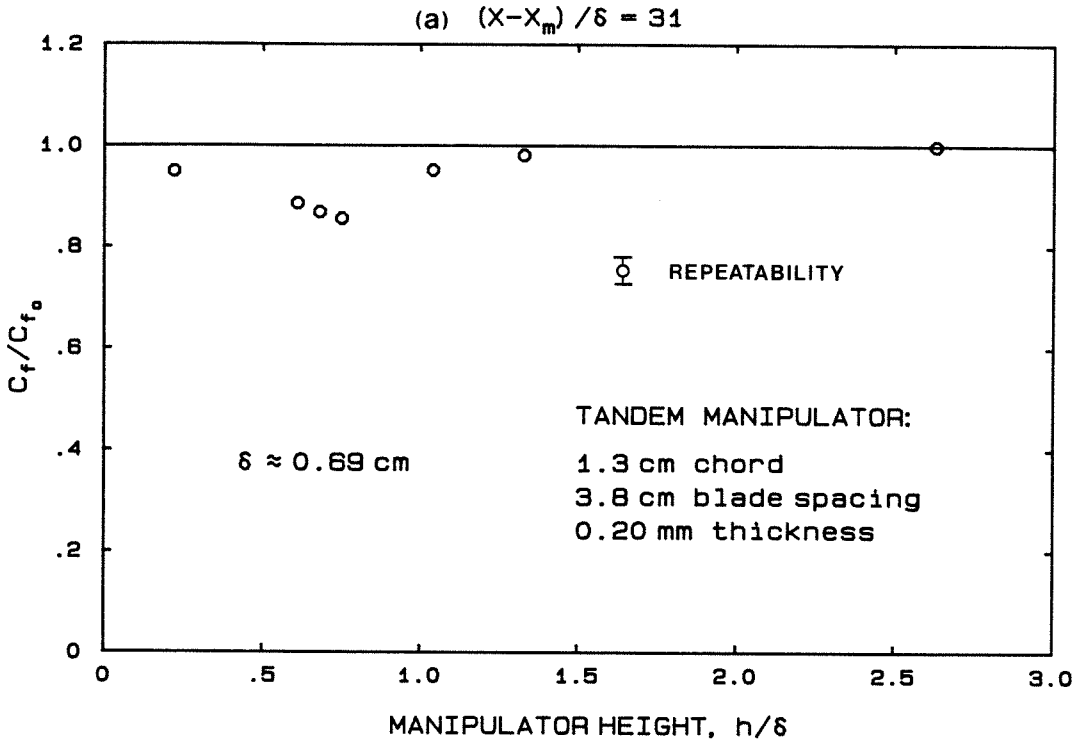


Figure 3.2 Variation of wall-shear reduction with height of manipulator, (a)  $(x-x_m)/\delta_m = 8$ , (b)  $(x-x_m)/\delta_m = 13$



**Figure 3.3** Variation of wall-shear reduction with height of manipulator  
(a)  $(x-x_m)/\delta_m = 31$ , (b)  $(x-x_m)/\delta_m = 42$

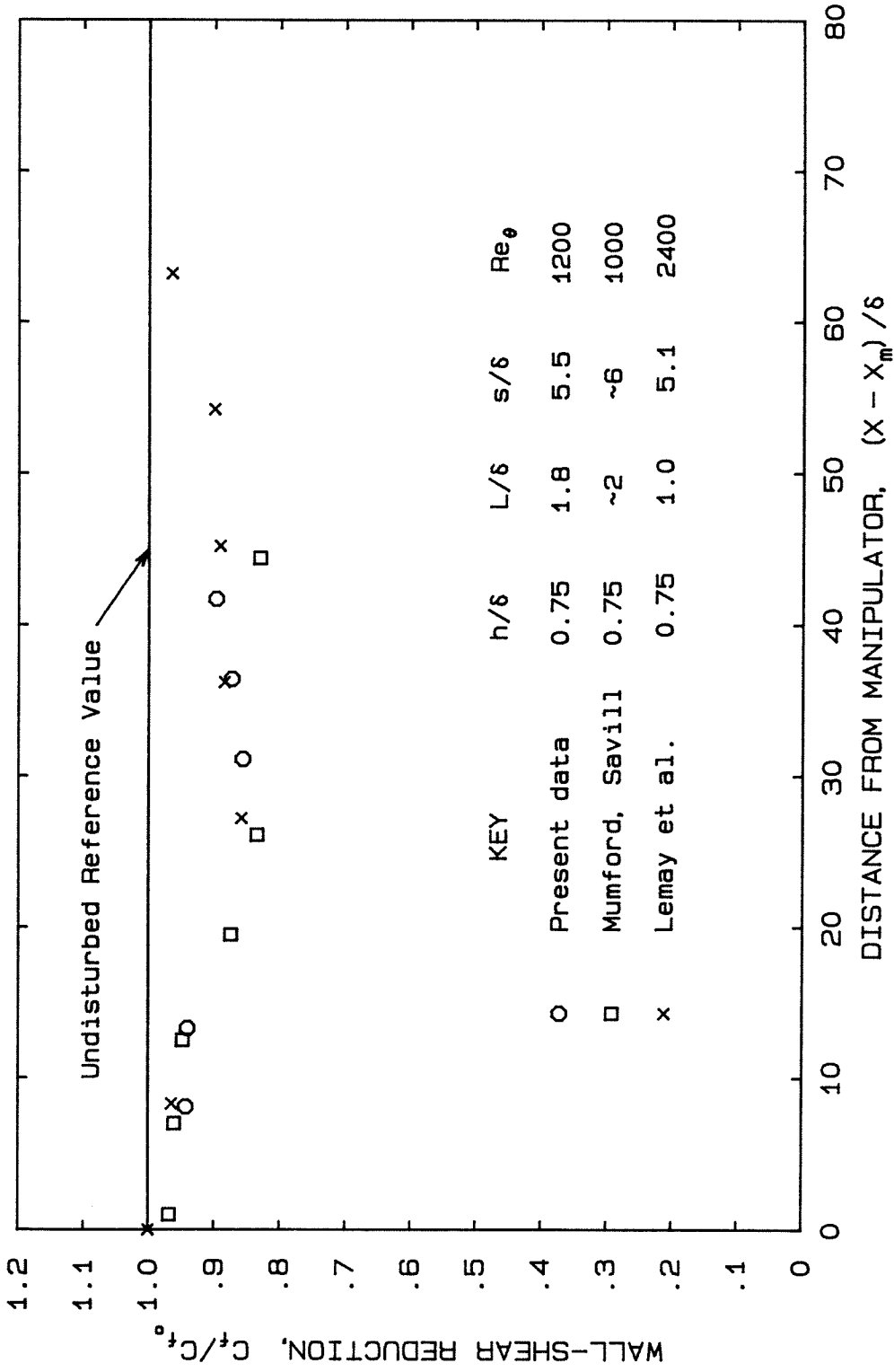
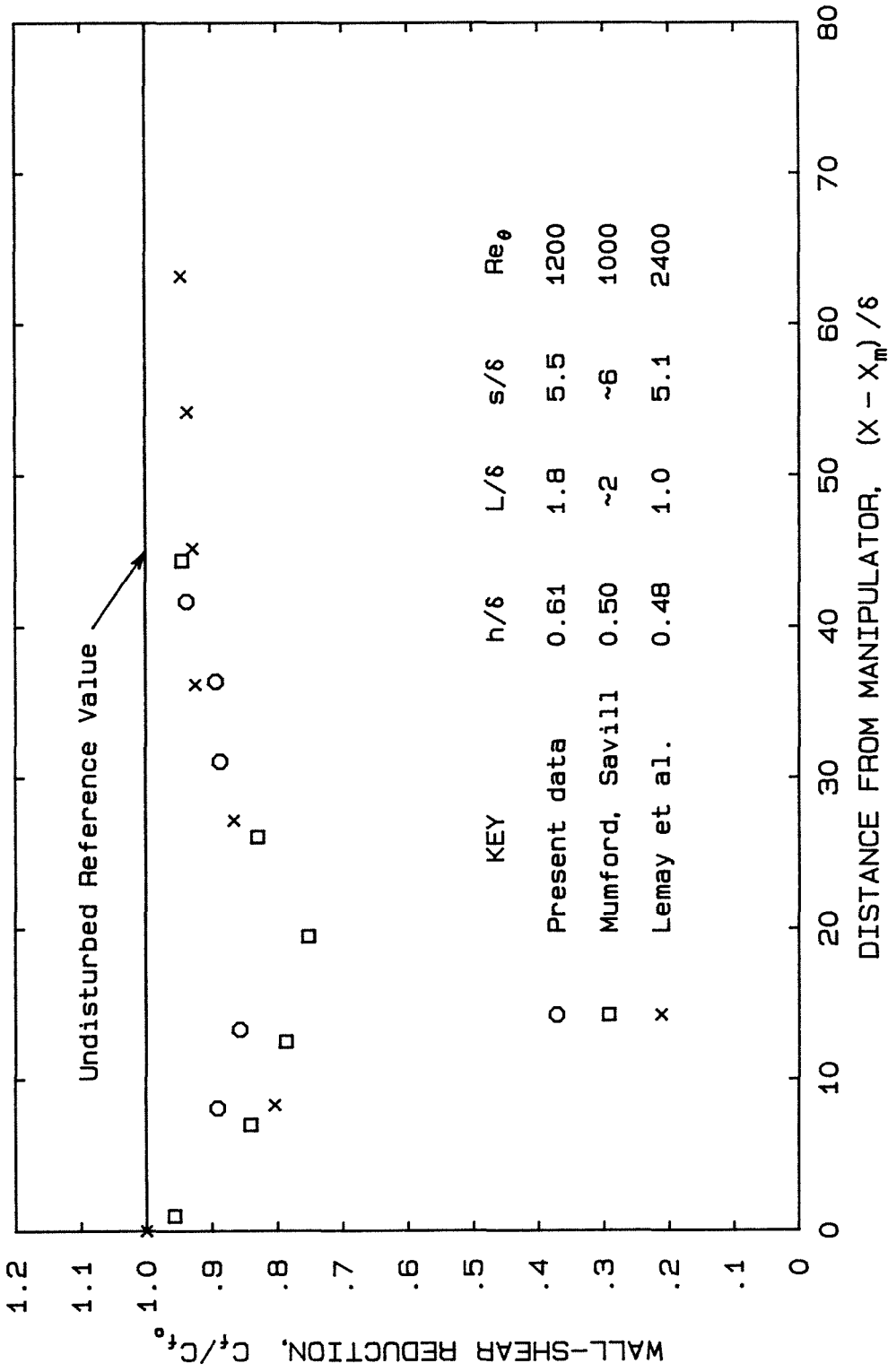
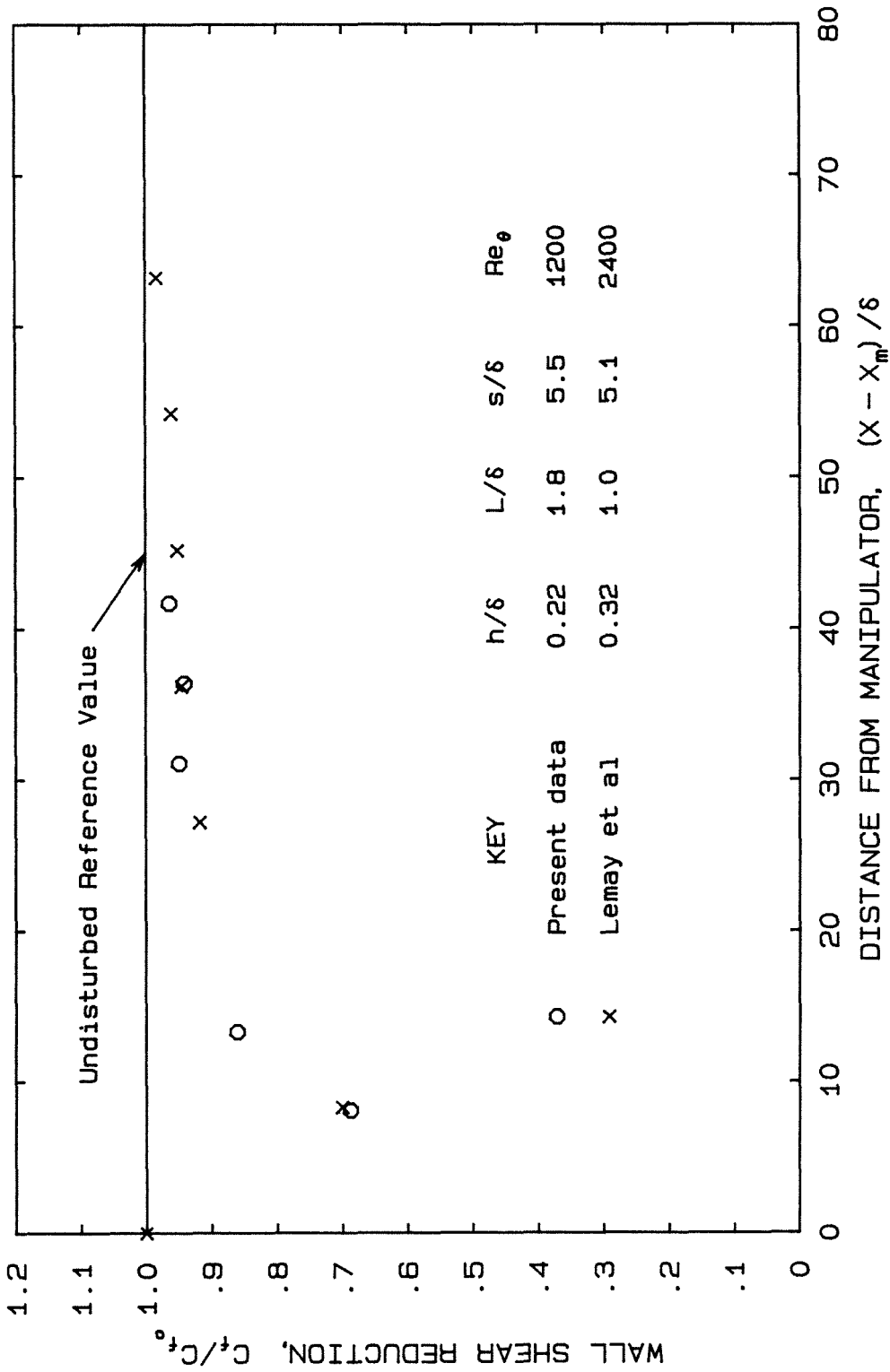


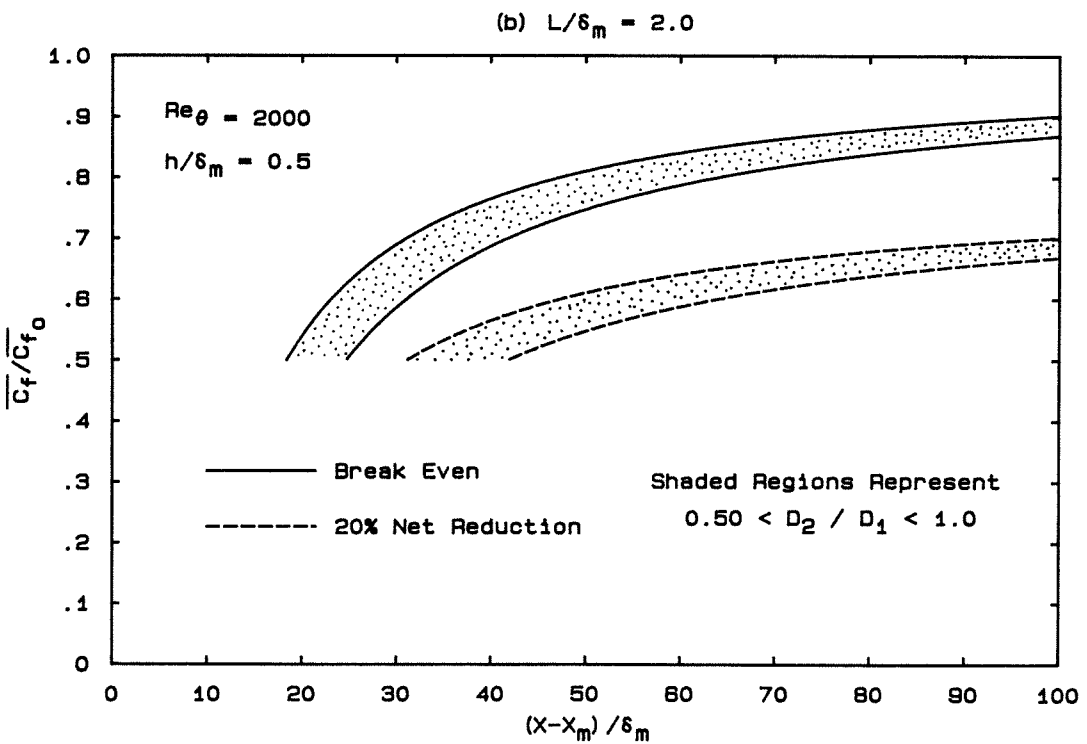
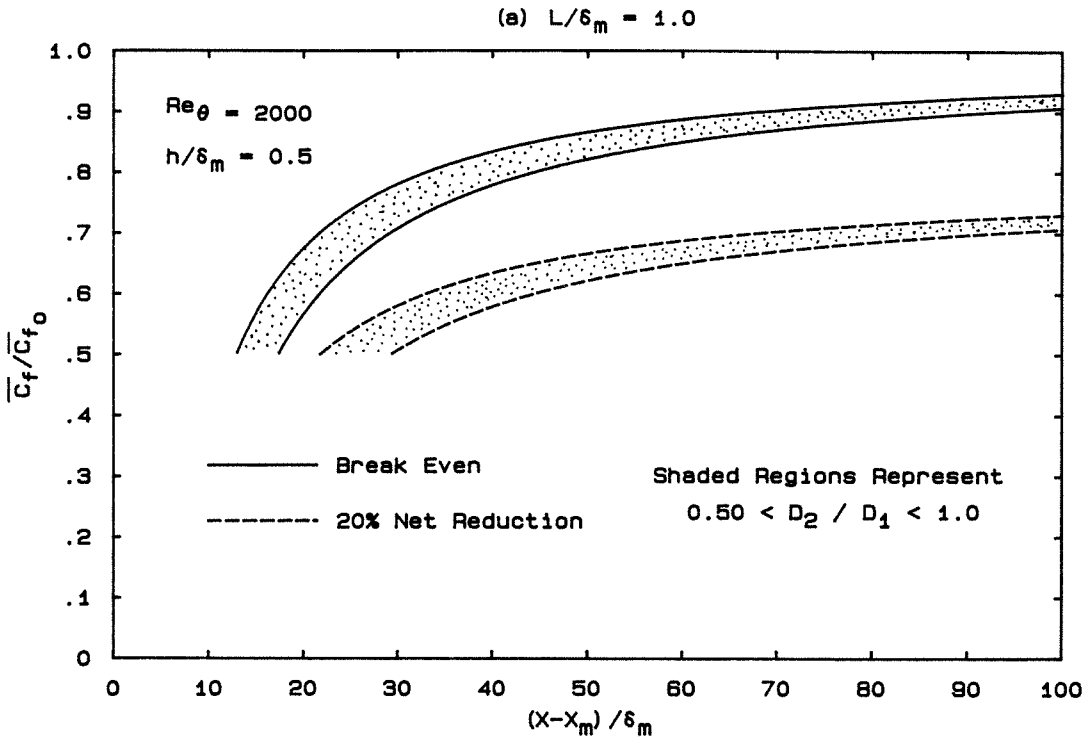
Figure 3.4 Mean wall-shear distribution downstream of tandem manipulator,  $h/\delta_m \approx 0.75$



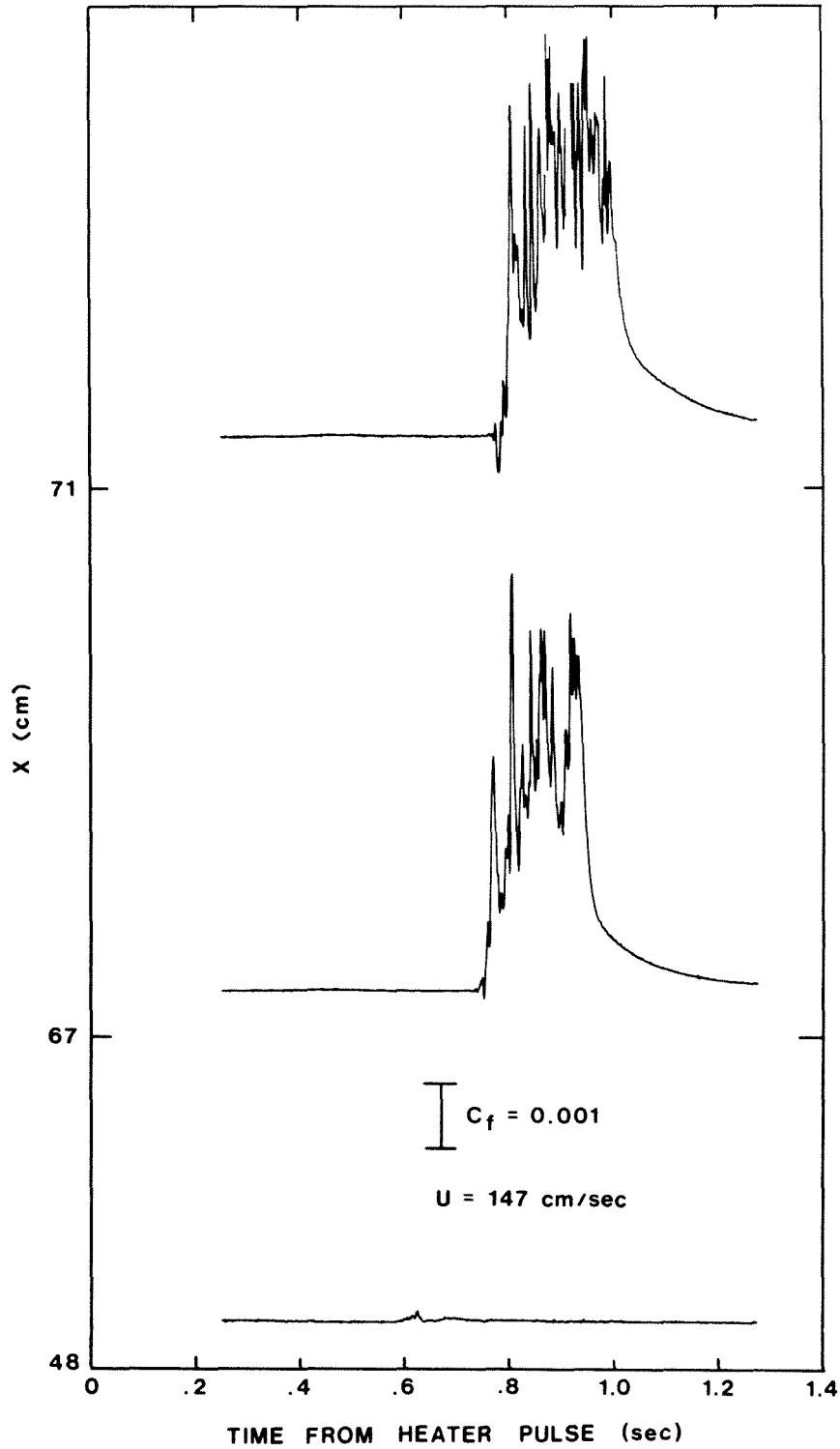
**Figure 3.5** Mean wall-shear distribution downstream of tandem manipulator,  $h/\delta_m \approx 0.50$



**Figure 3.6** Mean wall-shear distribution downstream of tandem manipulator,  $h/\delta_m \approx 0.25$

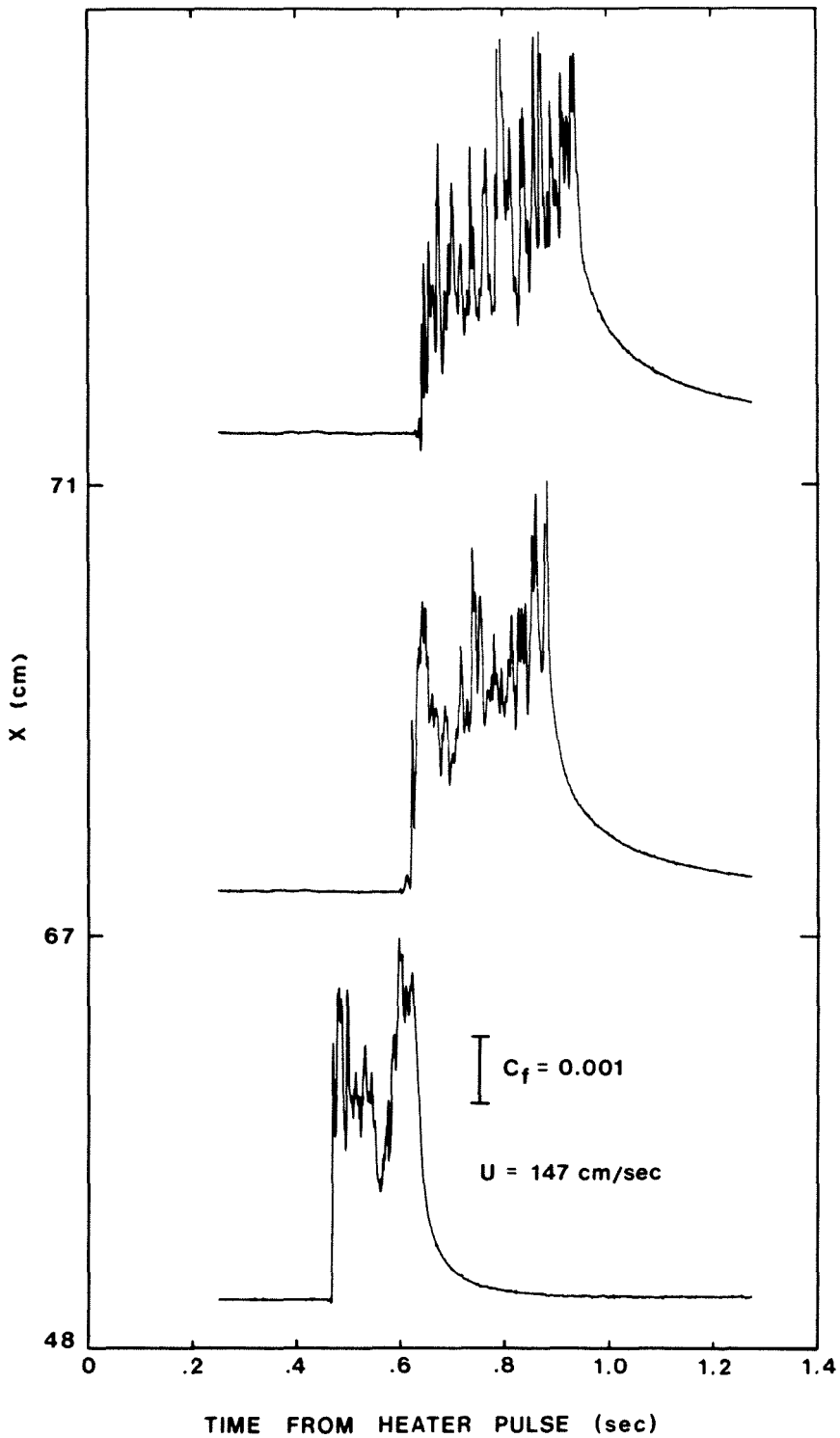


**Figure 3.7** Minimum required wall-shear reductions (spatially averaged) for net drag reduction.  $Re_\theta = 2000$ .  
(a)  $L/\delta_m = 1.0$ , (b)  $L/\delta_m = 2.0$



**Figure 4.1** Streamwise evolution of an individual spot generated from a *low*-amplitude heated-element pulse





**Figure 4.2** Streamwise evolution of an individual spot generated from a *high*-amplitude heated-element pulse

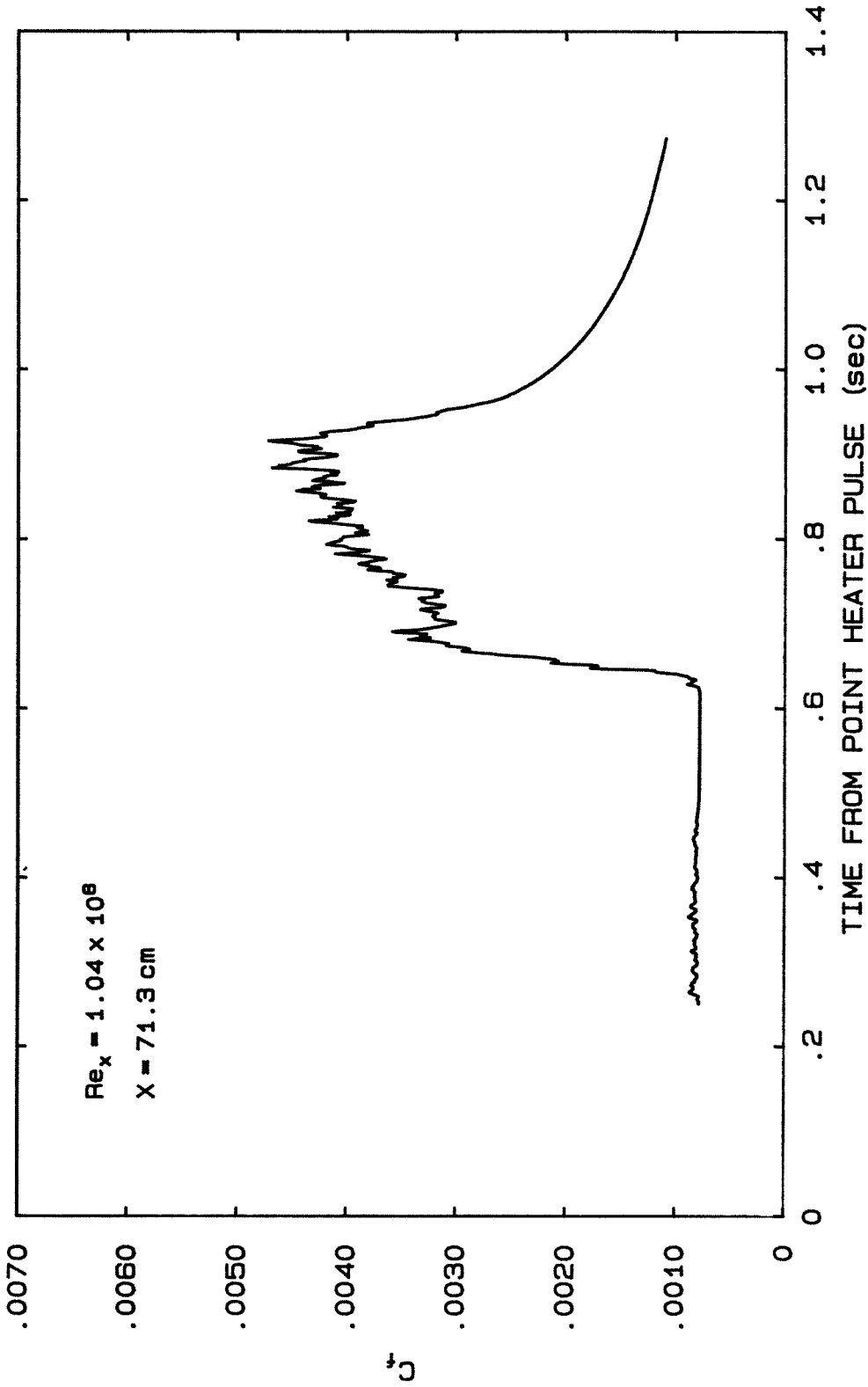


Figure 4.3 Ensemble-averaged wall-shear time history of a turbulent spot

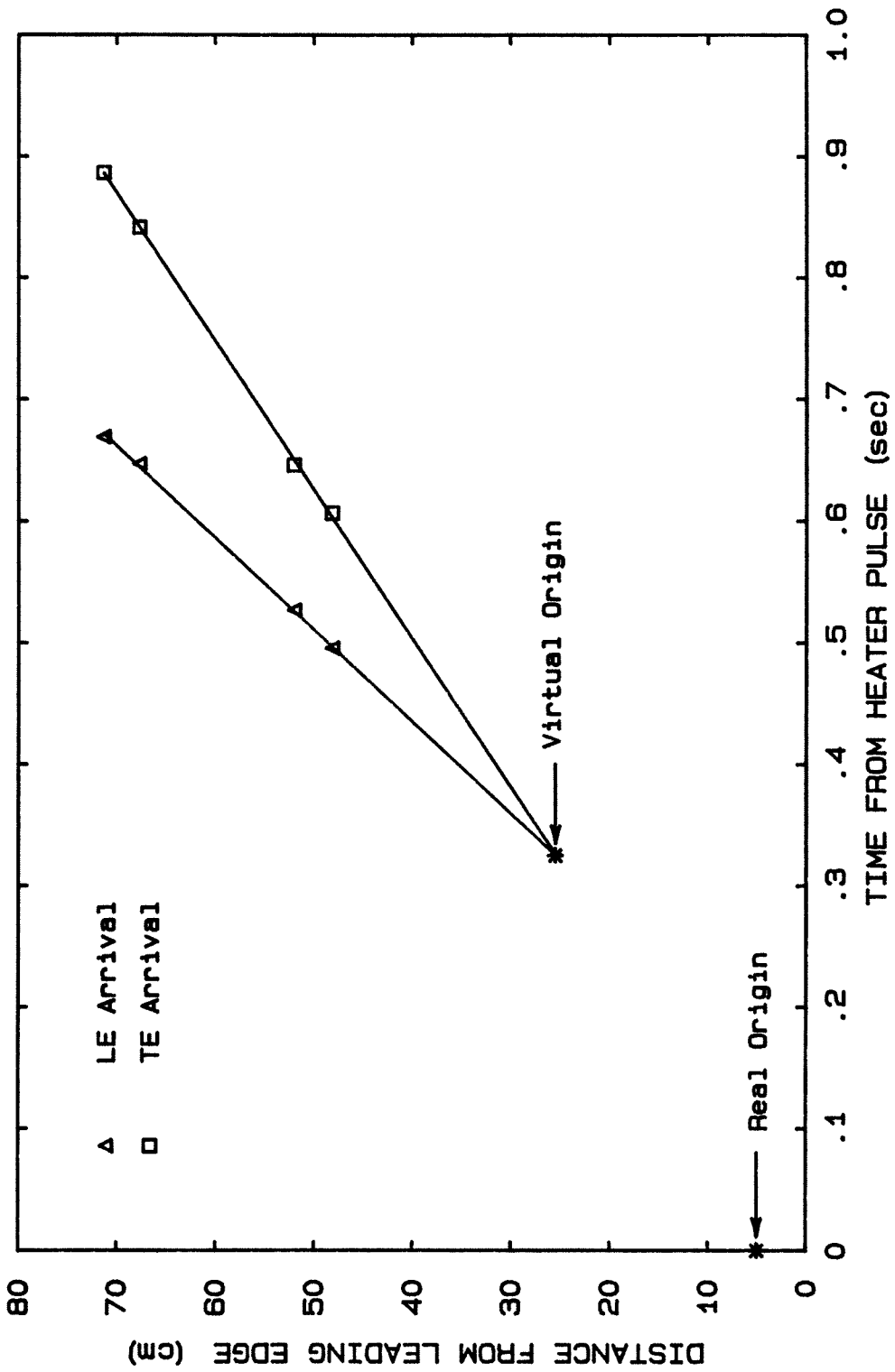


Figure 4.4 x-t diagram for a typical turbulent spot

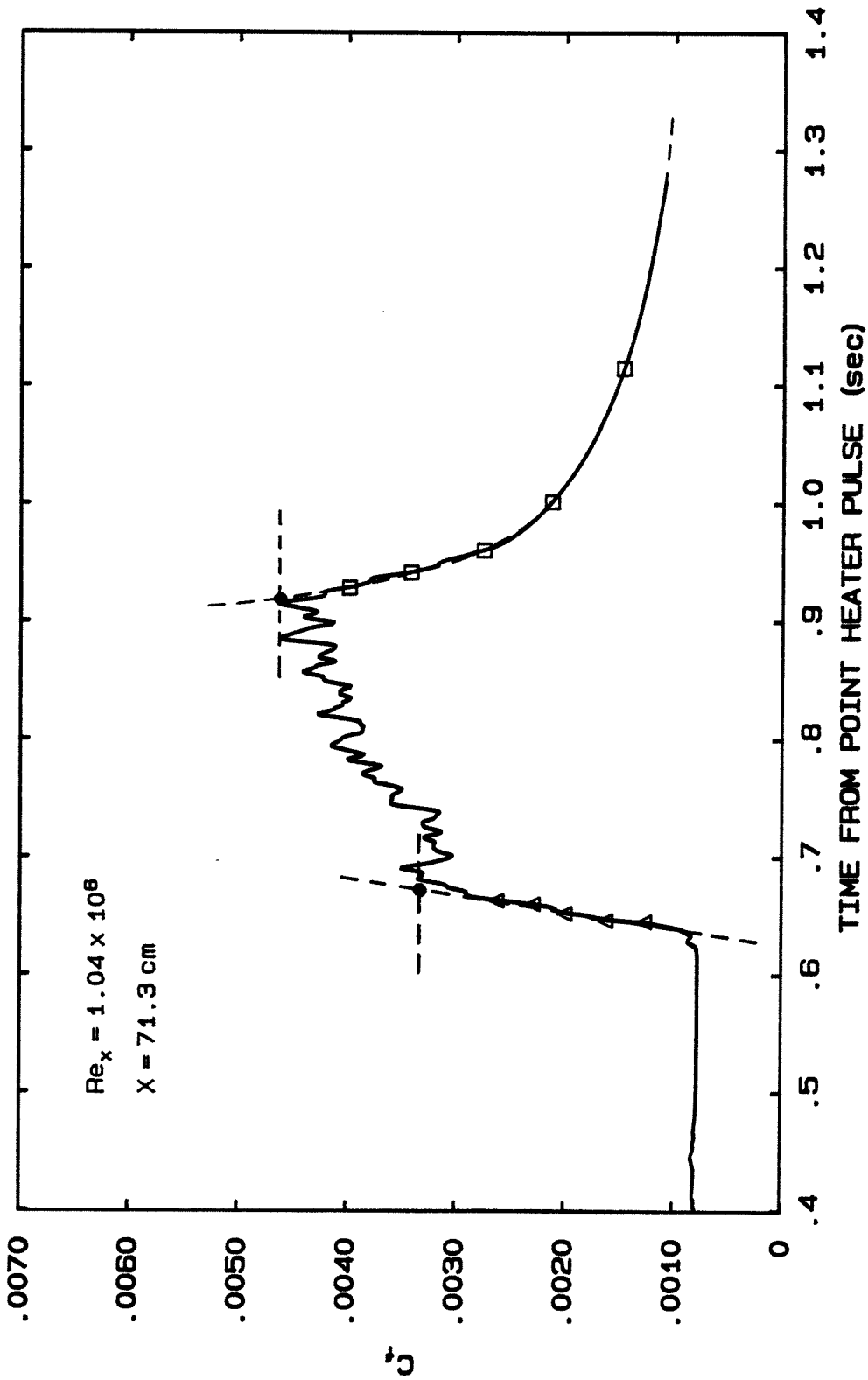
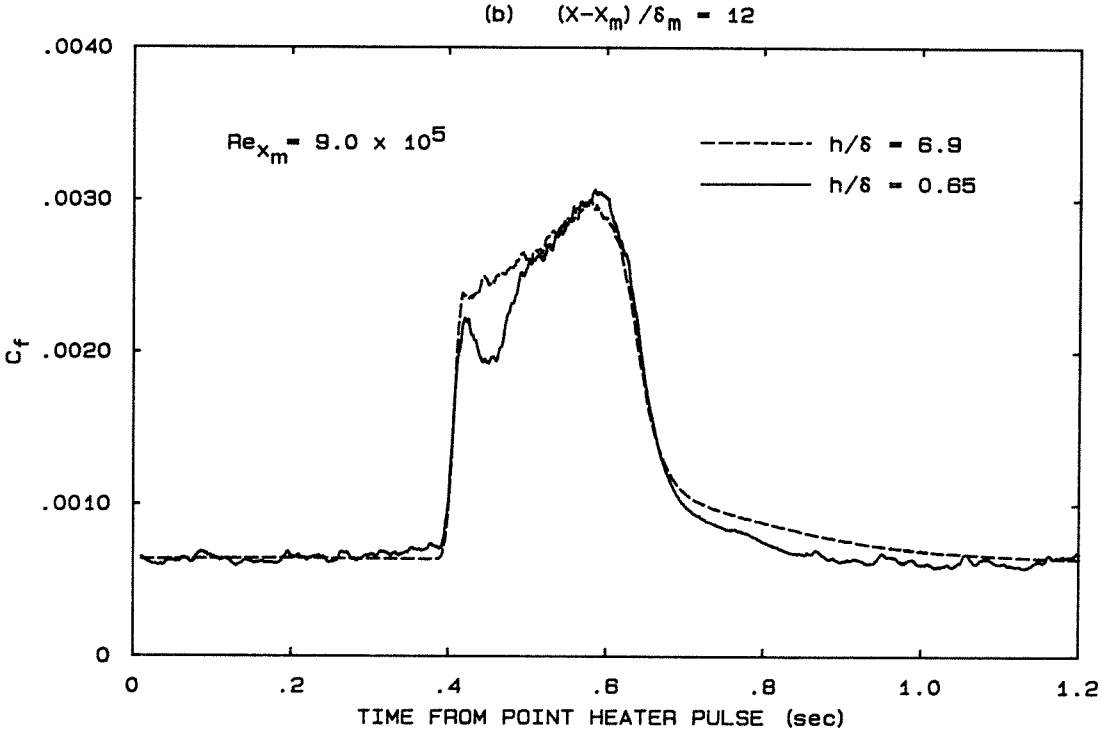
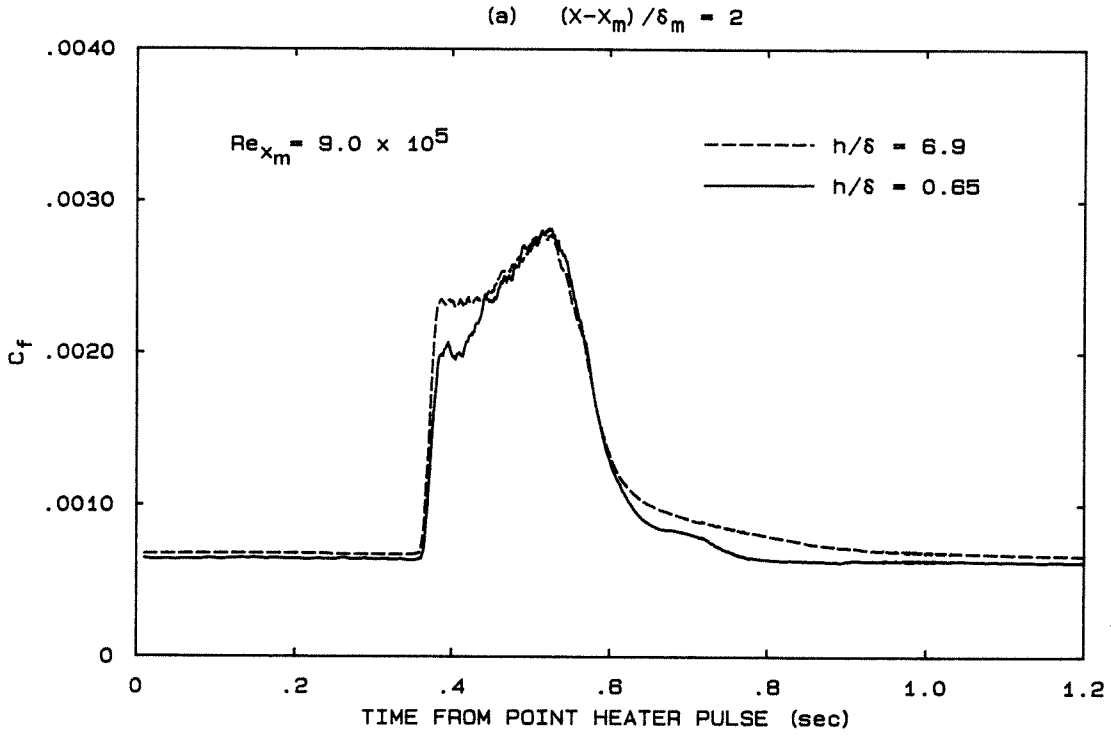


Figure 4.5 Criteria used to determine interface arrival times



**Figure 4.6** Tandem manipulator effects on the wall shear of an ensemble-averaged spot; laminar ambient boundary layer.  $h/\delta_m \approx 0.65$   
(a)  $(x-x_m)/\delta_m = 2$ , (b)  $(x-x_m)/\delta_m = 12$

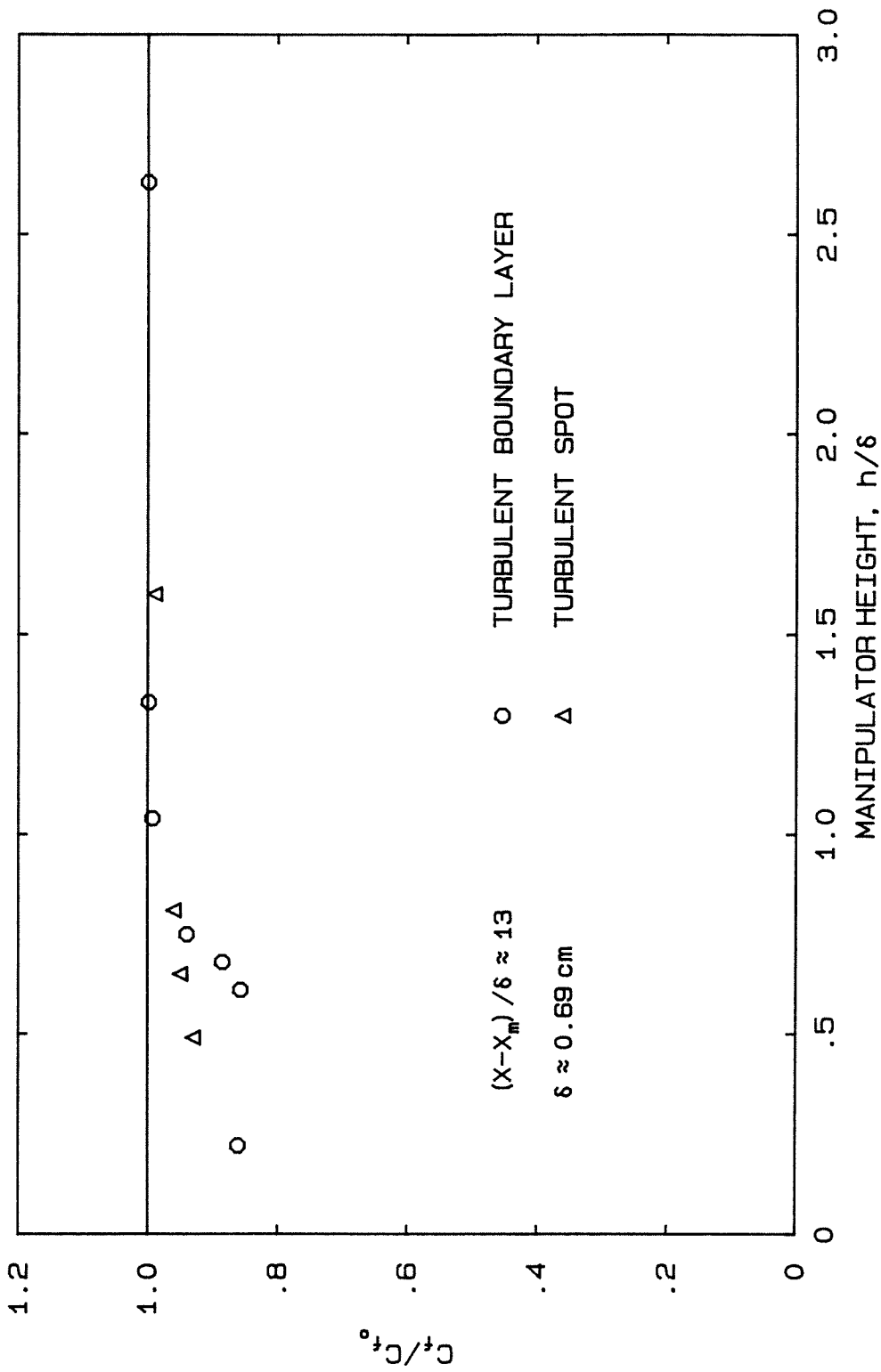
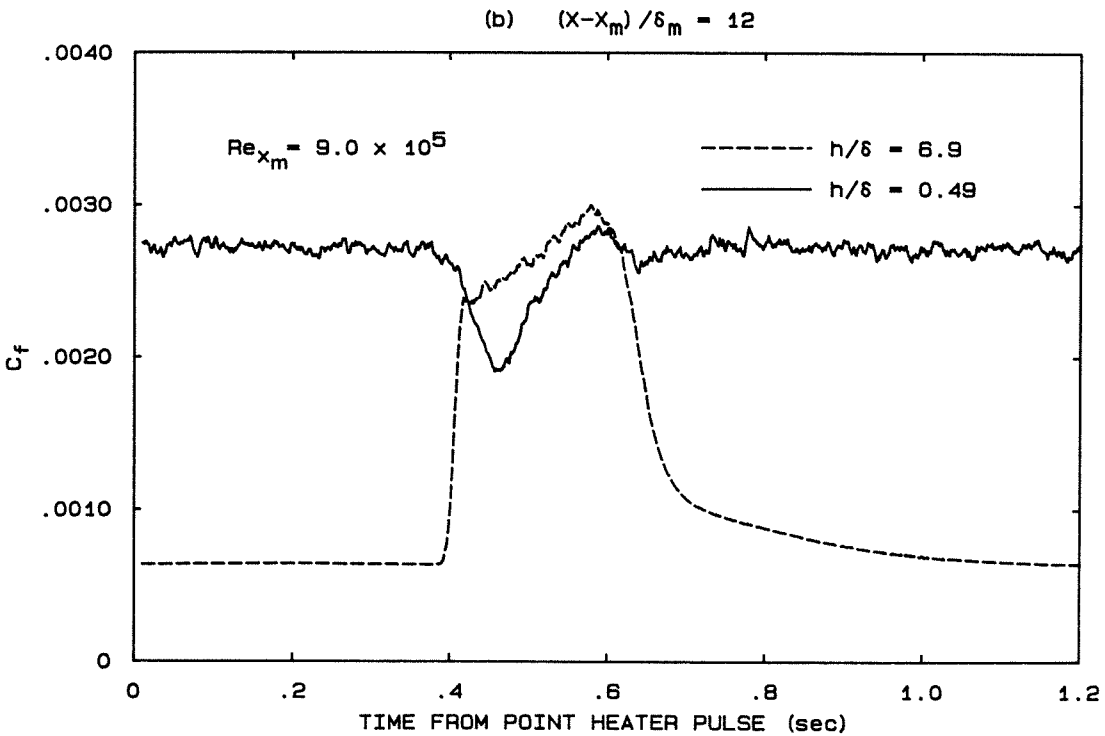
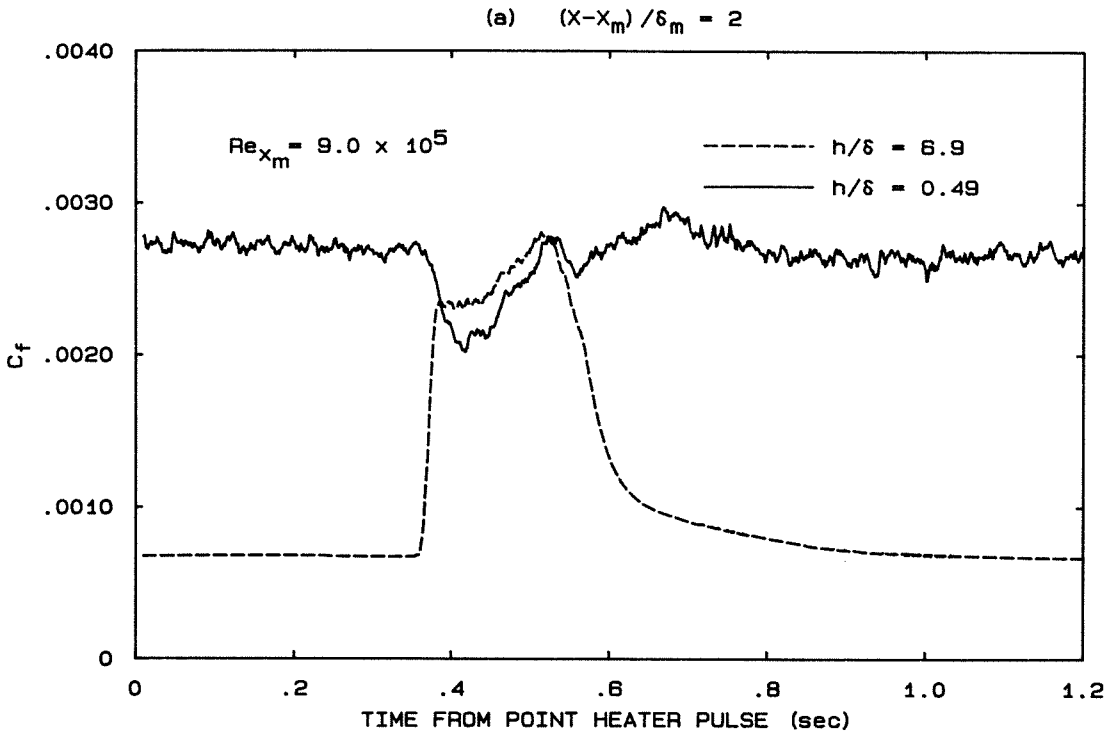
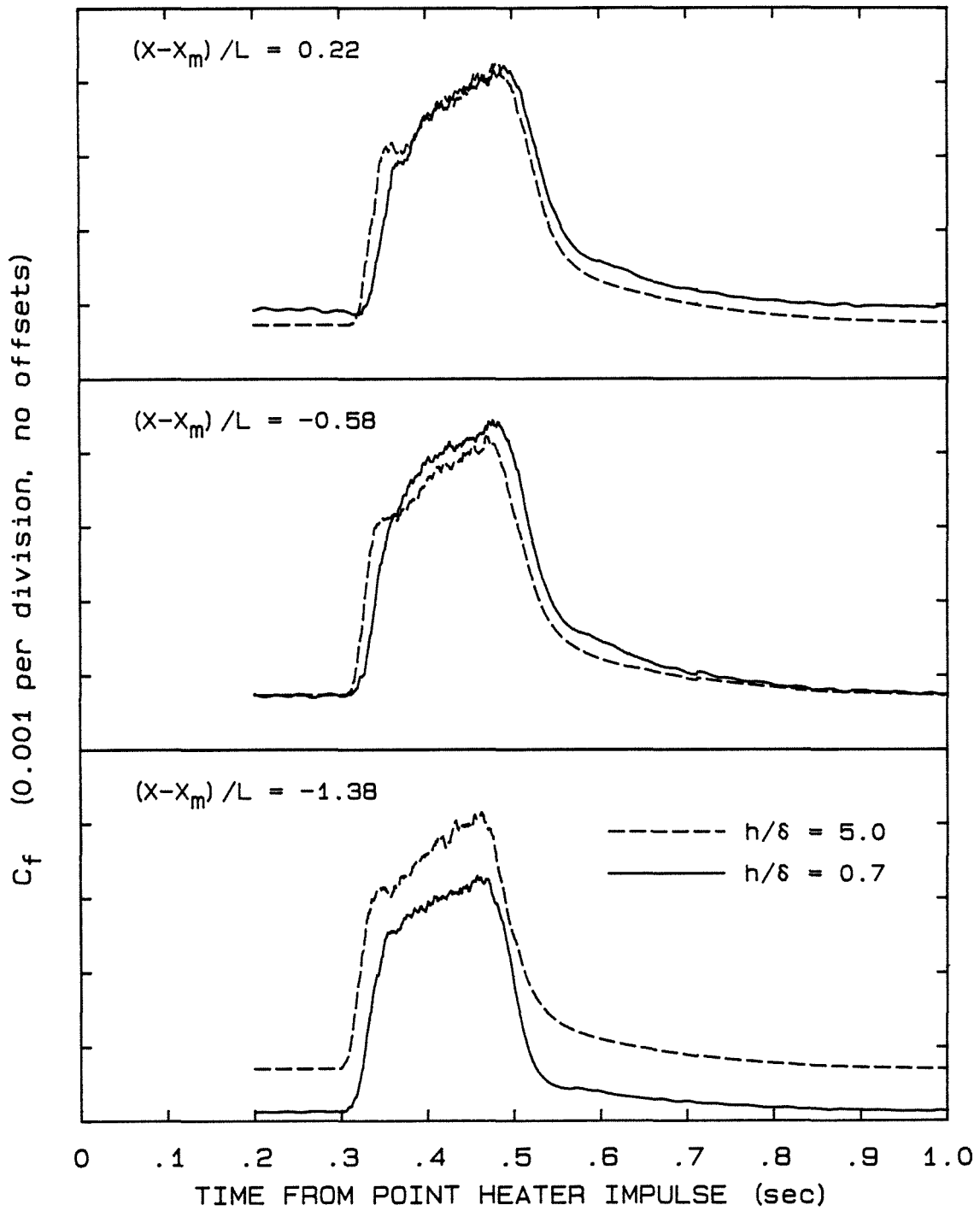


Figure 4.7 Effect of manipulator height on mean wall-shear reduction

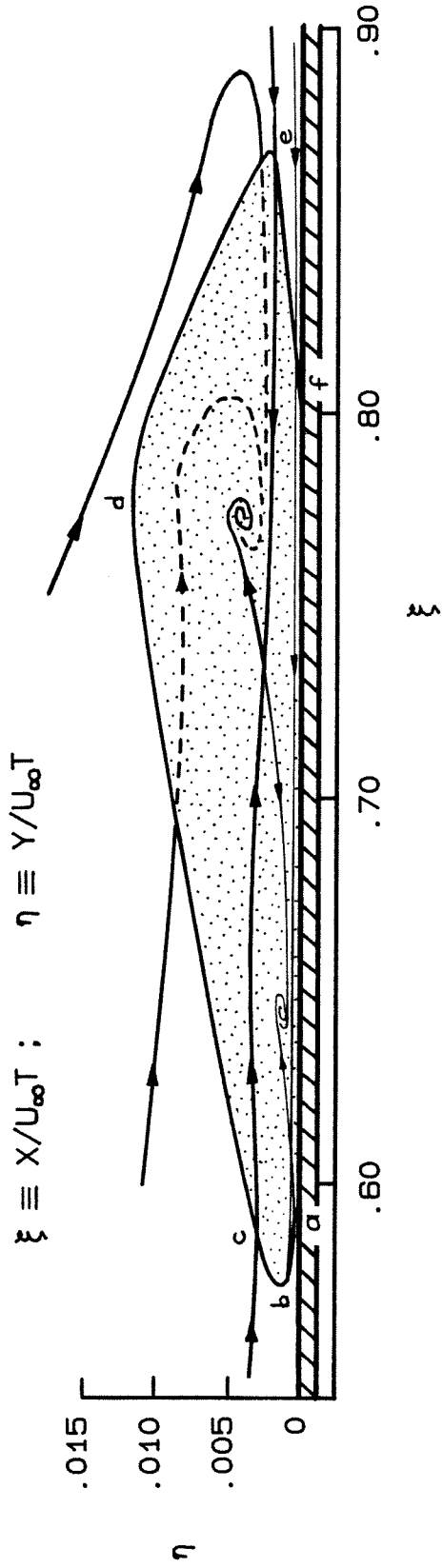


**Figure 4.8** Tandem manipulator effects on the wall shear of an ensemble-averaged spot; transitional ambient boundary layer.  $h/\delta_m \approx 0.49$   
(a)  $(x-x_m)/\delta_m = 2$ , (b)  $(x-x_m)/\delta_m = 12$



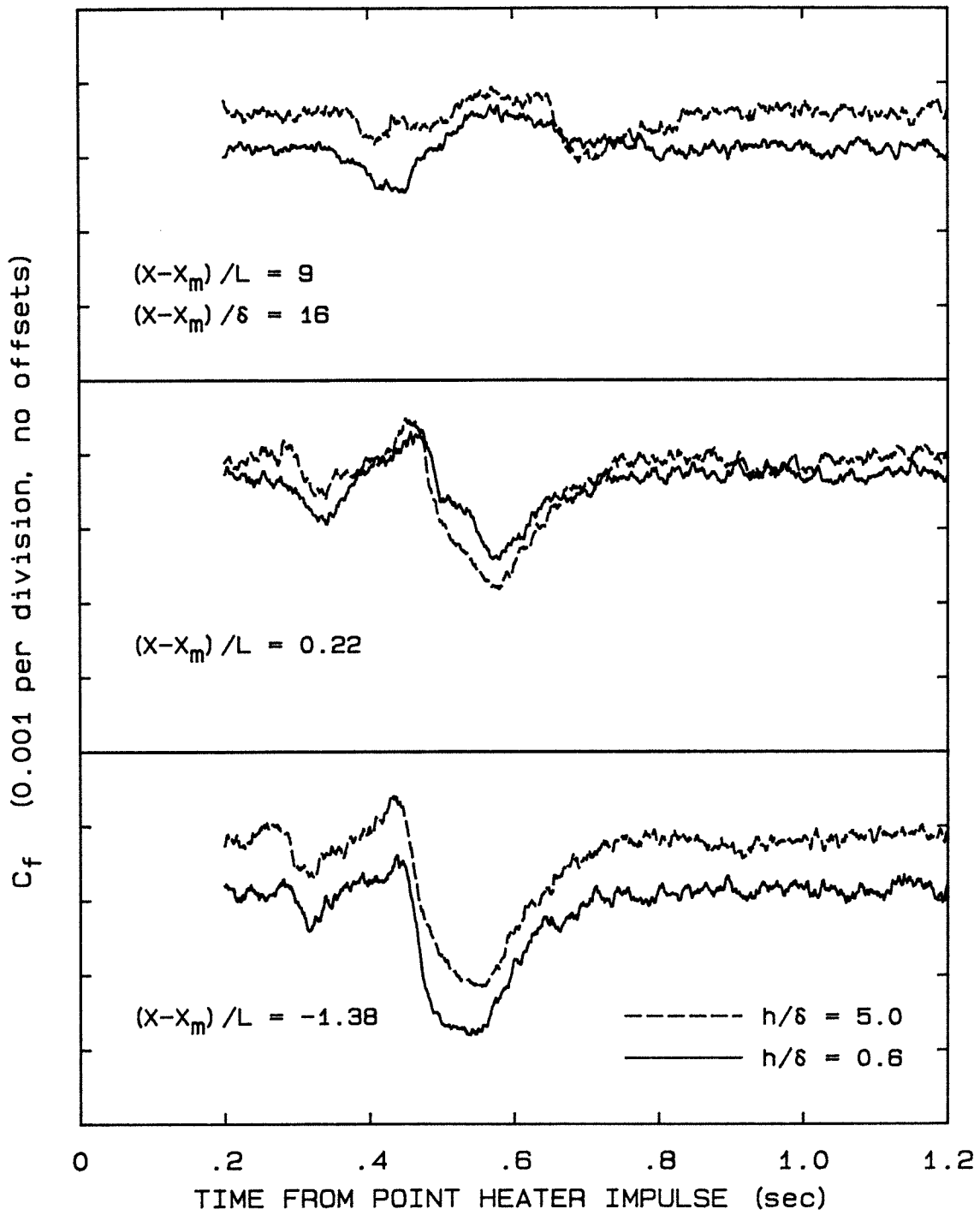
**Figure 4.9** Wall-shear behavior of turbulent spot in the neighborhood of a manipulator blade,  $h/\delta_m \approx 0.70$





REGION	BOUNDARY ARC	REL. ENTRAINMENT
Outer	cd	58
Intermediate and Wall	de	7
	ab	-2
	bc	23
	ef	14

**Figure 4.10** Structure and entrainment characteristics of an ensemble-averaged spot [after Cantwell, Coles, and Dimotakis (1978)]



**Figure 4.11** Manipulated spot propagating in a fully turbulent ambient boundary layer

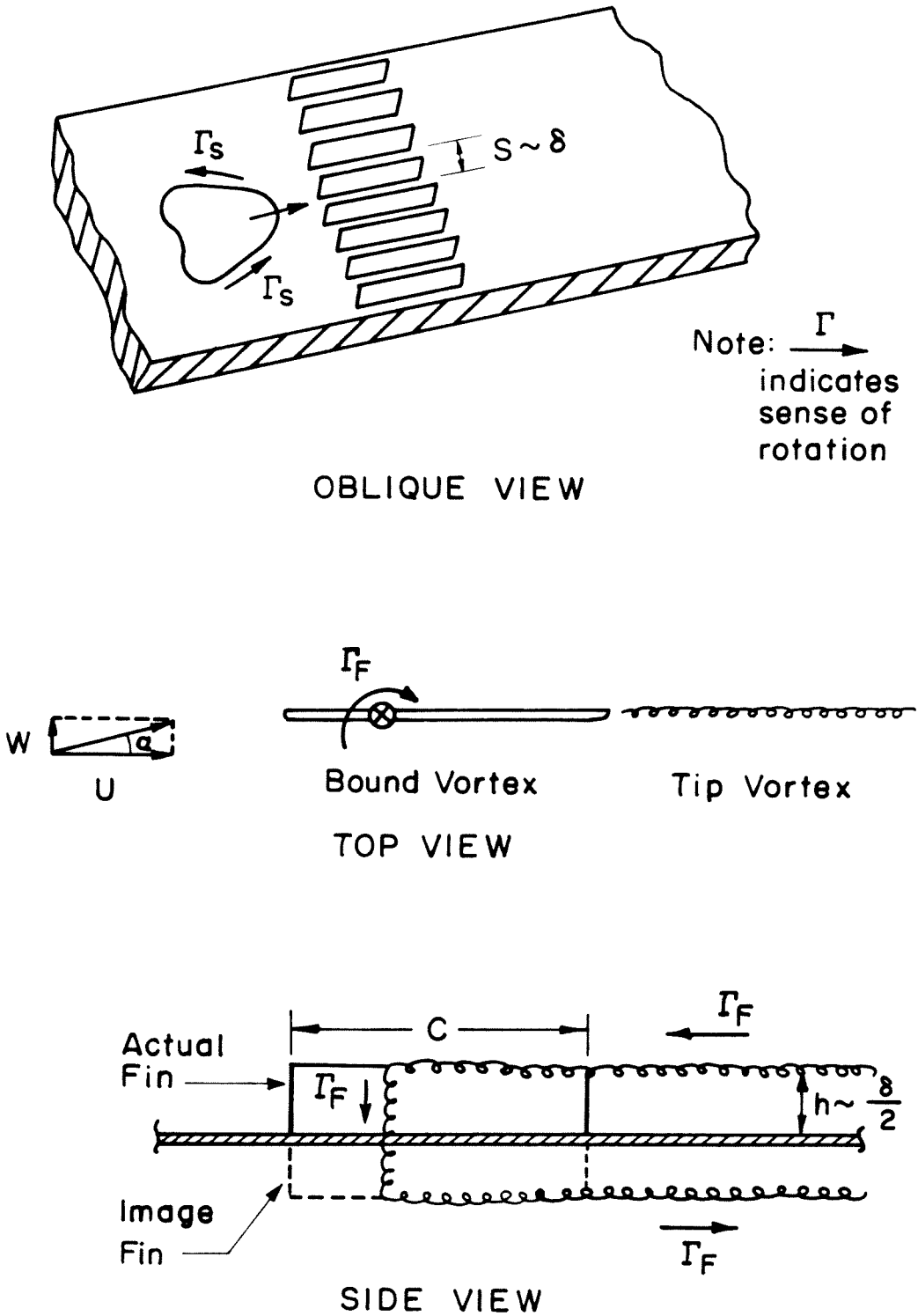


Figure 5.1 Schematic of vertical-fin manipulator

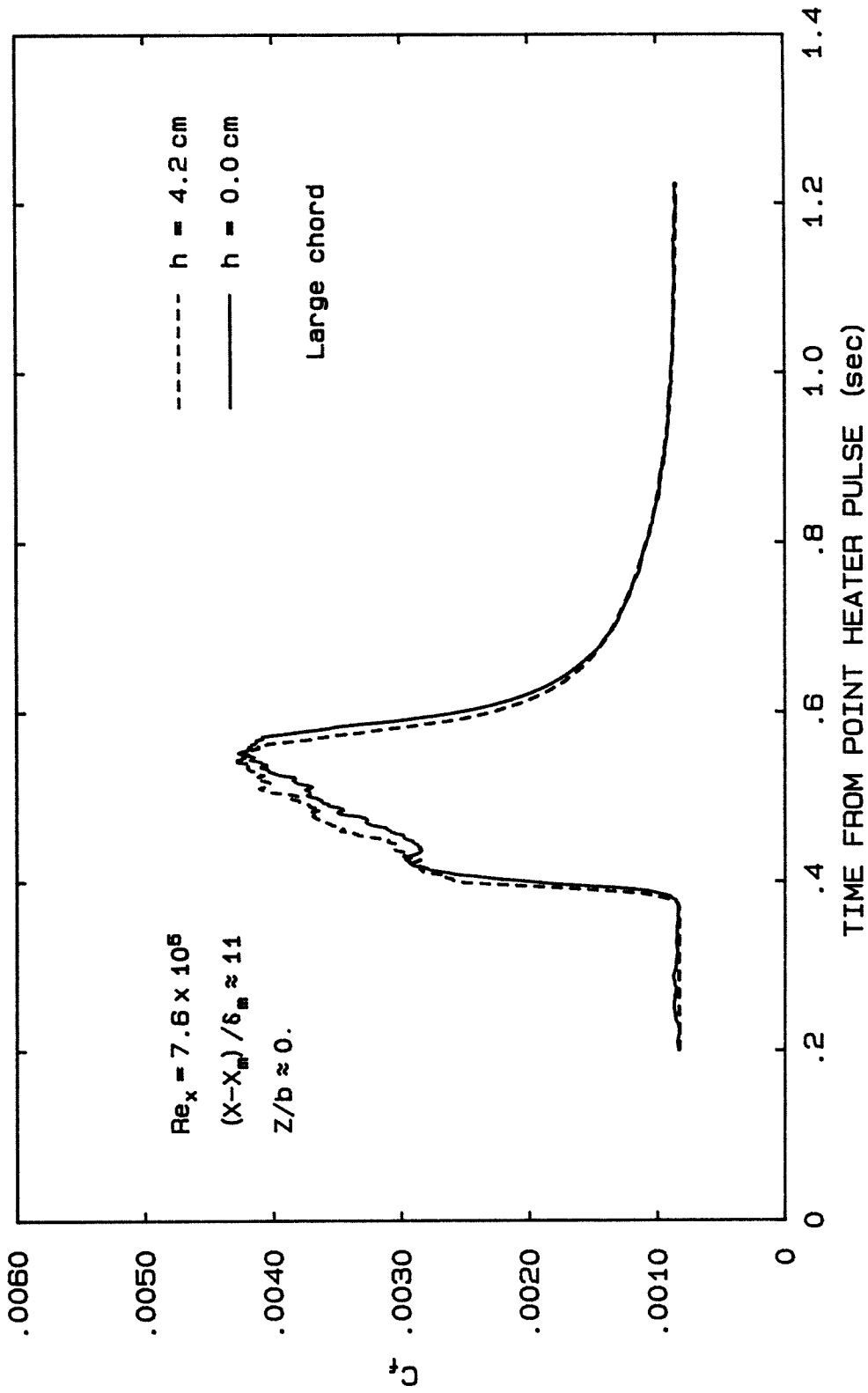


Figure 5.2 Turbulent spot wall-shear behavior due to long-chord, vertical-fin device,  $z/b = 0$

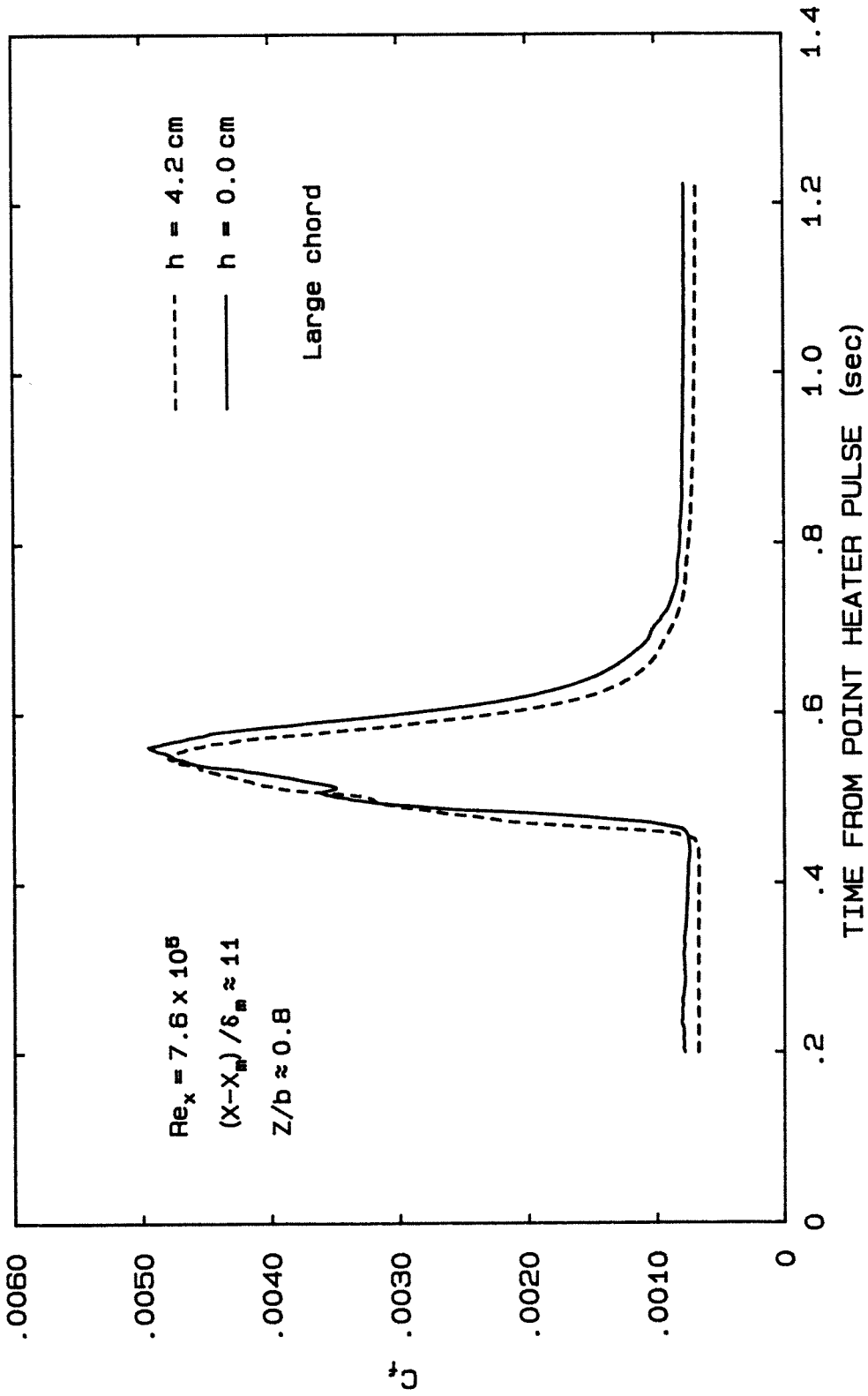


Figure 5.3 Turbulent spot wall-shear behavior due to long-chord, vertical-fin device, z/b = 0.8

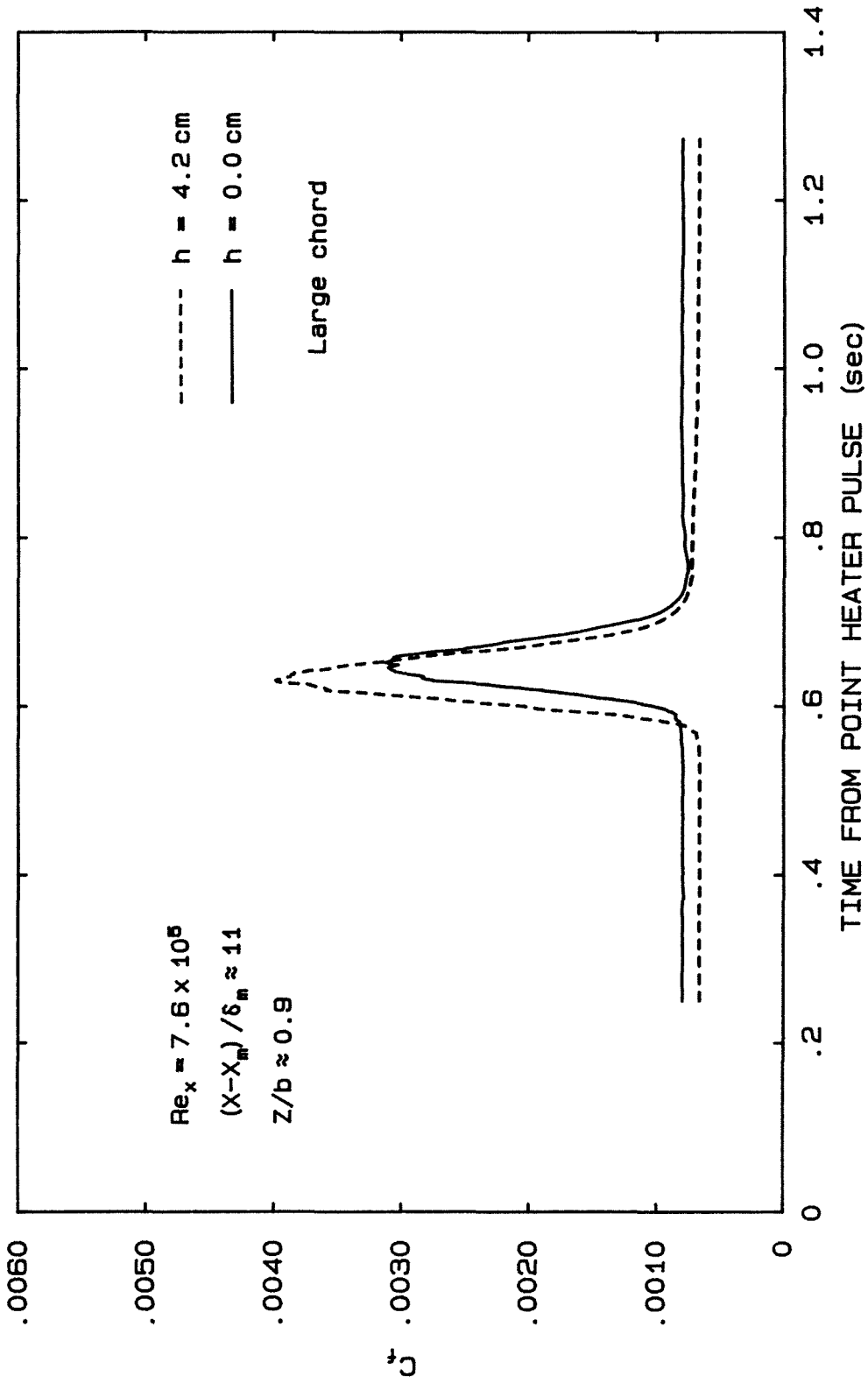


Figure 5.4 Turbulent spot wall-shear behavior at its spanwise extremity.  
Long-chord, vertical-fin device. z/b = 0.9

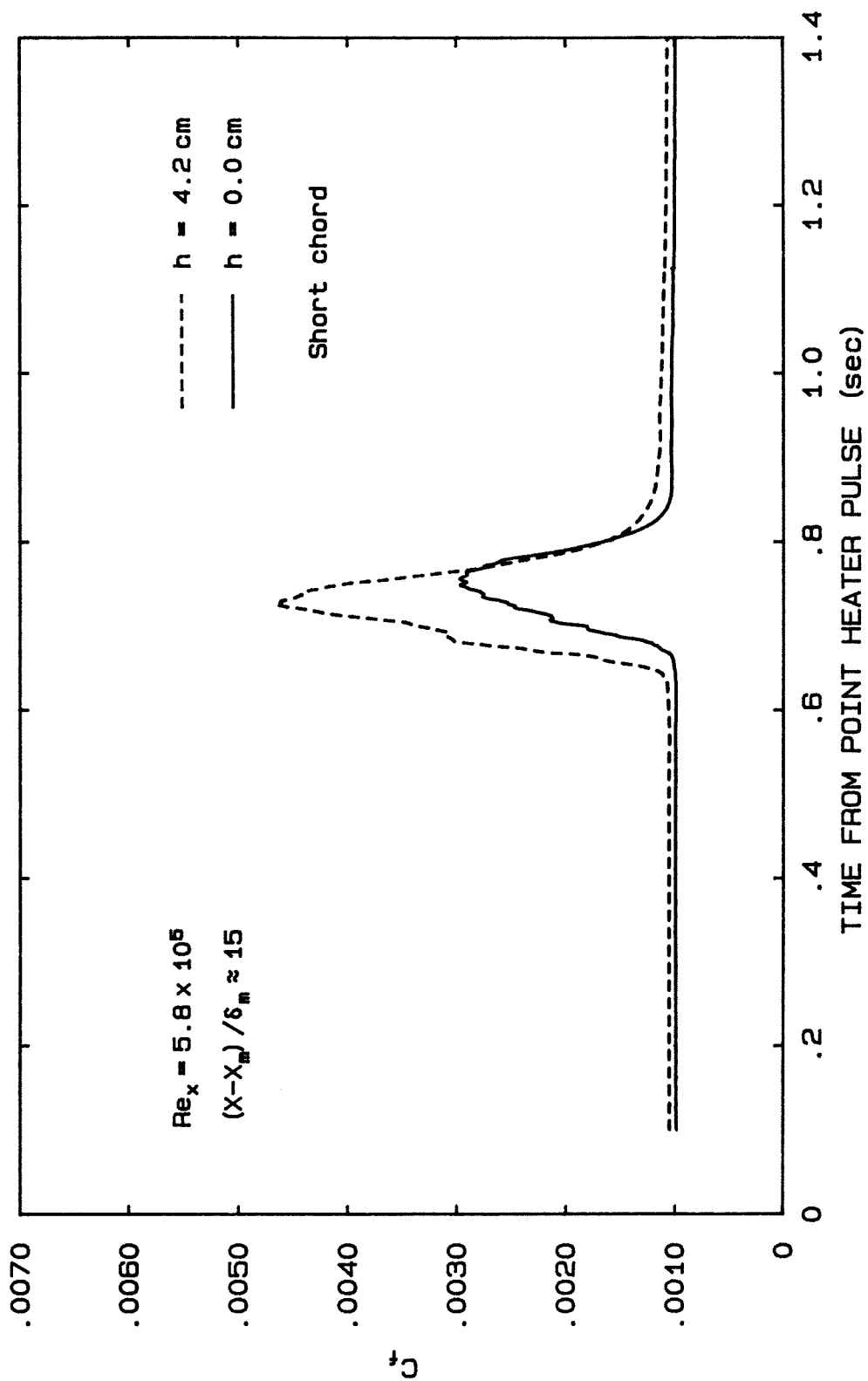


Figure 5.5 Turbulent spot wall-shear behavior at its spanwise extremity.  
Short-chord, vertical-fin device. z/b = 0.9

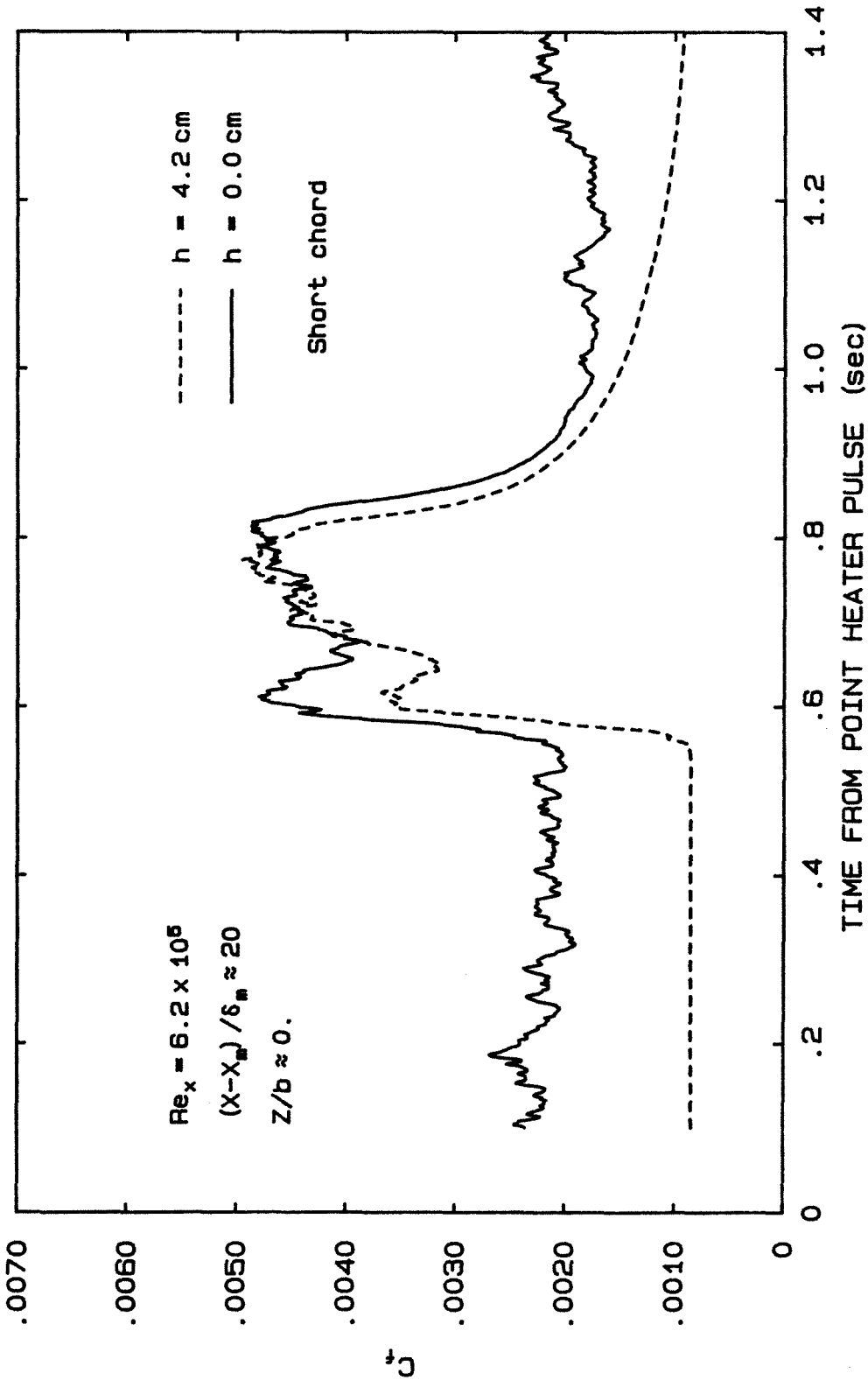
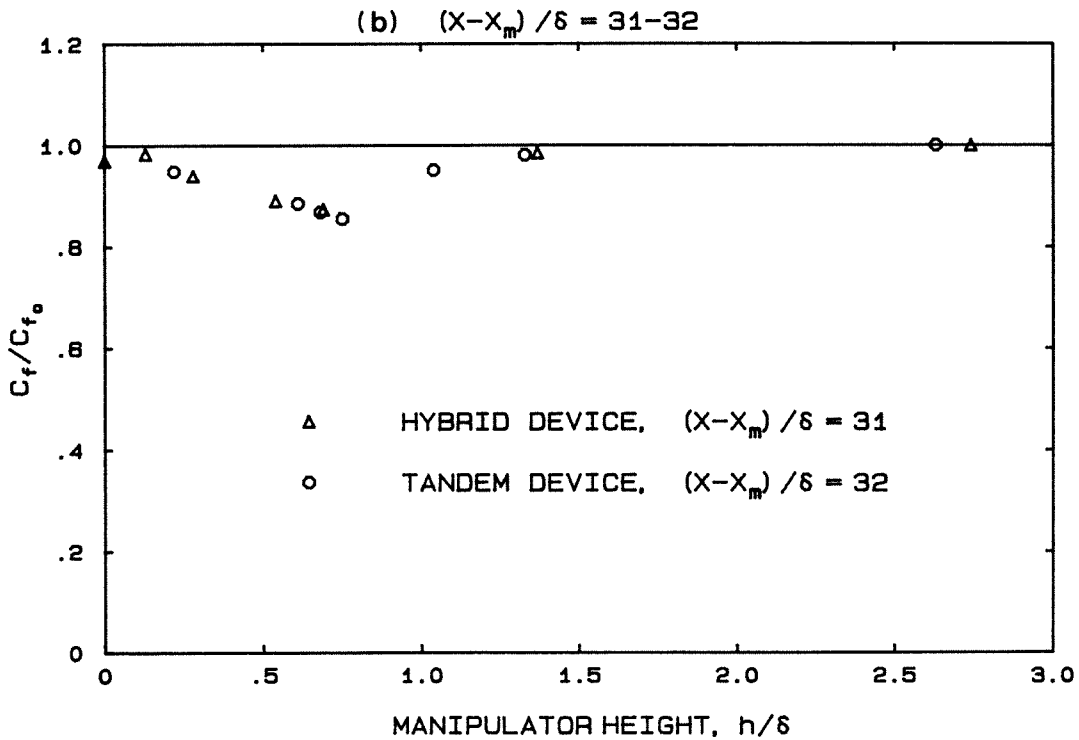
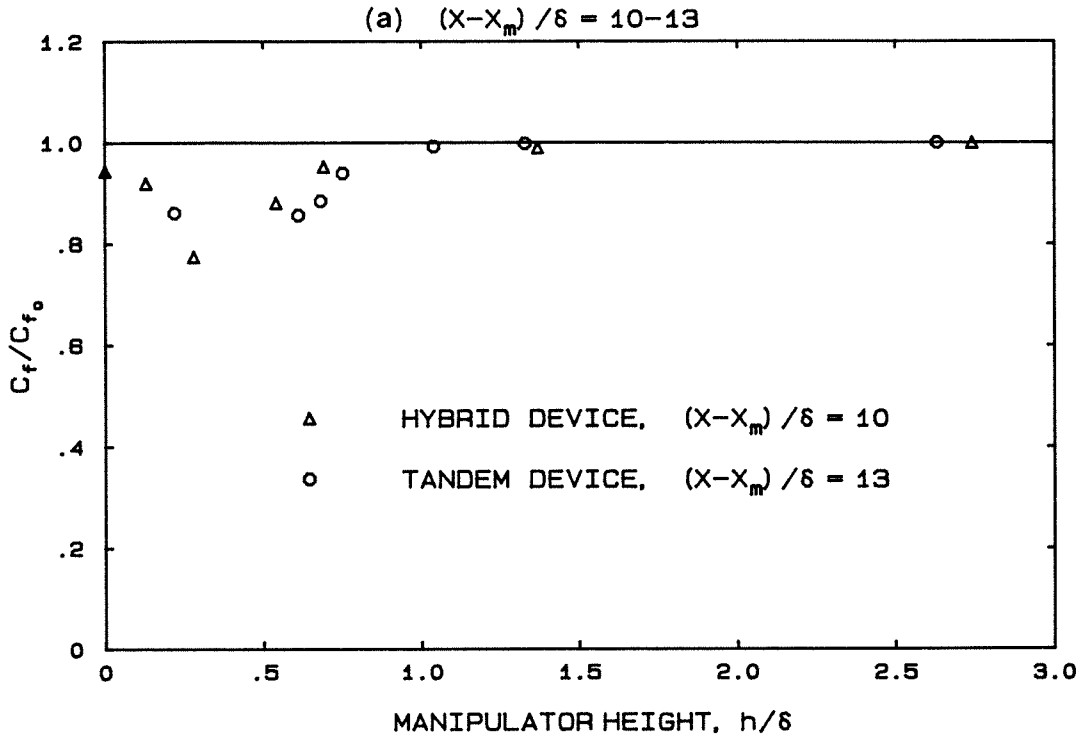
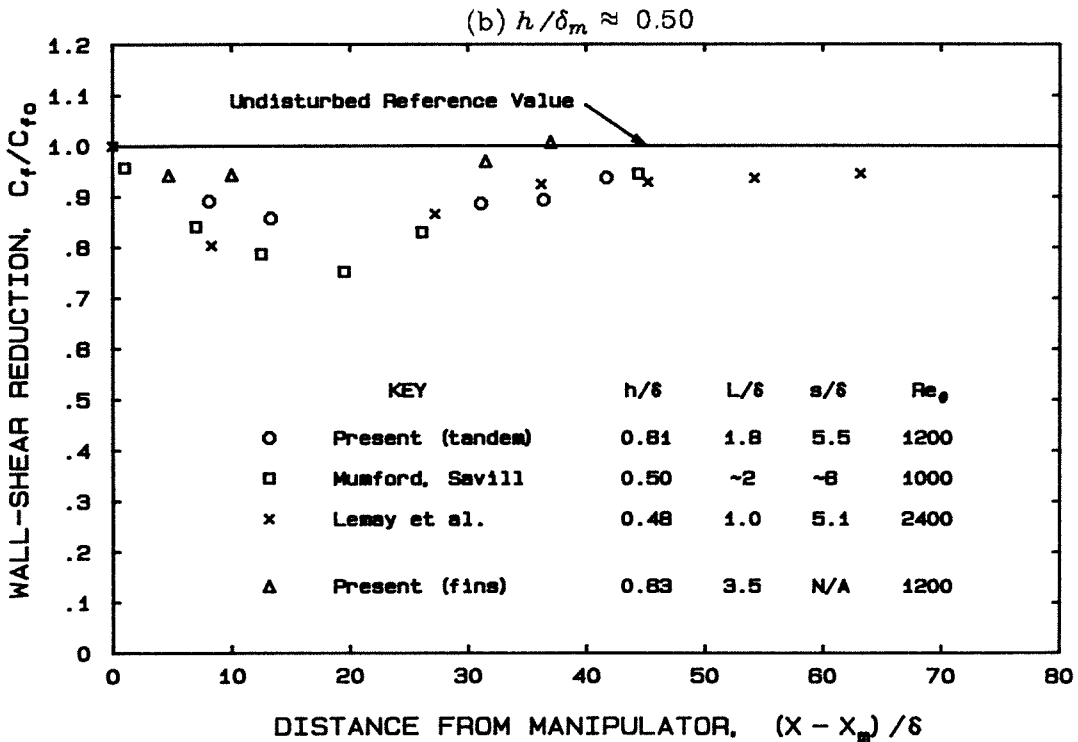
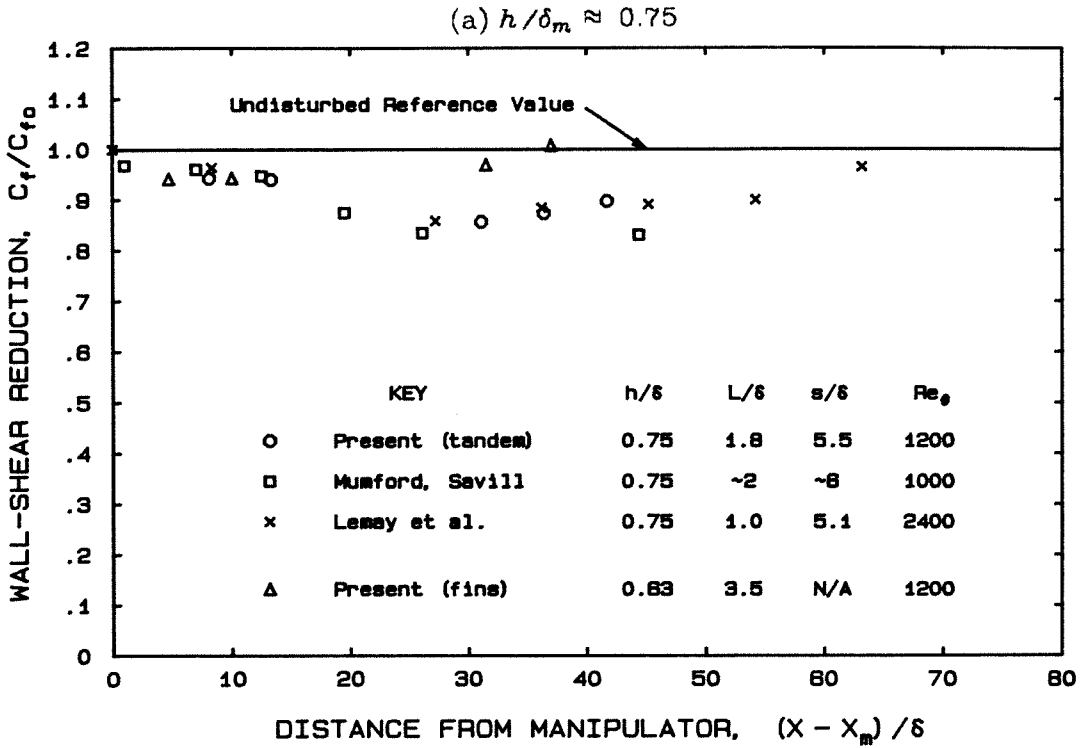


Figure 5.6 Effect of manipulator wake on ambient flow *directly* downstream of a fin



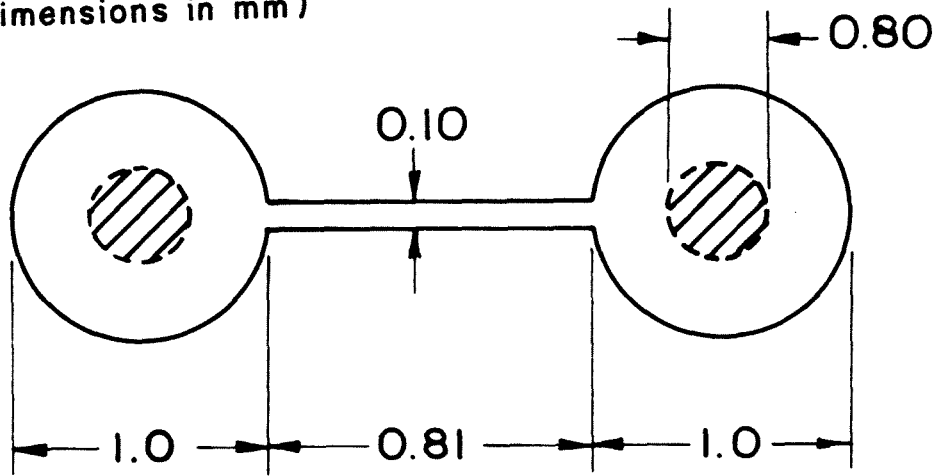


**Figure 5.7** Comparison between hybrid and tandem manipulators in a turbulent boundary layer. Variation of wall-shear reduction with height of manipulator.  
(a)  $(x-x_m)/\delta_m = 10-13$ , (b)  $(x-x_m)/\delta_m = 31-32$

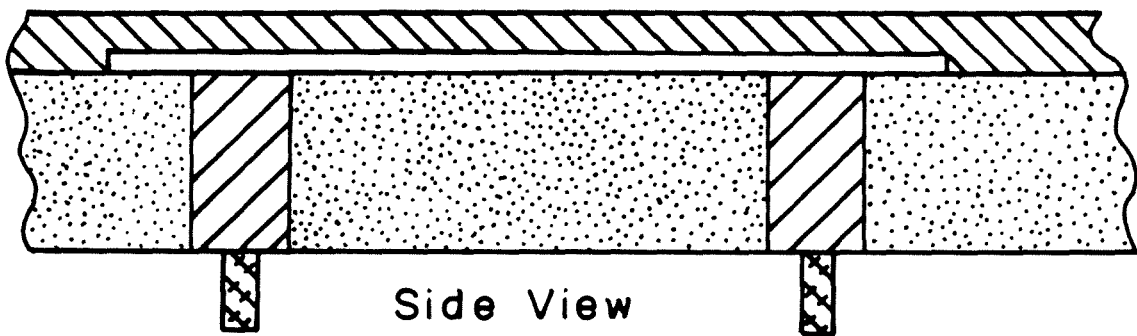


**Figure 5.8** Comparison between vertical-fin manipulator and tandem device in a turbulent boundary layer. Distribution of wall-shear downstream of devices. (a)  $h/\delta_m \approx 0.75$ , (b)  $h/\delta_m \approx 0.50$ . The data for the vertical-fin device are the same in both plots.

(dimensions in mm)



Top View



Side View






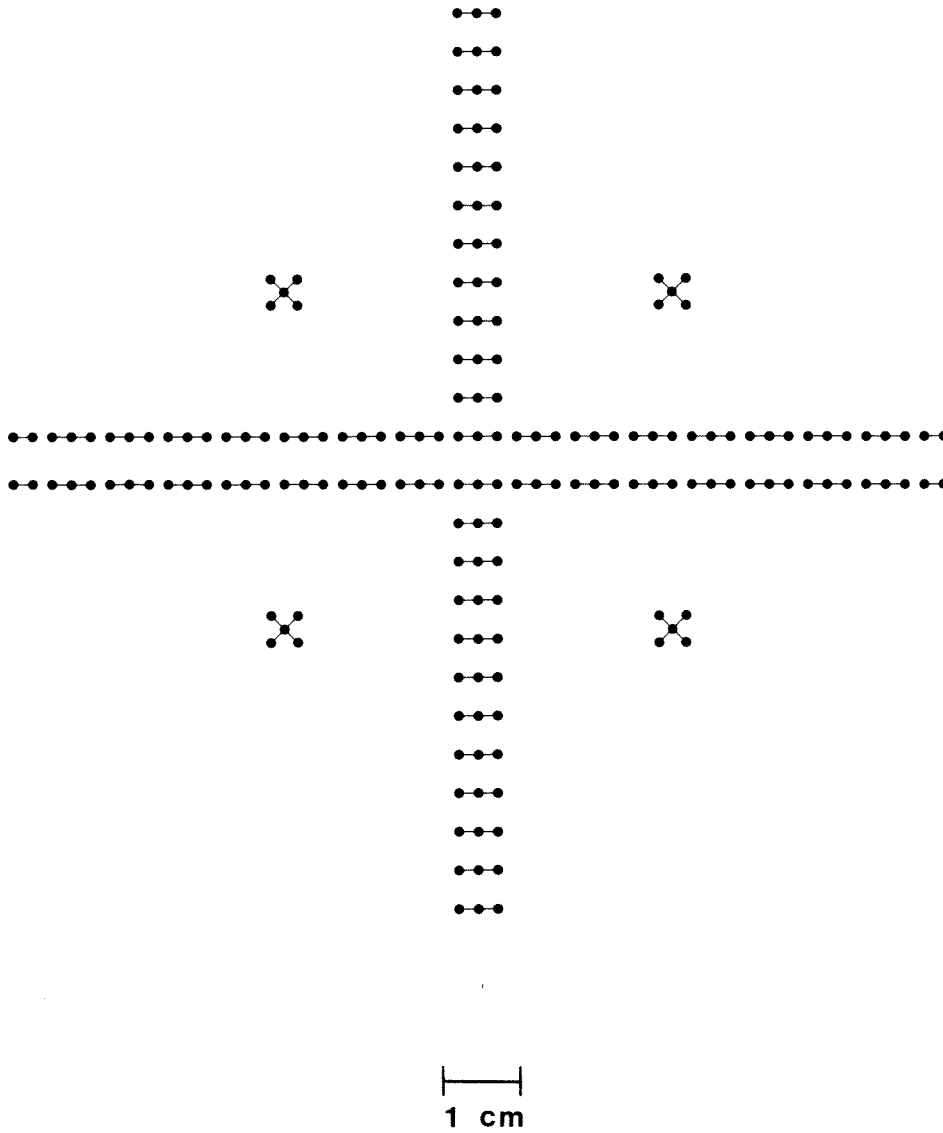
-  solid copper pins, 22 AWG
-  tin, vacuum deposited, 1000 Å thickness
-  silver-filled conductive epoxy
-  Parylene C coating, 2 μm thickness
-  glass-reinforced resin

Figure A.1 Design of thin-film wall-shear sensors



**Figure A.2** Typical pattern of wall-shear sensors  
(Pattern used for sensor array in Figure 2.4)

## 1. References

- ANDERS, J.B., HEFNER, J.N. and BUSHNELL, D.M. 1984 Performance of large-eddy breakup devices at post-transitional Reynolds numbers. *AIAA Paper* 84-0345.
- ANDERS, J.B. and WATSON, R.D. 1985 Airfoil large-eddy breakup devices for turbulent drag reduction. *AIAA Paper* 85-0520.
- BERTELUD, A., TRUONG, T.V. and AVELLAN, F. 1982 Drag reduction in turbulent boundary layers using ribbons. *AIAA Paper* 82-1370.
- BROWN, G.L. 1967 Theory and application of heated films for skin friction measurement. *Proc. 1967 Heat Transfer and Fluid Mech. Inst.*, 361-381.
- BROWN, G.L. and ROSHKO, A. 1971 The effect of density difference on the turbulent mixing layer. In: *Turbulent Shear Flows*, (AGARD CP 93), Paper 23.
- CANTWELL, B., COLES, D. and DIMOTAKIS, P. 1978 Structure and entrainment in the plane of symmetry of a turbulent spot. *J. Fluid Mech.* **87**, 641-672.
- CLAUSER, F.H. 1954 Turbulent boundary layers in adverse pressure gradients. *J. Aeronaut. Sci.* **21**, 91-180.
- CLAUSER, F.H. 1956 The turbulent boundary layer. *Adv. Appl. Mech.* **4**, 1-51.
- COLES, D. and BARKER, S. 1975 Some remarks on a synthetic turbulent boundary layer. In: *Turbulent Mixing in Nonreactive and Reactive Flows*, Plenum, 285-292.
- COLES, D. and HIRST, E.A. 1968 *Proc. of the Computation of Turbul. Boundary Layers -- 1968 AFOSR-IFP-Stanford Conf.*, II, Stanford Univ.
- CORKE, T.C. 1981 A new view on origin, role and manipulation of large scales in turbulent boundary layers. Ph.D. Thesis, Illinois Institute of Technology.
- CORKE, T.C., GUEZENNEC, Y.G. and NAGIB, H.M. 1980 Modification in drag of turbulent boundary layers resulting from manipulation of large-scale structures. *Progr. in Astronaut. and Aeronaut.* **72**, 128-143.
- CORKE, T.C., NAGIB, H.M. and GUEZENNEC, Y.G. 1982 A new view on origin, role, and manipulation of large scales in turbulent boundary layers. *NASA-CR-165861*.
- DOWLING, A.P. 1985 The effect of large-eddy breakup devices on oncoming vorticity. *J. Fluid Mech.* **160**, 447-463.
- GAD-EL-HAK, M., BLACKWELDER, R.F. and RILEY, J.J. 1981 On the growth of turbulent regions in laminar boundary layers. *J. Fluid Mech.* **110**, 73-95.
- GUEZENNEC, Y.G. and NAGIB, H.M. 1985 Documentation of mechanisms leading to net drag reduction in manipulated turbulent boundary layers. *AIAA Paper* 85-0519.

- HARITONIDIS, J.H., KAPLAN, R.E. and WYGNANSKI, I. 1977 Interaction of a turbulent spot with a turbulent boundary layer. *Lecture Notes in Physics* **75**, 234-247.
- HEFNER, J.N., ANDERS, J.B. and BUSHNELL, D.M. 1983 Alteration of outer flow structures for turbulent drag reduction. *AIAA Paper* 83-0293.
- HEFNER, J.N., WEINSTEIN, L.M. and BUSHNELL, D.M. 1980 Large-eddy breakup scheme for turbulent viscous drag reduction. *Progr. in Astronaut. and Aeronaut.* **72**, 110-127.
- HESS, J.L. and SMITH, A.M.O. 1966 Calculation of potential flow about arbitrary bodies. *Progr. Aeronaut. Sci.* **8**, Pergamon Press, 1-138.
- ITSWEIRE, E.C. and VAN ATTA, C.W. 1984 An experimental investigation of coherent substructures associated with turbulent spots in a laminar boundary layer. *J. Fluid Mech.* **148**, 319-348.
- KINNEY, R.B. 1985 Numerical study of large-eddy breakup and its effect on the drag characteristics of boundary layers. *NASA CR-3884*.
- KLINE, S.J., REYNOLDS, W.C. SCHRAUB, F.A., and RUNSTADLER, P.W. 1967 The structure of turbulent boundary layers. *J. Fluid Mech.* **30**, 741-773.
- LAGUNA, G.A. 1975 Second sound attenuation in a liquid helium counterflow jet. Ph.D. Thesis, California Institute of Technology.
- LEMAY, J., PROVENCAL, D., GOURDEAU, R., NGUYEN, V.D. and DICKINSON, J. 1985 More detailed measurements behind turbulence manipulators including tandem devices using servo-controlled balances. *AIAA Paper* 85-0521.
- LIEPMANN, H.W. 1958 A simple derivation of Lighthill's heat transfer formula. *J. Fluid Mech.* **3**, 357-360.
- LIEPMANN, H.W., BROWN, G.L. and NOSENCHUCK, D.M. 1982 Control of laminar-instability waves using a new technique. *J. Fluid Mech.* **118**, 187-200.
- LIGHTHILL, M.J. 1950 Contributions to the theory of heat transfer through a laminar boundary layer. *Proc. Roy. Soc. London*, **A202**, 359-377.
- MUMFORD, J.C. and SAVILL, A.M. 1984 Parametric studies of flat plate, turbulence manipulators including direct drag results and laser flow visualisation. Presented at *ASME Symposium*, Feb. 11-17, New Orleans.
- NOSENCHUCK, D.M. 1982 Passive and active control of boundary layer transition. Ph.D. Thesis, California Institute of Technology.
- PERRY, A.E., LIM, T.T. and TEH, E.W. 1981 A visual study of turbulent spots. *J. Fluid Mech.* **104**, 387-405.
- PLESNIAK, M.W. and NAGIB, H.M. 1985 Net drag reduction in turbulent boundary layers resulting from optimized manipulation. *AIAA Paper* 85-0518.
- ROBEY, H.F. 1986 The nature of three-dimensional instability waves in boundary layer transition. Ph.D. Thesis, California Institute of Technology.
- SCHUBAUER, G.B. and KLEBANOFF, P.S. 1955 Contributions on the mechanics of boundary layer transition. *NACA Rep.* 1289.

- TAKAGI, S. 1983 The structure of turbulent boundary layer controlled by the plates. *Proc. of the 15th Turbulence Symp.*, Tokyo, Japan.
- TANI, I. 1968 Review of some experimental results on the response of a turbulent boundary layer to sudden perturbations. *Proc. of the Computation of Turbul. Boundary Layers -- 1968 AFOSR-IFP-Stanford Conf.*, I, Stanford Univ., 483-494.
- WARD, T.M. 1976 The Hydrodynamics Laboratory at the California Institute of Technology. *Trans. ASME*, Dec., 740-748.
- WYGNANSKI, I. 1980 The effects of Reynolds number and pressure gradient on the transitional spot in a laminar boundary layer. *Lecture Notes in Physics* **136**, 304-332.
- WYGNANSKI, I. 1981 On turbulent spots. In: *Symposium on Turbulence*, Univ. of Missouri-Rolla, eds. G.K. Patterson & J.L. Yakin.
- WYGNANSKI, I., SOKOLOV, M. and FRIEDMAN, D. 1976 On a turbulent spot in a laminar boundary layer. *J. Fluid Mech.* **78**, 785-819.
- WYGNANSKI, I., ZILBERMAN, M. and HARITONIDIS, J.H. 1982 On the spreading of a turbulent spot in the absence of a pressure gradient. *J. Fluid Mech.* **123**, 69-90.
- YAJNIK, K.S. and ACHARYA, M. 1977 Non-equilibrium effects in a turbulent boundary layer due to the destruction of large eddies. *Lecture Notes in Physics* **75**, 249-260.
- YAJNIK, K.S., ACHARYA, M. AND SUNDARAM, S. 1980 Non-equilibrium effects in a turbulent boundary layer. *Proc. of the First Asian Congress of Fluid Mechanics*, Bangalore, India. Paper A19.